Assessment of composite fuselage crashworthiness: A virtual testing methodology

Mário Rui Dias Miranda

Dissertation developed in the framework of a research stay at the Aeronautical and Structural Design Lab (ASD Lab) of the UC3M aerospace engineering department

and submitted to Universidade do Porto – Faculdade de Engenharia in partial fulfillment of the requirements for the degree of Master in Mechanical Engineering

Supervisors:

Prof. Andrea Cini, UC3M

Prof. Antonio Raimondo, UC3M

Prof. Volnei Tita, FEUP

June, 2023

"Aqui...onde a terra se acaba e o mar começa."
- Luís de Camões

Acknowledgments

Firstly, I want to express my deep gratitude to Professor Andrea Cini for giving me the opportunity to develop this thesis in his research group, the Aeroelastic and Structural Design (ASD) Lab. His guidance, expertise, and mentorship have played a vital role in my growth and independence throughout this research endeavor.

I would also like to extend my thanks to Professor Antonio Raimondo for the continuous support, availability, and patience. He has been a constant source of guidance, encouraging me to delve deeper into my work and fostering a sense of self-critique.

I am grateful to Professor Volnei Tita for his insights into the world of aeronautics, support and for the interest shown on my work during all my master's degree.

I want to thank all of the ASD Lab members, with whom I shared my daily struggles, progress, and discussed different areas of research, for their companionship. From day one, they made sure I felt welcomed and part of the group.

I am deeply thankful to my friends and family for their love and support during this process.

To all the people that I crossed paths with at the UC3M Aerospace Engineering department, who have also made me feel at home, thank you.

A special thank to my parents, who supported me in the most difficult times, which without their encouragement and wise advice, I would not have been able to complete this journey.

Abstract

This thesis focuses on simulating the crashworthiness of composite fuselage components in civil transportation aircraft. Despite the rise in air transportation over the last few decades, fatal accident rates have decreased due to strict airworthiness regulations and safety requirements, which the industry has gained confidence in complying with metallic designs. However, with the increasing use of lightweight materials such as polymer matrix composites, with different material properties and energy absorption mechanisms, it is crucial to guarantee safety is not compromised in case of emergency landings. Special Conditions have been created to ensure no significant difference in survivability between similar-sized aircraft made with composite or metal airframes. Compliance to these conditions can be demonstrated through direct testing or numerical tools such as finite element analysis. However, despite the latter presenting a wide range of advantages, simplified models have been used in the past to keep computational costs low, sometimes leading to differences between simulations and experimental results. This work aims at implementing improved numerical inter and intra-laminar damage evolution models, to improve the damage prediction accuracy of simulations to possibly enable the development of novel virtual testing methodologies for composite structures crashworthiness assessment. To this end, three different damage models, with different failure criteria, were created and used in conjunction with ABAQUS software via user defined materials (VUMAT), which were successfully numerically verified. Then, to validate the developed routines, two benchmark composite damage problems, an Open Hole Tensile (OHT) test and a low velocity impact were simulated and the results compared to previous literature. The developed subroutines resulted in a experimental test correlation improvement compared to the original literature models. Finally, a virtual certification dynamic test of composite fuselage component is carried on for all the different failure criteria and a comparison against the experimental results, available in literature is performed. It was concluded that the suggested methodology provided higher fidelity results regarding the crash behaviour of the composite part.

Resumo

Esta tese foca-se na simulação da resistência ao impacto de componentes de fuselagens em materiais compósitos de aeronaves de transporte civil. Apesar do aumento do tráfego aéreo nas últimas décadas, as taxas de acidentes fatais têm vindo a diminuir devido a regulamentações rigorosas de aeronavegabilidade e requisitos de segurança nos quais a indústria ganhou experiência e confiança em cumprir com designs metálicos. No entanto, com o aumento do uso de materiais leves, como os materiais compósitos de matriz polimérica, e com as suas diferentes propriedades e mecanismos de absorção de energia, é crucial estabelecer métodos para garantir que a segurança não seja comprometida em caso de aterragens de emergência. Foram criadas 'Special Conditions' para garantir que não haja diferença significativa na sobrevivência entre aeronaves de dimensões semelhantes feitas de metal ou compósito. O cumprimento dessas condições pode ser demonstrado por meio de testes diretos ou ferramentas numéricas, como a análise por elementos finitos. No entanto, apesar de esta última apresentar uma ampla gama de vantagens, modelos simplificados têm sido utilizados no passado para manter baixos os custos computacionais, o que às vezes resulta em diferenças entre as simulações e os resultados experimentais. Este trabalho tem como objetivo implementar modelos numéricos aprimorados de evolução de danos inter e intra-laminares para melhorar a precisão na previsão de danos nas simulações e, possivelmente permitir o desenvolvimento de novas metodologias de teste virtual para a avaliação da resistência a impactos de estruturas em material compósito. Para este efeito, três modelos de dano diferentes, com critérios de falha diferentes foram usados em conjunto com o software ABAQUS através de 'user defined materials' (VUMAT), que, foram numericamente verificados com sucesso. Depois, de forma a validar os modelos desenvolvidos, foram simulados e comparados com a literatura anterior dois problemas de dano em materiais compósitos de referência: um 'Open Hole Tensile (OHT) Test' e um teste de impacto de baixa velocidade. Os modelos desenvolvidos resultaram numa melhoria da correlação com os resultados experimentais em relação aos modelos da literatura. Por fim, um teste dinâmico virtual de certificação de um componente de fuselagem em material compósito foi realizado para todos os diferentes critérios de falha, e foi realizada uma comparação com os resultados experimentais disponíveis na literatura. Concluiu-se que a metodologia sugerida proporcionou resultados de maior fidelidade em relação à resposta ao impacto de uma coluna em material compósito.

Contents

1 Introduction **1**
- 1.1 Goals and methodology . . . 2
- 1.2 Thesis outline . . . 3

2 Literature review **5**
- 2.1 Crashworthiness . . . 5
  - 2.1.1 Definition . . . 5
  - 2.1.2 Regulations . . . 5
  - 2.1.3 Composite Regulations . . . 5
- 2.2 Drop Tests . . . 8
  - 2.2.1 Testing requirements . . . 8
  - 2.2.2 Conducted tests . . . 9
    - 2.2.2.1 Composite fuselage drop tests . . . 12
- 2.3 Fuselage Energy Absorption Structures . . . 14
  - 2.3.1 Fuselage . . . 14
  - 2.3.2 Sub-cargo area . . . 15
  - 2.3.3 Stanchions . . . 15
- 2.4 Building Block Approach . . . 17
    - 2.4.0.1 Coupons . . . 18
    - 2.4.0.2 Structural Elements . . . 19
    - 2.4.0.3 Details . . . 20
    - 2.4.0.4 Sub-Components . . . 20
    - 2.4.0.5 Components . . . 21

3 Theoretical Background and Numerical Implementation **23**
- 3.1 Intra-Laminar damage . . . 23
  - 3.1.1 Damage onset . . . 24
  - 3.1.2 Damage evolution . . . 31
  - 3.1.3 Damage model . . . 34
- 3.2 Inter-Laminar damage . . . 35
- 3.3 Numerical Implementation . . . 37
  - 3.3.1 Explicit and Implicit Schemes . . . 37
  - 3.3.2 Element Formulation . . . 38
  - 3.3.3 VUMAT development . . . 39

4 Composite Failure Model Numerical Development and Validation **43**
- 4.1 One element test . . . 43
  - 4.1.1 Hashin Failure Criterion . . . 45
  - 4.1.2 Puck Failure Criterion . . . 46
  - 4.1.3 Strain Rate Dependent Failure Criterion . . . 47

5 Model Development and Validation **51**
- 5.1 Open Hole Tensile Test . . . 51
  - 5.1.1 Model description . . . 51
  - 5.1.2 Results . . . 53
- 5.2 Low Velocity Impact . . . 60

5.2.1 Model description 60
5.2.2 Preliminary results 64
5.2.3 Sensitivity analysis 68
5.2.4 Results 73

6 Sub-Cargo Element **79**
6.1 Test specimen and model description 79
6.2 Quasi-static test 83
6.3 Impact tests 85
6.3.1 Low Energy Impact 85
6.3.2 High Energy Impact 88
6.3.2.1 Acceleration an Energy absorption 97
6.3.2.2 Comparison with experimental results 102

7 Conclusions & Future Work **107**
7.1 Conclusions 107
7.2 Future Work 108

List of Figures

2.1 Evolution of composite composition from 1970 to 2020 [14]. 6
2.2 CID full-scale crash test of a B720 [32]. 9
2.3 Vertical drop tests of two B737 fuselage sections (a) with conformable auxiliary fuel tank (b) with overhead bins and luggage [35]. 10
2.4 Fokker F28 impact test conducted at NASA Langley Research Center (LaRC) Impact Dynamics Research Facility. (a) undeformed and (b) deformed fuselage section [37]. 11
2.5 Aftermath of the ATR 42-300 drop test with visible extensive damage [38]. . . . 11
2.6 Fuselage section with internal facilities drop test. (a) undeformed and (b) deformed fuselage section [39]. 12
2.7 Full-scale crash test of a F28 [41]. 12
2.8 Deformed composite fuselage section of a regional aircraft [44]. 13
2.9 Drop tests through the years differentiating composite fuselage sections (square). Adapted from [11]. 13
2.10 Semi-monocoque configuration [46]. 14
2.11 Fuselage sections and respective load path in case of impact [47]. 14
2.12 Sub-cargo structure [49]. 15
2.13 C section stanchions [11]. 15
2.14 Relation between energy absorption and failure mechanisms [56]. 16
2.15 Typical load-displacement curve [57]. 16
2.16 Schematic of building block approach for a fixed wing component [6]. 17
2.17 Typical building block program flow [60]. 18
2.18 Examples of standards for composite coupon testing [65]. 19
2.19 Examples of single lap shear tests [68]. 19
2.20 Crashworthiness tests of (a) frames and (b) stanchions [11, 69]. 20
2.21 Inverted impact test of an A350 sub-cargo structure [70]. 21
2.22 Crashworthiness building block approach of an A350 fuselage [70]. 21
3.1 Inter, intra and translaminar failure modes [73]. 23
3.2 Composite failure modes [74]. 24
3.3 Linear an quadratic approximations of the failure surfaces [85]. 25
3.4 Potential fracture plane, respective orientation, θ, and stress components [87]. 27
3.5 SPIS method for a specific 3D load case with two local maxima [89]. 28
3.6 Ply material orientation [95]. 30
3.7 Linear and exponential degradation models [97]. 31
3.8 Fracture energy represented by the enclosed area [99]. 33
3.9 Influence of the characteristic length l_c on the constitutive model. Adapted from [98]. 33
3.10 Mixed-mode behaviour of a cohesive element [105]. 37
3.11 Example of a 3D element (C3D8, 8-node linear brick) [107]. 39
3.12 Flowchart of 3D Hashin VUMAT [84]. 39
4.1 One millimeter side cubic element loaded in the longitudinal direction. 43
4.2 Longitudinal Tension VUMAT verification. 45
4.3 Tension and Compression bi-linear curves for (a) longitudinal and (b) transverse directions. 45
4.4 Compression bi-linear curves for the tranverse direction using Puck criterion. . 47

4.5 Strain rate dependent stress-strain curves for (a) longitudinal tension, (b) longitudinal compression, (c) transverse tension and (d) transverse compression. . 48
5.1 Geometric details and boundary conditions of the problem [27]. 51
5.2 Meshed OHT part: (a) top view and (b) partial lateral view. 52
5.3 Boundary conditions and highlighted displacement track node (top right). . . . 53
5.4 Load-displacement curve using Hashin failure criterion. 53
5.5 Load-displacement curve using Hashin failure criterion with instantaneous and gradual degradation. 54
5.6 Selected path for the assessment of damage through the thickness. 54
5.7 Distribution of the non-zero damage variables employing Hashin criterion. . . . 55
5.8 Load-displacement curve using Puck failure criterion. 55
5.9 Distribution of the non-zero damage variables employing Puck criterion. 56
5.10 Damage distribution comparison for each ply orientation following Hashin criterion. Adapted from [27]. 57
5.11 Damage distribution comparison for each ply orientation following Puck criterion. Adapted from [27]. 58
5.12 Damage distribution comparison with [111], for matrix damage following Puck criterion. Adapted from [27]. 58
5.13 Fibre tensile damage on 0° ply immediately before total failure (Hashin criterion). 59
5.14 Plate, impactor and respective boundary conditions. 60
5.15 Meshed plate. 61
5.16 Bending behaviour of a linear reduced integration element [118]. 63
5.17 Numerical and previously existing literature energy-time curves. 65
5.18 Numerical and previously existing literature force-time curves. 66
5.19 Matrix tensile damage on each composite layer: (a) Shao et al. (b) Numerical. Adapted from [115]. 66
5.20 Inter-laminar damage on each interface: a) Shao et al. b) Numerical. Adapted from [115]. 67
5.21 Overall delamination: a) X-ray radiograph b) Numerical. Adapted from [115]. . 67
5.22 Energy-time curves of case (a) one and (b) three. 71
5.23 Case 13 (relax stiffness with $s = 1.5$) energy-time curve. 72
5.24 Case 13 force-time curve. 74
5.25 Case 13 matrix tensile damage on each composite layer: a) Shao et al. b) Numerical. Adapted from [115]. 74
5.26 Inter-laminar damage on each interface: a) Shao et al. b) Case 13. Adapted from [115]. 75
5.27 Overall delamination: a) X-ray radiograph b) Case 13. Adapted from [115]. . . 75
5.28 Energy-time curves employing (a) Puck and (b) Strain Rate Dependent criteria. 76
6.1 Geometric details of the stanchion. Adapted from [124]. 79
6.2 Stacking sequence of the stanchion [123]. 79
6.3 Meshed stanchion. 81
6.4 Number of elements through the thickness. (a) one element per 3 plies [123] and (b) one element per ply. Adapted from [123] 82
6.5 Experimental setup [123]. 82
6.6 Boundary conditions of the model. 83
6.7 Experimental and numerical quasi static load-displacement curves. 84
6.8 Deformed shape after the quasi-static compression. 84

6.9 Analytical and numerical displacement-time curves. 86
6.10 Analytical, numerical and filtered numerical force-time curves. 87
6.11 Analytical and numerically obtained kinetic and internal curves. 88
6.12 Evolution of the deformed shape, using Hashin failure criterion. 89
6.13 Detail of the deformed shape 15 ms after impact, using Hashin failure criterion. 90
6.14 First non-zero SDEG value registered at the interface between the stanchion and the potting (0.3 ms after impact). 90
6.15 Fibre compression failure distribution at the first registered total failure (0.6 ms after impact). 91
6.16 Damage variables through the thickness of a 12 mm above potting flange element (0.75 ms after impact). 91
6.17 Local buckling (a) lateral displacement and (b) matrix tensile damage due to bending stress (0.85 ms after impact). 92
6.18 Shape and inter-laminar damage evolution (1.05 ms to 1.275 ms after impact). 92
6.19 Evolution of the deformed shape, using Puck failure criterion. 93
6.20 Detail of the deformed shape 15 ms after impact, using Puck failure criterion. . 93
6.21 Matrix compressive damage near or inside the potting zone, where the dot represents the surface of the potting (0.525 ms after impact). 94
6.22 (a) Band of matrix compressive damage and (b) buckling of the structure (0.6 ms after impact). 94
6.23 Buckling of the delaminated plies employing Puck failure criterion (1.425 ms after impact). 95
6.24 Evolution of the deformed shape, using SRD failure criterion. 95
6.25 Detail of the deformed shape 15 ms after impact, using SRD failure criterion. . 96
6.26 Fibre compression failure, at the same simulation time, in the intermediate zone of the laminate employing (a) Hashin and (b) SRD failure criterion (0.6 ms after impact). 96
6.27 Energy-Time curves of the stanchion employing Hashin criterion. 97
6.28 Acceleration-Time curves of the stanchion employing Hashin criterion. 98
6.29 Force-Displacement curve of the stanchion employing Hashin criterion. 99
6.30 Kinetic energy of the impactor for the three different models 100
6.31 Local buckling zones and shapes employing (a) Hashin and (b) Puck criterion (1.95 ms after impact). 100
6.32 Acceleration-time curves of the three different models. 101
6.33 Force-displacement curves of the three different models. 101
6.34 Experimental damage after 585 J impact. (a) Damaged region near potting and (b) respective amplification [123, 124]. 102
6.35 Superimposition with the experimental results of the lateral displacement of the SRD model and damage through the thickness near critical zone (7.5 ms after impact). 103
6.36 Vertical displacement at maximum compression (a) and fibre compressive damage state (b) previously obtained in [123] and vertical displacement at maximum compression (c) and undeformed fibre compressive damage state with transparency (d) obtained with SRD failure criterion. 104

List of Tables

3.1 Phenomenological and non-phenomenological failure criteria. 25
3.2 Scaling factors. 30
3.3 Equivalent displacement and stress for each failure mode. 32
3.4 VUMAT required material constants. 41
3.5 State variables. 42
4.1 Material properties for numerical verification [98]. 44
4.2 Intra-laminar volumetric fracture energy for numerical verification [98]. 44
4.3 Expected and obtained values of relevant properties for the 3D Hashin element verification. 46
4.4 Expected and obtained values of relevant properties for the Puck element verification. 47
4.5 Longitudinal tension properties. 49
4.6 Longitudinal compression properties. 49
4.7 Transverse tension properties. 49
4.8 Transverse compression properties. 49
5.1 Obtained maximum loads. 56
5.2 Material properties for impact numerical verification [114]. 62
5.3 Intra-laminar volumetric fracture energies for impact numerical verification [114]. 62
5.4 Material properties of the cohesive interface for impact numerical verification [114]. 63
5.5 Sensitivity analysis on hourglass control and and step viscosity. 70
5.6 Energy summary and computational time for cases 1, 3 and 13. 72
5.7 Mean square error relatively to the experimental curve of the best results. . . . 73
5.8 Mean square error relatively to the experimental curve of both Puck and Strain Rate Dependent (SRD) failure criteria. 77
6.1 Material properties of the stanchion laminae [123]. 80
6.2 Intra-laminar volumetric fracture energies of the stanchion laminae [123]. . . . 80
6.3 Material properties of the cohesive interfaces of the stanchion [123]. 81
6.4 Experimental and numerical stiffness values. 85
6.5 Impact tests. 85
6.6 Computational times of the three different models. 97
6.7 Summary of registered reaction forces and specific energy absorption. 102

1 Introduction

Worldwide air transportation has been on the rise over the last couple of decades, until 2020, when the COVID-19 pandemic significantly reduced the number of flights. Nonetheless, there has been a substantial recovery since travel restrictions were alleviated and the same number of travels of 2019 is expected to be reached by 2024 and to continuously grow in the next few decades [1, 2].

Fortunately, the number of fatal accident rates (per million departures) has followed an inverse trend [1], owing to the strict regulations and requirements that need to be fulfilled and are regularly updated based on the experience and observation of field data. However, there are still some issues that need to be addressed to reduce even further the casualty rates.

In fact, the majority of fatal accidents that occurred in the last few years have been related to either the initial and final stages of the flight, being the latter (final approach and landing) responsible for practically half of the fatal accidents and nearly a third of onboard fatalities [1, 3].

In order to reduce these numbers to the minimum, crasworthiness regulations have been created and updated ensuring that the survivability of the occupants in case of an accident increases.

Current regulations for civil transportation aircraft such as sections 25.561 and 25.562 given in CS 25/FAR 25 [4, 5] establish the minimum requirements related to "Emergency Landing Conditions", which, the aeronautical industry has developed confidence and expertise in complying, particularly in adhering to conventional metallic design solutions [6].

However, as the aeronautical industry strives for a more sustainable stance and to lower operational and maintenance costs, lightweight materials such as polymer matrix composites have been replacing metals on principal structural elements such as circumferential frames and fuselage skin, owing to their high corrosion and fatigue resistance coupled with a higher manufacturing flexibility.

Taking into account the differences between these materials (eg.,stiffness, ductility, failure modes), it is of paramount importance to ensure that safety is not compromised by this change.

To address this issue, Special Conditions [7] with a specific set of criteria, were created by the regulatory bodies to ensure that no significant difference in survivability is expected between similar-sized aircraft made of these two material types.

Following these rules, compliance can be demonstrated either through direct testing such as drop tests or by numerical tools such as finite element analysis (FEA), given that they are validated through building block approach and correlation tests. Despite

both approaches requiring experimental testing, the latter takes the edge since once validated, different configurations may be virtually tested, reducing time and financial costs.

However, despite the fact that numerical simulations present a whole plethora of advantages, there are some limitations that may limit their full potential such as computational and model development times. In fact, to overcome these issues, less complex models such as the use of two dimensional elements and failure theories have been implemented, which, sometimes, are not able to accurately predict the impact behaviour of composite structures.

1.1 Goals and methodology

The objective of this work is to develop and implement enhanced numerical models, at the mesoscale level, to improve the damage prediction accuracy of composite material simulations, and to possibly pave the way for novel virtual testing methodologies for the assessment of the crashworthiness of composite fuselage components, decreasing the required times and/or experimental tests of sub-components for certification. These improvements include using different damage initiation formulations and failure criteria (including a strain rate dependent failure criterion as well as an algorithm to determine the critical fracture plane) based on damage mechanics, along with damage evolution based on continuum damage mechanics.

Based on the pointed out goals, this work will aim at the following objectives:

- Gain a sound understanding of what crashworthiness is and the relative regulatory framework concerning civil aviation;
- Explore the features of composite fuselages and the respective energy absorbing parts;
- Probe different composite failure mechanisms including both intra and inter-laminar damage as well as several failure criteria to do so;
- Develop three different VUMAT, based on different failure criteria and strain rates, amenable to be employed in a 3D element formulation and validate them with benchmark literature;
- Investigate if the use of the developed routines and modeling strategy leads to an increase of accuracy of a high-energy impact simulation of a composite fuselage stanchion by comparing it to experimental and literature results.

1.2 Thesis outline

This thesis has been divided into seven different chapters. A concise chapter content overview is listed below:

Chapter 1 is relative to the introduction, where the overall context, motivation, and objectives of this work are contained.

Chapter 2 introduces the fundamental notions of crashworthiness and explores the corresponding regulatory framework within the field of aeronautics. Other basic concepts such as building block approach and experimental testing and design methodologies are also presented.

Chapter 3 provides a theoretical background of the composite failure mechanisms including intra and inter-laminar damage and some failure criteria that have been created to predict it. Their respective numerical implementation on the finite element solver software (via VUMAT), while providing some insights on element formulation and the explicit and implicit scheme, is also explained.

Chapter 4 contains the numerical verification of the three different implemented failure criteria, were a simple patch test is conducted to evaluate if they are predicting the expected behaviour.

Chapter 5 focuses on the validation of the developed VUMAT. It can be divided into two separate composite damage benchmark tests: Open Hole Tensile (OHT) test and one low velocity impact test. Regarding the latter, a sensitivity analysis is performed to evaluate the influence of both hourglass control methods and step viscosity, providing a brief explanation of both concepts.

Chapter 6 presents the numerical analysis of a composite stanchion under three different regimes: Quasi-static, low velocity impact and high velocity impact, being special focus given to the last one. The obtained numerical results are compared to the experimetnal results and other numerical simulations available on the literature.

Chapter 7 covers the obtained conclusions from all the work carried on this thesis. Additionally, some future work is recommended to continue and/or improve the contributions achieved in this work.

2 Literature review

2.1 Crashworthiness

In this chapter, a brief introduction of what is crashworthiness is made. Then, focusing on aeronautics, the regulations, design methodologies, and respective experimental tests are presented.

2.1.1 Definition

Despite vehicle occupant safety had been an issue since the late 1800's, it was not until the early 1950's that the term crashworthiness was used for the first time, curiously, in the aerospace industry [8].

The definition of crashworthiness can be seen as the ability of a structure and any other of its parts to protect the occupants in survivable crashes. In fact, this term can be applied to several vehicles such as automobiles and aircraft, since some of the underlying principles are shared (eg., maximizing impact energy absorption, maintenance of passenger compartment, etc.) [8–10], however, in this work, aeronautics will be the main focus.

Bearing civil transportation in mind, crashworthiness comes as the ability of an aircraft structure to protect the occupants in an emergency landing event or crash (most common survivable accidents) [11, 12].

2.1.2 Regulations

In order to ensure the safety of civil aviation, the regulatory bodies such as EASA (European Union Aviation Safety Agency) and the FAA (Federal Aviation Administration) established a set of requirements that need to be fulfilled for aircraft/rotorcraft to be certified. For the case of large passenger aeroplanes, these regulations can be found on CS-25/ FAR 25 [4, 5] which are regularly amended based on previous experience and operational data.

Directly related to the crashworthiness of the aircraft there are two sections (under the Emergency Landing Conditions chapter): CS 25.261 "General" and CS 25.562 "Emergency landing dynamic conditions".

While the former establishes the requirements, (such as inertial forces and cabin equipment positioning), to maximize the chance of occupants escaping serious injury in a minor crash landing, the latter addresses the seats design and body forces that the seatbelts and anthropomorphic test dummies are allowed to exert and suffer, respectively, during dynamic tests (given that the seat belts are properly being used).

2.1.3 Composite Regulations

Although the previously presented rules do cover the necessary requirements for the crash behaviour of the structure, they reflect what is expected from a typical metallic

structure, since up to date, is the one that the regulatory bodies and manufacturers have more information about, either through direct testing or previous accidents that have been investigated [6].

However, as the aviation industry strives to reduce its effect on global warming and maintenance costs, the use of composite materials, due to their high specific strength, and excellent fatigue and corrosion resistance, resulting in the reduction of weight and longer inspection times windows, has been increasing over the years, as seen on Figure 2.1 [13, 14].

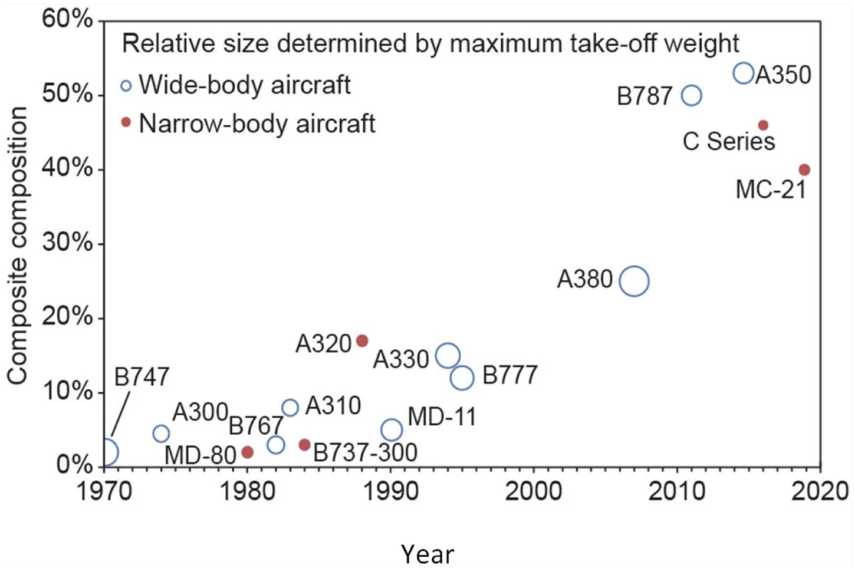

Figure 2.1: Evolution of composite composition from 1970 to 2020 [14].

In fact, although the use of composites on primary structural components was a lengthy process (nearly 40 years after their first use) [13], now, recent aircraft such as the Boeing 787 or the Airbus A350 have about 50% of their weight composed by composite materials, being them used for primary structures such as fuselage skin and frames [13–15].

This poses a challenge for the manufacturers, since carbon fibre reinforced polymers (CFRP) present a different impact absorption behaviour than conventional metallic materials. While plastic deformation is seen as the principal kinetic energy absorption mechanism for the latter, CFRPs dissipate it mainly by intra- and inter-laminar damage mechanisms (eg.,matrix cracking, fibre breakage, delaminations, etc.) [16–22] which may lead to a completely different structural behaviour and passenger inertial loads [7, 22, 23].

To address this issue, an Advisory Circular, AC 20-107B was put forward by the FAA (equivalent to the AMC 20-29 by the EASA) to provide guidance and support on how to meet the pre-established requirements for designs involving the use of composite materials, including not only manufacturing and process controls but also structural design recommendations [6].

One of the mentioned sections in the documents, refers to the crashworthiness of the aircraft which anticipates the use of "Special Conditions" (SC) for large aircraft with composite fuselages.

Special Conditions are a set of specific regulations that apply to a particular aircraft design, whenever the aiworthiness regulations (whether for structure, engines or systems), do not offer appropriate safety standards, mainly due to the novelties being used [24].

The special conditions for both Boeing 787 and Airbus A350 (25-362-SC and 25-537-SC respectively) state that these models need to provide an equivalent level of occupant safety to that of previously certified wide body transport aircraft. To do this, the proposed models should meet a set of criteria for impacts of vertical velocities up to 30 ft/sec [7]. The four criteria to be assessed are:

1. **Retention of items of mass**
   The occupants, i.e., passengers, flight attendants, and flightcrew, must be protected during the impact event from release of seats, overhead bins, and other items of mass caused by the impact loads and resultant structural deformation of the supporting airframe and floor structures. The applicant must show that loads due to the impact event and resultant structural deformation of the supporting airframe and floor structure at the interface of the airplane structure to seats, overhead bins, and other items of mass are comparable to those of previously certificated widebody transports of similar size for the range of descent velocities stated above. The attachments of these items need not be designed for static emergency landing loads in excess of those defined in § 25.561 if impact response characteristics of the aircraft[1] yield load factors at the attach points that are comparable to those for a previously certificated wide-body transport category airplane.

2. **Maintenance of acceptable acceleration and loads experienced by the occupants**
   The applicant must show that the impact response characteristics of the aircraft[2], specifically the vertical acceleration levels experienced at the seat/floor interface and loads experienced by the occupants during the impact events, are consistent with those found in § 25.562(b) or with levels expected for a previously certificated wide-body transport category airplane for the conditions stated above.

3. **Maintenance of a survivable volume**
   For the conditions stated above, the applicant must show that all areas of the airplane occupied for takeoff and landing provide a survivable volume comparable to that of previously certificated wide-body transports of similar size during and after the impact event. This means that structural deformation will not result in

[1] In the official document, the word "aircraft" is substituted by the name of the model that the Special Conditions apply to.

[2] See footnote 1.

infringement of the occupants' normal living space so that passenger survivability will not be significantly affected.

4. **Maintenance of occupant emergency egress paths**
   The evacuation of occupants must be comparable to that from a previously certificated widebody transport of similar size. To show this, the applicant must show that the suitability of the egress paths, as determined following the vertical impact events, is comparable to the suitability of the egress paths of a comparable, certificated wide-body transport, as determined following the same vertical impact events.

In order to show compliance to these requirements, the Original Equipment Manufacturers (OEMs) should employ either analysis through validated analytical tools (virtual models) or direct-test evidence, also known as drop tests [7].

2.2 Drop Tests

2.2.1 Testing requirements

Drop tests, as previously mentioned, are a crucial tool to evaluate the crashworthiness of a proposed design/structural solution. In fact, the results of the tests do not only provide valuable data for certification purposes, but they also allow to evaluate and tune numerical models that may have been created [25].

The selection of the test article should take into account three different parameters:

- **Selection of Fuselage Section**
  The test article should represent passenger areas of the plane and, in general, should include all the features that may influence the crash response of the structure (having specific design features not necessary to be included if not expected to influence the results). Wings do not need to be included unless the aircraft has a high-wing configuration, where a ballast weight can be used to simulate maximum landing weight and 1 g wing lift for high-wing design sections [26].

- **Appropriate Boundary Conditions**
  Open ends of the test article may need to be reinforced to appropriately simulate the stiffness of a complete fuselage. It should be long enough to allow the accommodation of adjacent rows of certified seats and the overhead structure must be installed with the maximum allowed weight. For an emergency exit section, seats and maximum overhead and underfloor luggage mass should be considered to assess the deformation in the most severe case.

- **Representative Stiffness and Cargo Configuration**
  If the under floor compartment is to be used for luggage or cargo, the test article should include the most critical configuration (ballast weights can be used for this

purpose). Depending on the section, cargo door structure may be required do adequately simulate the difference in stiffness relatively to a regular fuselage section.

To assess accelerations and lumbar load limits addressed in the regulations, anthropomorphic test dummies should be used, alternatively, if the test does not envision seats, airframe accelerations may be used to show compliance with the injury limits [26].

Additional equipment such as accelerometers at the seat tracks, frames and/or on other critical junctions and the use of strain gauges/Digital Image Correlation (DIC) may be helpful to measure the fuselage response to the test. However, high speed video cameras must be used to validate the maintenance of the required survivable volume and retention of items of mass throughout the test [26].

The impact surface should be rigid and the fuselage section should be dropped vertically at zero pitch angle (although some variations may be considered to evaluate specific energy absorbing features [27]) at an height which results in impact velocities in accordance to the requirements [26].

2.2.2 Conducted tests

Despite their importance for the assessment of structural performance under accidents, drop tests were not the first full-scale crash tests being conducted. In fact, the first tests, performed by NACA in the late 1950s and the 1960s, consisted in submitting the aircraft to horizontal impact such as crash barriers and hills to simulate specific situations such as off-airport landings [28].

From the 1970s forward, vertical drop testing started being used, mainly by the FAA and NASA beginning with the crash dynamics development programme [28]. In the 1980s, NASA Langley Research Center conducted several drop tests for different sections of the the B707 fuselage (i.e. forward and after the wing and middle sections) [29–31].

In 1984, within the scope of the CID (Controlled Impact Demonstration) research programme, a full-scale impact test of a remotely piloted B720 was conducted (Figure 2.2) [32].

Figure 2.2: CID full-scale crash test of a B720 [32].

It allowed to assess both the maturity and integrity of the data acquisition systems as well as to validate finite element models.

Between 1993 and 1999, three fuselage sections of the A320 were drop tested in the frame of the "Crashworthiness for commercial aircraft" European programme [28, 33, 34]

In 1999, the FAA conducted a 30 ft/sec vertical drop test of 10-foot section of a B737 fuselage with a conformable auxiliary fuel tank. A similar test was performed in 2000, but this time, the fuselage was fitted with overhead stowage bins and the fuel auxiliary tank was replaced by luggage [35]. The obtained results (Figure 2.3) were later used to evaluate the capabilities of the available computational tools [35].

(a) (b)

Figure 2.3: Vertical drop tests of two B737 fuselage sections (a) with conformable auxiliary fuel tank (b) with overhead bins and luggage [35].

In 2001, two sections (forward and after wing) of a YS-11 transport aircraft and a section of a F28 fuselage (Figure 2.4) were drop tested (impact velocities of 20 and 30 ft/sec respectively) by the National Aerospace Laboratory of Japan (NAL) and by the Langley Research Center correspondingly, with the objective of assessing both structural performance under realistic crash conditions and to validate/improve FEM models, which for both cases showed good correlations with the test article [36, 37].

On July 30, 2003, an ATR 42-300 was drop tested (Figure 2.5) from an height of 14 ft, which lead to an impact velocity of 30 ft/sec. The test conducted by the FAA, had as primary objectives to assess the impact response of the fuselage, fuel systems, anthropomorphic test dummies, etc. under a severe, but survivable crash impact [38].

It was concluded that, for this drop height, the fuselage did not comply with the regulations (both at the structural level and inertial forces suffered by the passengers) [38].

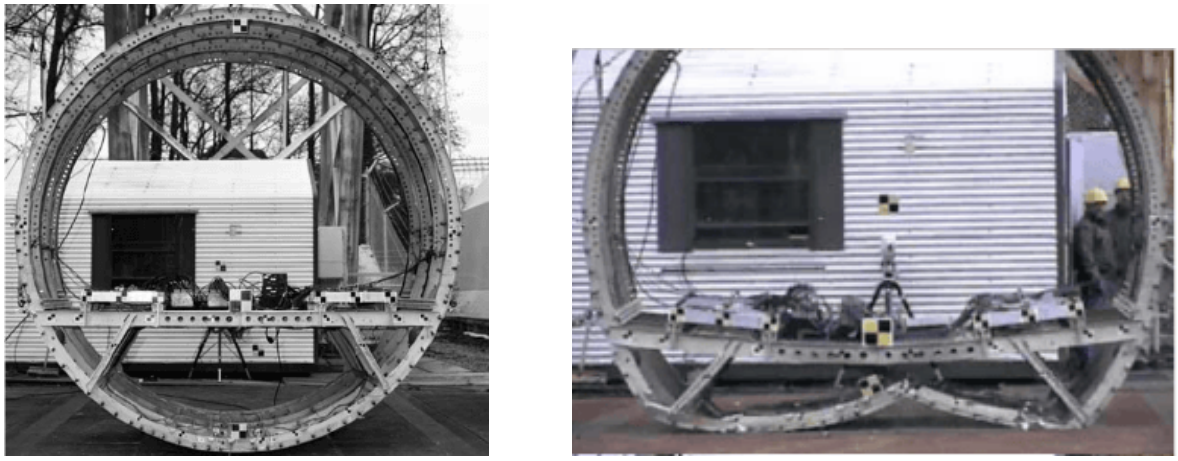

(a) (b)

Figure 2.4: Fokker F28 impact test conducted at NASA Langley Research Center (LaRC) Impact Dynamics Research Facility. (a) undeformed and (b) deformed fuselage section [37].

Figure 2.5: Aftermath of the ATR 42-300 drop test with visible extensive damage [38].

In 2012, a vertical drop test (22.5 ft/sec) of a fuselage section with seats, anthropomorphic dummies and overhead stowage bins (Figure 2.6) was conducted at ASRI (Airplane Strength Research Institute), China, with the intent of validating a previously developed finite element model of the structure [39].

In 2017, two F28 fuselage sections (forward with luggage and wingbox) were drop tested at NASA LaRC's Landing and Impact Research Facility, once again to investigate the structural behaviour of the aircraft in a survivable accident [40].

From the test data, it was possible to conclude that luggage can have a great influence on the overall response of the structure [40].

More recently, in 2019, a 20 ft/sec drop test conducted by the CAUC (Civil Aviation University of China) to validate a simulation of the fuselage section [11].

In the same year, as part of a joint NASA/FAA project, a full-scale crash test of a F28 was conducted to evaluate the crashworthiness of transport aircraft and to obtain data for model validation [41]. The results of the impact test can be seen of Figure 2.7.

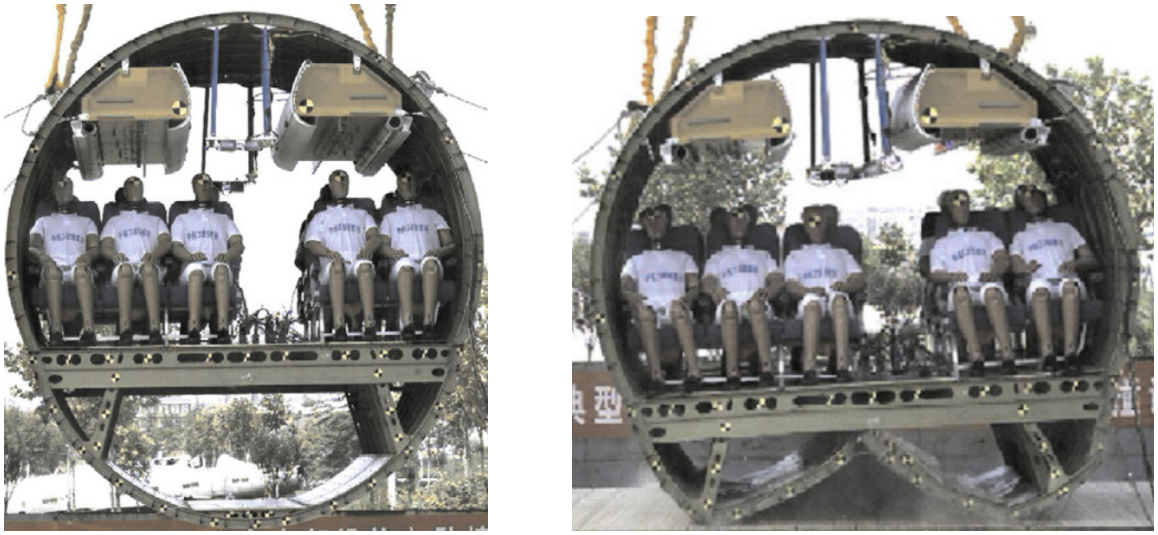

(a) (b)

Figure 2.6: Fuselage section with internal facilities drop test. (a) undeformed and (b) deformed fuselage section [39].

Figure 2.7: Full-scale crash test of a F28 [41].

In 2021, the National Institute for Aviation Research (NIAR) at the Wichita State University, conducted a Bombardier Challenger 601 fuselage drop test [42].

2.2.2.1 Composite fuselage drop tests

Crashworthiness investigation of composite fuselage structures began in the late XX century, stating with smaller components such as composite sub-floor absorbers and frames [43]. However, it was only in 2007 that a civil airliner composite fuselage was tested by the Boeing company. A 30 ft/sec drop test was conducted in order to assess if the new and innovative design complied with the regulations (i.e. presented similar crashworthy characteristics than a regular matallic counterpart) [11].

Ten years later, in 2017, a regional aircraft full-scale composite fuselage section was drop tested at a velocity of 30 ft/sec (Figure 2.8) in CIRA (Italian Aerospace Research Centre) in order to evaluate both the validity of numerical models and structural response/passenger survivability [12].

Figure 2.8: Deformed composite fuselage section of a regional aircraft [44].

In the same year, a 30 ft/sec impact test of a Hawker 4000 fuselage was performed at the NIAR Crash Dyanmics Laboratory to assess the adequacy of the structure to the pre-established regulations [42].

In their work, Mou et al. [11] have compiled and arranged the majority of the documented drop tests in chronological order. For the sake of clarity and completeness, in this work, the distinction between composite and metal fuselage is done as well as the introduction of new experiments that have meanwhile been made (Figure 2.9).

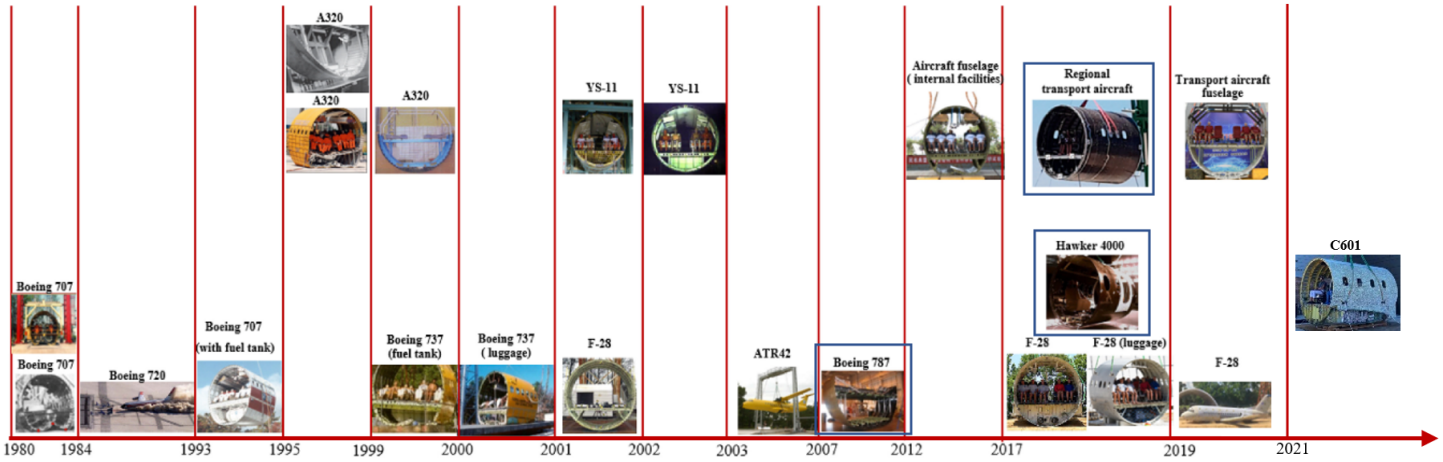

Figure 2.9: Drop tests through the years differentiating composite fuselage sections (square). Adapted from [11].

As it can be observed, there is still limited research on composite fuselage impact response, compared to the numerous tests that have been already preformed for conventional metallic solutions.

This reduction may also be due to the higher maturity of numerical tools, which, may reduce the necessity of such intensive experimental testing, however, the latter will be most certainly needed to attain validation.

2.3 Fuselage Energy Absorption Structures

Given that the fuselage is the aircraft component that will generally impact the ground first in an emergency landing (considering the failure of the landing gear), it is of uppermost interest to include features capable of absorbing some impact energy on its structure [11].

2.3.1 Fuselage

The fuselage of a typical transport aircraft has a semi-monocoque configuration, meaning its outer structure is constituted by an exterior skin, frames and longitudinal stringers, being the last, the difference relatively to a true monocoque configuration [45].

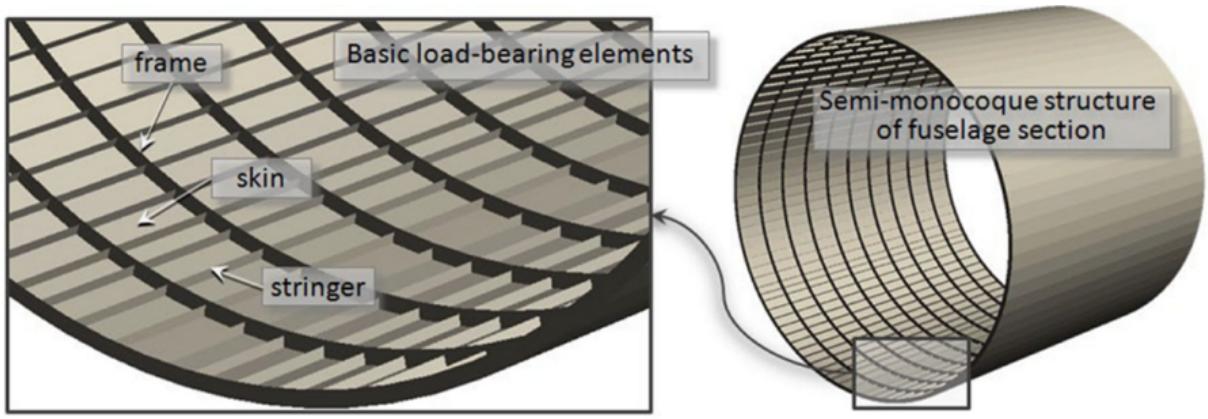

Figure 2.10: Semi-monocoque configuration [46].

On the other hand, the interior sections of the fuselage can be divided in three separate parts: a cabin compartment, where the passengers are located, a cargo compartment, where the cargo is stowed, and a sub-cargo area, as seen on Figure 2.11 [47].

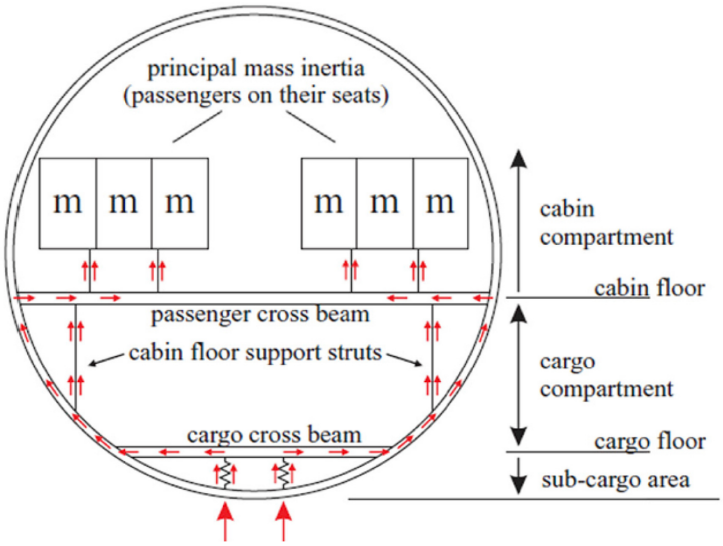

Figure 2.11: Fuselage sections and respective load path in case of impact [47].

During an impact event, while the structures above the cabin floor need to maintain the cabin integrity, to comply with the aforementioned regulations, the lower part structures, specially the sub-cargo ones, need to absorb as much as energy as possible, either through deformation or destruction, to reduce the loads transmitted to the passengers [11].

2.3.2 Sub-cargo area

The sub-cargo area is the main energy absorption zone and it can have different layouts, specially on how the cargo cross beams are connected to the below fuselage skin structure. These structural solutions, such as sine-wave beams, corrugated webs or stanchions (Figure 2.12), are dependent on the model of aircraft or rotorcraft being made [11, 48]. However, regarding composite civil aircraft, the latter are preferred [11] and thus, will be the main focus in the next section.

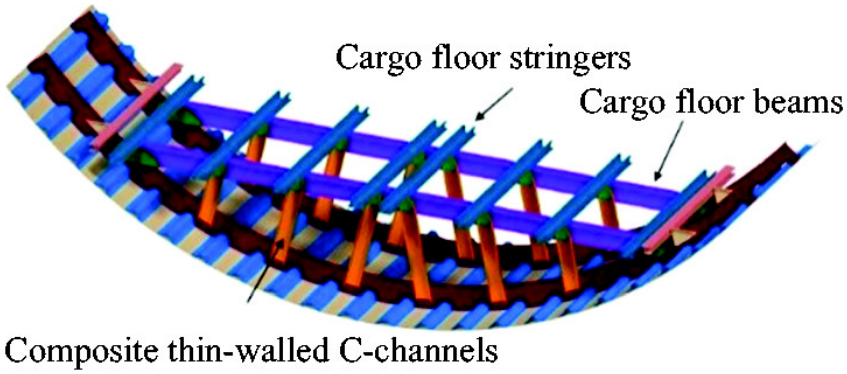

Figure 2.12: Sub-cargo structure [49].

2.3.3 Stanchions

Thin-walled columns, specially open-section columns, such as C section (Fig. 2.13), are common structures to serve as energy absorbers in crash events due to their long axial crushing distances [48, 50, 51].

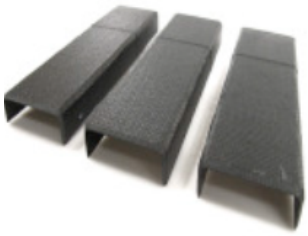

Figure 2.13: C section stanchions [11].

In fact, in the last years, there has been a significant amount of research on structures of this type made of composite materials [49], since their implementation would allow the reduction of weight and to possibly obtain higher energy absorption efficiency than regular aluminium tubes [52].

However, behaving differently than metals, composites have different and more complex damage mechanisms that affect the damage absorption capability (Figure 2.14), which several authors have tried to characterize [53–55]. To this end, many experimental tests have been and are being done to further understand their behaviour [49, 56, 57].

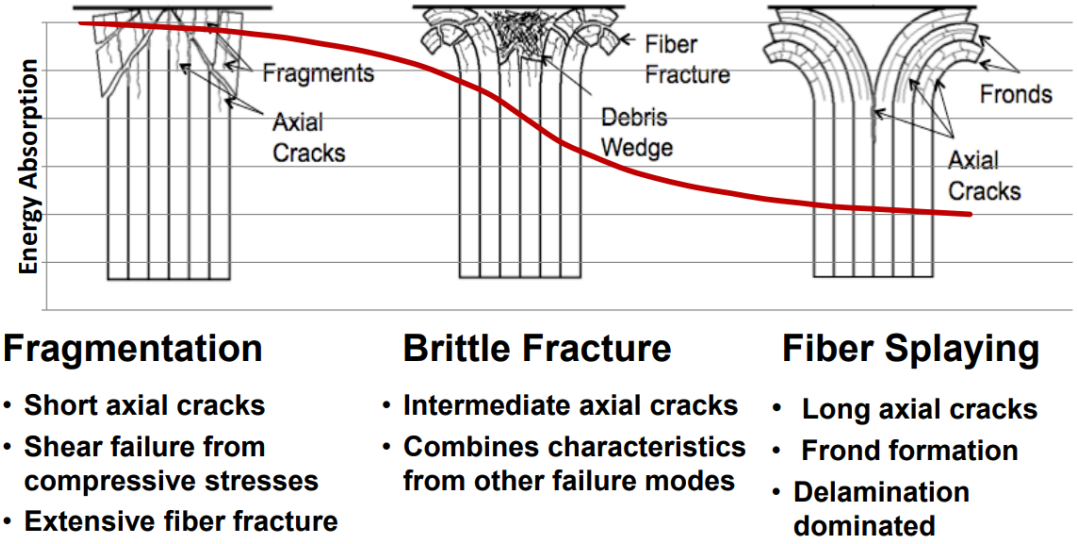

Figure 2.14: Relation between energy absorption and failure mechanisms [56].

The crush tests are the most important regarding this kind of structure and allow to generate force-displacement curves, which are useful since they allow the estimation of the absorbed energy. Usually, these curves lead to configurations similar to the one in Figure 2.15.

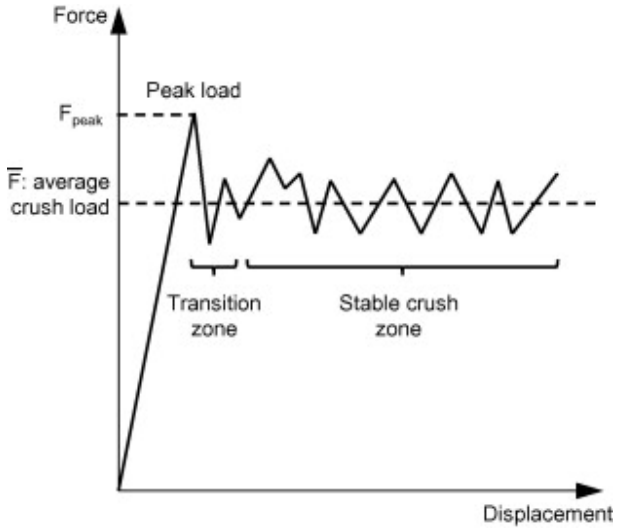

Figure 2.15: Typical load-displacement curve [57].

As it can be seen, the curve can be divided into three stages: a peak stage, where the compressive load reaches the highest value, an usually small transition phase and

a final third phase where the load oscillates around an average value and where the majority of energy is absorbed [57].

From this graph, some useful crashworthiness indicators such as the mean force or the specific energy absorption (SEA), which allows to assess the absorbed energy per unit of mass can be obtained [49]. The respective equations of these two measures can be found below:

$$F_{mean} = \frac{\int F\,dl}{L} \tag{1}$$

$$SEA = \frac{\int F\,dl}{\rho A L} = \frac{F_{mean}}{\rho A} \tag{2}$$

where F is the force, L, the total crushing distance, ρ, the density and A the cross sectional area.

2.4 Building Block Approach

As aforementioned, drop tests, besides being expensive and time consuming, also present high variability in their results, consequently, OEMs have great interest on acquiring reliable computational tools which allow the simulation of different boundary conditions and other experimental variables before having to actually perform the test [58].

Despite the immense potential of computational tools, for new and innovative solutions, specially regarding composites, all the geometries, materials and/or manufacturing processes should be addressed and previously validated through test evidence [26]. For this validation, the AC 20-107B strongly suggests a building block approach (Figure 2.16) [6, 59]

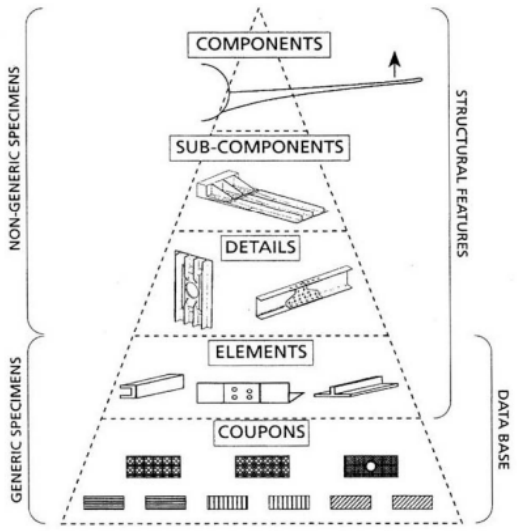

Figure 2.16: Schematic of building block approach for a fixed wing component [6].

Following this methodology, it is expected that testing will be carried from the lower to the higher level of complexity of an aircraft component, being knowledge gained from previous "steps" applied on the next ones, reducing the number of specimens tested along the way [60].

In order to validate a composite structure, both experimental and numerical tests (and their respective comparison) need to be performed for coupons, elements, details, sub-components and components, culminating with full-scale aircraft testing (Figure 2.17).

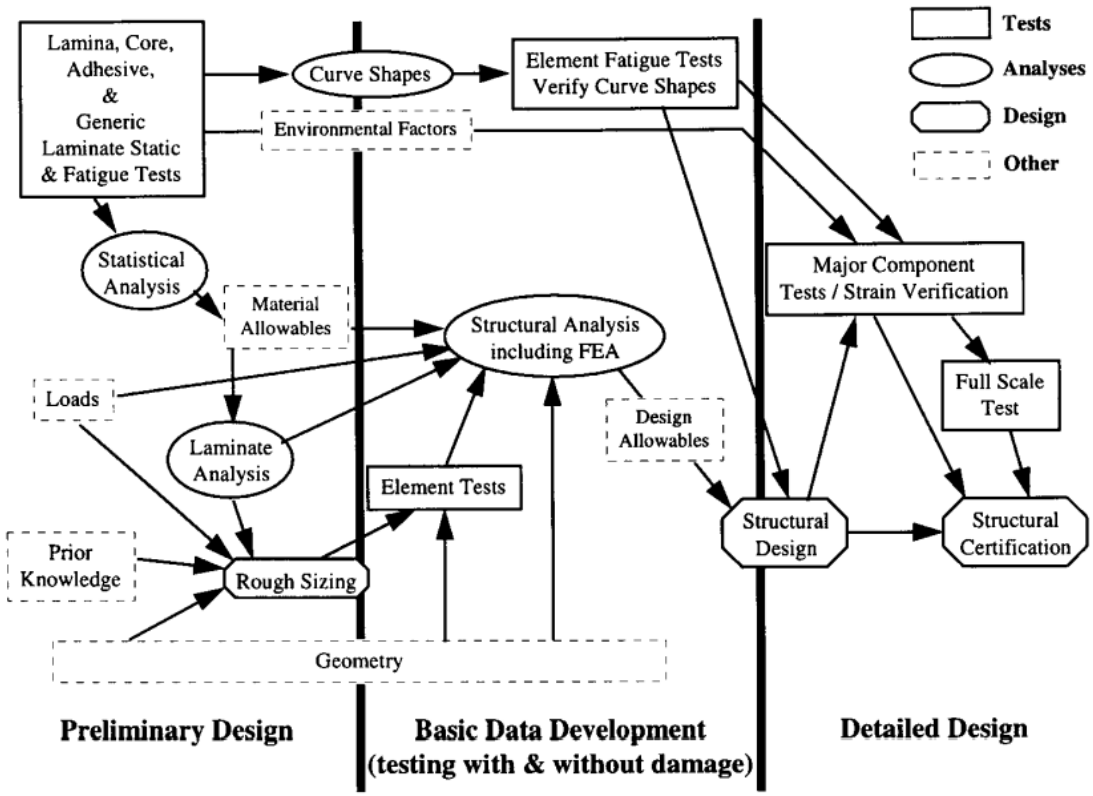

Figure 2.17: Typical building block program flow [60].

In the next sections, a small introduction to each step of the pyramid will reported, while referencing some tests that are performed regarding the crashworthiness behaviour of each specimen.

2.4.0.1 Coupons

Testing at the coupon level is a very important step for the appropriate definition of the material behaviour and properties [59, 61].

Through an exhaustive experimental campaign, composed of different test cases (e.g., tension, compression, shear, etc.) and numerous specimens, the material mechanical properties and failure modes can be determined and analysed [11, 62]. A schematic of some of these tests can be seen on Figure 2.18.

It is also at this stage where the material allowables are generated, through a statistical analysis of the results [59, 63].

Regarding crashworthiness, some variables such as damage evolution parameters for different conditions and strain rates are essential for the development of an accurate failure model and assessment of energy absorption characteristics [64].

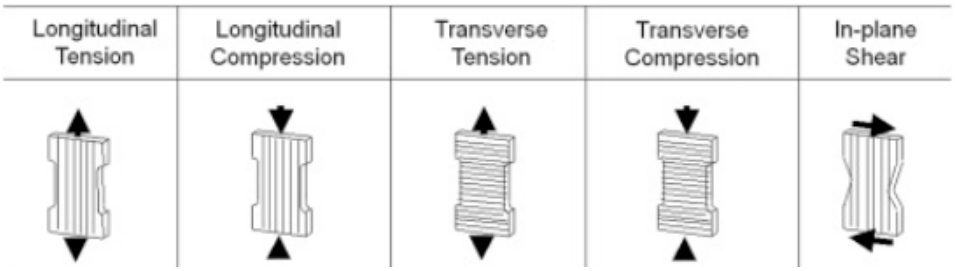

Figure 2.18: Examples of standards for composite coupon testing [65].

Also at the coupon level, different types of connectors such as single (Figure 2.19) and double lap joints are tested under several loading conditions and some other tests such as bolt pull-through are considered. This is also a crucial step since the failure of fasteners account for a large portion of the total energy, due to their elasto-plastic characteristics [11, 66, 67]. The appropriate characterization of their behaviour is essential not only for the determination of the energy associated with the failure of the fastener but also to characterize the different failure modes of the composite laminate [60].

Figure 2.19: Examples of single lap shear tests [68].

2.4.0.2 Structural Elements

Fuselage elements such as stanchions, columns, clips and frames, have proven to be extremely important when it comes to energy absorption mechanisms [48]. Element testing (Figure 2.20) is then essential to determine elementary failure modes and load-deflection curves which ultimately allow to predict/estimate the energy absorption and crashworthy characteristics [26]. It is also at this stage where design values are derived for the selected structural configuration as well as the assessment of the sensitivity to manufacturing parameters and defects [60].

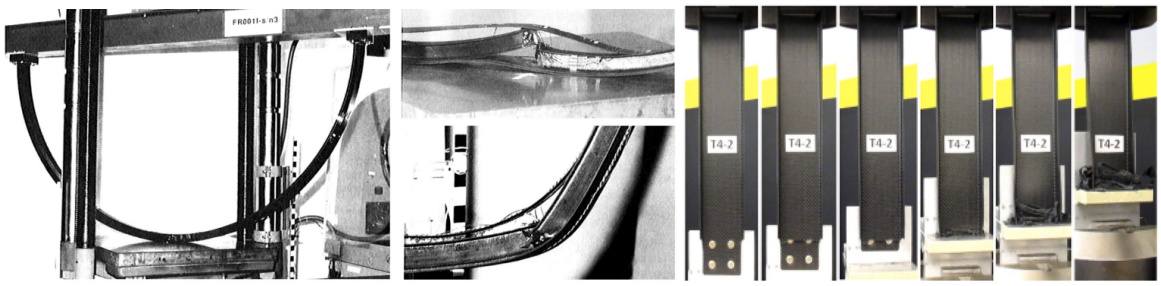

(a) (b)

Figure 2.20: Crashworthiness tests of (a) frames and (b) stanchions [11, 69].

2.4.0.3 Details

Tests on design details of an aircraft help to establish the fundamental failure modes, damage sequences, and energy absorption characteristics of the features. Sub-floor webs, sub-floor energy absorption structures, and fuselage panels are examples of such features [11, 26].

2.4.0.4 Sub-Components

Sub-components are typically sections of a components and tests are conducted to evaluate the failure modes and failure mechanisms as well as possible load redistribution and energy absorption capabilities of the proposed structure [26, 60]. The performed tests can be either dynamic or static (with more representative boundary conditions due to specimen complexity) and the specimen may include assembly features such as stringers, clips, frames, etc.

One example of a sub-component is the sub-cargo fuselage section, previously mentioned on section 2.3.2, being extremely important regarding the crashworhtiness of the aircraft [11, 26, 59].

Being the main energy absorption zone, given it is the first structure making contact with the ground surface during a crash landing, costly dynamic tests are performed to evaluate its overall structural behaviour and crashworthy performance. These crash tests can be either forward, where the structure is dropped from a specific height, or inverted, where a weight is dropped on an upside-down structure, as seen on Figure 2.21, being the latter more common and easier to control [11].

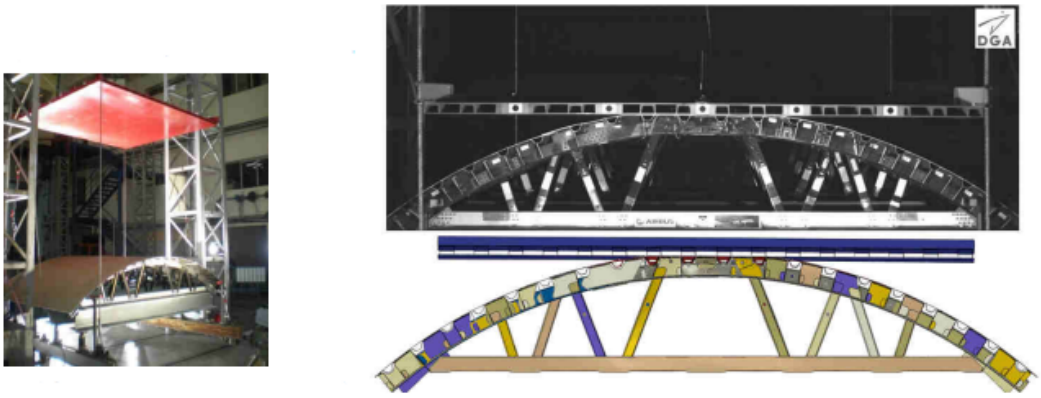

Figure 2.21: Inverted impact test of an A350 sub-cargo structure [70].

2.4.0.5 Components

At the top of the pyramid are component tests. These are made with a representative specimen of the final structure (e.g. fuselage sections as presented in Section 2.2.2). These types of tests are complex and typically resource-intensive, both in terms of cost and time and generally are performed to validate previous analytical calculations.

As a summary, an example of a composite fuselage building block crashworthiness oriented approach is shown on Figure 2.22.

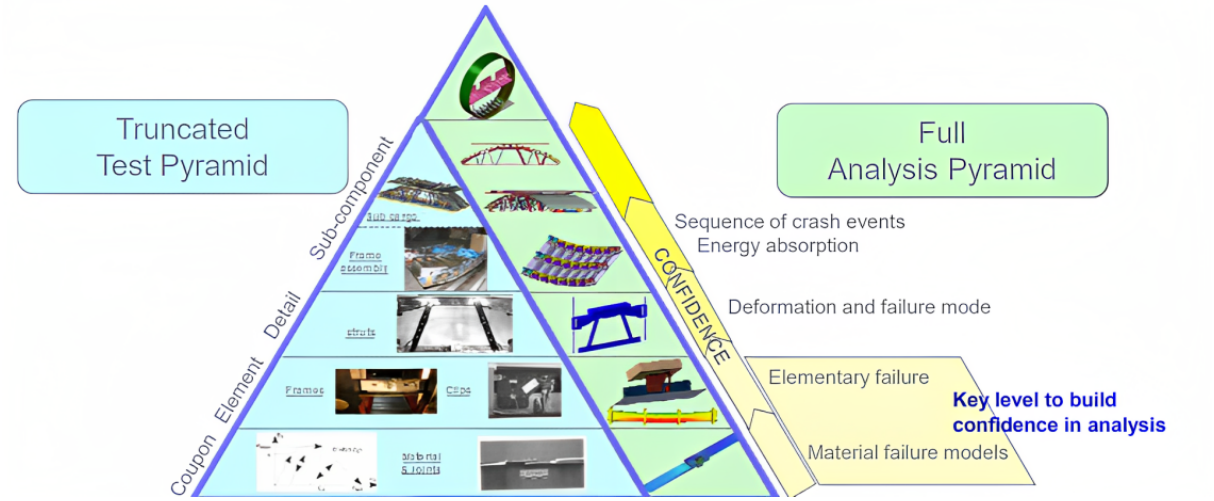

Figure 2.22: Crashworthiness building block approach of an A350 fuselage [70].

It is important to note that finite element simulations follow the experimental tests (shown as truncated test pyramid), this way, the confidence on the numerical results is improved given they are validated step-by-step with increasing complexity.

3 Theoretical Background and Numerical Implementation

Energy absorption capabilities of composite structures are heavily dependent on their damage mechanisms. Given so, it is of paramount importance to assess and characterize those damages in order to establish reliable models which can be later implemented in virtual simulations [57, 71].

There are different damage modes in laminated composites which can be divided into two main categories: intra-laminar and inter-laminar. Intra-laminar damage occurs within the plane of the individual plies and encompasses fibre dominated failure such as fibre breakage, fibre pullout, and fibre buckling, as well as matrix dominated modes like matrix cracking and fibre-matrix splitting. On the other hand, inter-laminar damage refers to the separation of two adjacent layers in a laminate stack, commonly known as delamination [72].

Frequently, distinction is made between the matrix and fibre dominated modes, addressing the former as translaminar damage [73], however in this work, the term intra-laminar damage will be used for both cases. Figure 3.2 summarizes the mentioned failure modes.

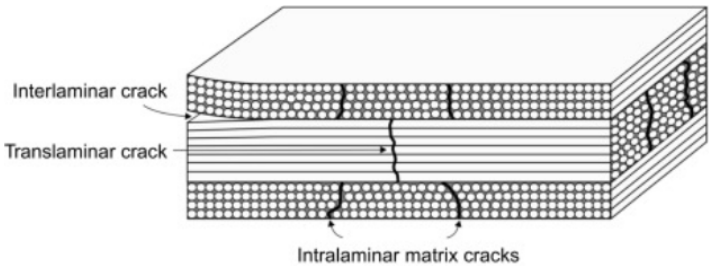

Figure 3.1: Inter, intra and translaminar failure modes [73].

In this chapter, several intra-laminar damage models (initiation and evolution) will be presented, with special emphasis on the Hashin, a modified Hashin-Puck and a Strain Rate Dependent Hashin based failure criteria, which are the ones being used in this work, while for the inter-laminar damage, the Cohesive Zone Model (CZM) will be the main focus.

3.1 Intra-Laminar damage

Being the driver of composite ply failure, intra-laminar damage can be divided into a set of different failure modes: fibre tension, fibre compression, matrix tension, matrix compression and shear failure of the matrix, which are represented on Figure 3.2.

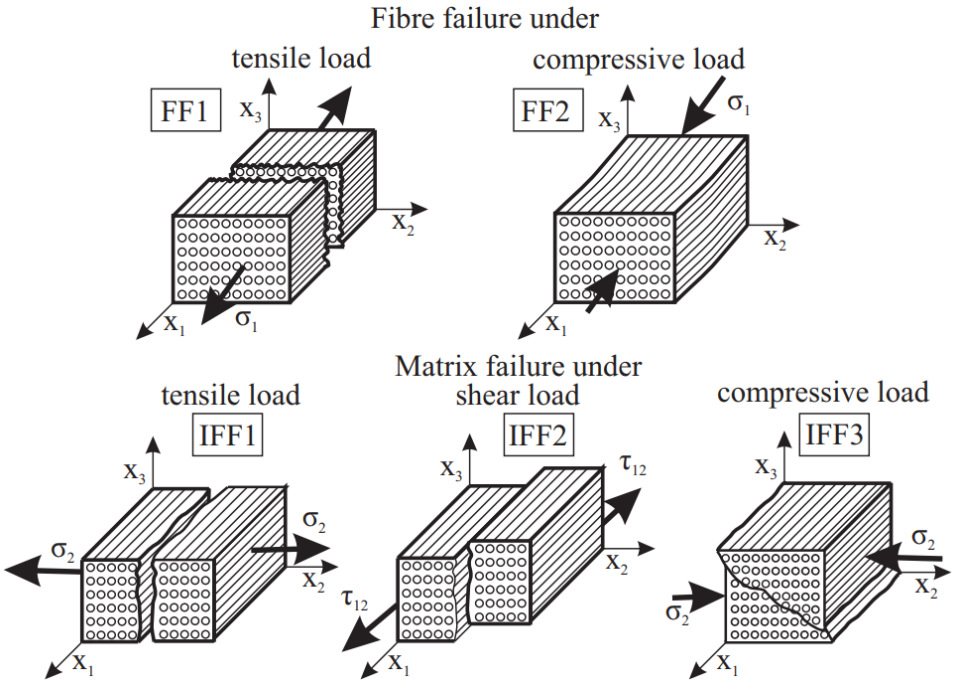

Figure 3.2: Composite failure modes [74].

Also in the figure there are missing some failure modes such as fibre pull-out or fibre-matrix debonding [72].

Once damage is initiated, there is a reduction in stiffness owing to the loss of load carrying capability of the damaged material, whether is the fibre or the matrix. To account for this loss of stiffness, usually a distinction is made between the start of material damage (Damage onset) and the respective stiffness degradation (Damage evolution) [75].

3.1.1 Damage onset

In order to predict the onset of intra-laminar damage, several theories have been developed by different authors [76–83].

These failure criteria can be divided into two major categories: phenomenological and non-phenomenological failure criteria. The main difference between them is the ability of determining the mechanism associated with the failure. Phenomenological criteria, besides being able to predict the damage onset, are physically based and thus, able to identify what failure mechanism was involved while non-phenomenological failure criteria also determine the damage onset but at an overall level, not being able to disclose the failure mode behind it [84]. The latter are also generally closed-form solutions and therefore computationally inexpensive.

On Table 3.1, a set of different non-phenomenological and phenomenological criteria can be found.

Table 3.1: Phenomenological and non-phenomenological failure criteria.

Non-phenomenological	Phenomenological
Maximum Stress	Hashin [85]
Maximum Strain	Puck [79]
Tsai-Hill [77]	LaRC 3D [82]
Tsai-Wu [76]	3D invariant-based [83]

Hashin Failure Criterion

The first criterion that will be presented is the 3D Hashin Failure Criterion developed by Hashin in 1980 [85]. The method is based on a quadratic approximation of the failure surfaces as seen in Figure 3.3, which, do not hold any physical meaning, being only a good fit of experimental data [85].

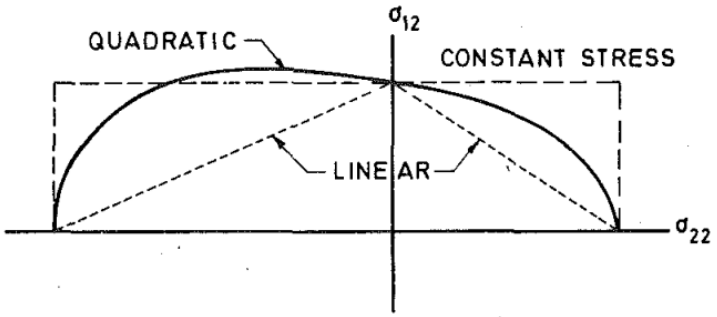

Figure 3.3: Linear an quadratic approximations of the failure surfaces [85].

This approximation, based on mathematical reasoning of the stress invariants for transversely isotropic materials [85], lead to the following set of equations:

- Fibre tensile failure ($\sigma_{11} \geq 0$)

$$F_{ft} = \left(\frac{\sigma_{11}}{X_T}\right)^2 + \alpha \left(\frac{\sigma_{12}}{S_{12}}\right)^2 + \alpha \left(\frac{\sigma_{13}}{S_{13}}\right)^2 \geq 1 \tag{3}$$

- Fibre compressive failure ($\sigma_{11} < 0$)

$$F_{fc} = \left(\frac{\sigma_{11}}{X_C}\right)^2 \geq 1 \tag{4}$$

- Matrix tensile failure ($\sigma_{22} + \sigma_{33} \geq 0$)

$$F_{mt} = \left(\frac{\sigma_{22} + \sigma_{33}}{Y_T}\right)^2 + \frac{1}{S_{23}^2}(\sigma_{23}^2 - \sigma_{22}\sigma_{33}) + \left(\frac{\sigma_{12}}{S_{12}}\right)^2 + \left(\frac{\sigma_{13}}{S_{13}}\right)^2 \geq 1 \tag{5}$$

- Matrix compressive failure ($\sigma_{22} + \sigma_{33} < 0$)

$$F_{mc} = \left(\frac{\sigma_{22} + \sigma_{33}}{2S_{23}}\right)^2 + \frac{\sigma_{22} + \sigma_{33}}{Y_C}\left[\left(\frac{Y_C}{2S_{23}}\right)^2 - 1\right] + \frac{1}{S_{23}^2}(\sigma_{23}^2 - \sigma_{22}\sigma_{33}) + \left(\frac{\sigma_{12}}{S_{12}}\right)^2 + \left(\frac{\sigma_{13}}{S_{13}}\right)^2 \geq 1 \tag{6}$$

Where, $\sigma_{ij}(i, j = 1, 2, 3)$ are the components of the stress tensor, X_T and X_C are the tensile and compressive strengths of the unidirectional laminate in the fibre direction, Y_T and Y_C are the transverse tensile and compressive strengths, S_{12},S_{13} and S_{23} are the shear strengths and α is the shear failure coefficient, which controls the contribution of the shear stresses on the fibre tensile failure, which, in this work, will be considered to be an unitary value [86].

As it can be seen, this criterion has a distinct failure condition function for each failure mode. This way, the prediction of the nature of failure of composite parts can be determined, contrarily to other non-phenomenological failure criteria.

However, it has been documented and widely accepted that Hashin criterion does not predict well the behaviour of composite plies under compression, both for fibre and matrix, since besides not considering the influence in shear strength under transverse compression it also does not take into consideration the effects of in-plane shear in fibre failure [81]

Modified Hashin-Puck failure criterion

In 2002, Puck and Schürmann [79] came up with a new failure criteria able to better predict failure, specially when matrix compression is involved. Therefore, in this work, a mixed failure criterion using Hashin's for the prediction of all the failure types but the matrix compression is developed.

The criterion considers that the matrix failure happens due to the instant creation of an Inter Fibre Failure (IFF) crack. The orientation of this crack varies accordingly to the load case as well as its severity, relatively to the laminate failure. It is based on Mohr-Coulomb hypothesis which is typically used for brittle fracture of quasi-isotropic materials and it considers that the failure is driven by stresses on a plane parallel to the fibres [79].

The fracture plane and the corresponding stresses, as seen in Figure 3.4, is in fact one of the infinite possibilities of fracture planes.

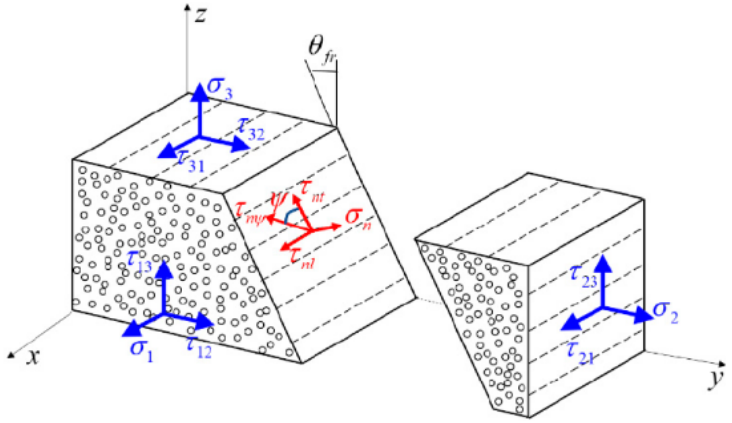

Figure 3.4: Potential fracture plane, respective orientation, θ, and stress components [87].

The orientation of the most favourably oriented fracture plane is dependent on the value of the failure index for each possibility.

To determine the failure index, it is necessary to determine the relations between the in-plane stresses on the fracture plane (σ_{nn}, σ_{nt} and σ_{nl}) and the stresses of the ply axes (σ_{11}, σ_{22}, σ_{33}, σ_{12}, σ_{23} and σ_{13}). These relations can be found on Equations [7-9].

$$\sigma_{nn} = \sigma_{22}\cos^2(\theta) + \sigma_{33}\sin^2(\theta) + 2\sigma_{23}\sin(\theta)\cos(\theta) \tag{7}$$

$$\sigma_{nt} = (\sigma_{33} - \sigma_{22})\sin(\theta)\cos(\theta) + \sigma_{23}(\cos^2(\theta) - \sin^2(\theta)) \tag{8}$$

$$\sigma_{nl} = \sigma_{13}\sin(\theta) + \sigma_{12}\cos(\theta) \tag{9}$$

The failure index, F_{mc}, is the defined by the following equation:

$$F_{mc} = \left(\frac{\sigma_{nt}}{S_{23}^A - \eta_{nt}\sigma_{nn}}\right)^2 + \left(\frac{\sigma_{nl}}{S_{12} - \eta_{nl}\sigma_{nn}}\right)^2 \tag{10}$$

where η_{nt} and η_{nl} are friction coefficients in the transverse and longitudinal directions, S_{23}^A is the transverse shear strength in the fracture plane and S_{12} is the longitudinal shear strength.

These parameters can be calculated via the following expressions:

$$\varphi = 2\theta - 90° \tag{11}$$

$$\eta_{nt} = \tan(\varphi) \tag{12}$$

$$S_{23}^A = \frac{Y_C(1 - \sin(\varphi))}{2\cos(\varphi)} \tag{13}$$

$$\eta_{nl} = \frac{\eta_{nt}}{S_{23}^A} S_{12} \tag{14}$$

To determine the fracture angle, θ, a numerical procedure needs to be followed, specially for 3D stress cases where the value of the failure index is difficult to predict analytically [88].

The failure angle is then searched between $-90° < \theta \leq 90°$ and is the one which maximizes the value of the failure index. However, having to calculate the trial fracture plane stresses for each iteration makes this method excessively computationally expensive.

To solve this issue, several algorithms have been suggested to more efficiently find the fracture angle, or at least a reasonable and with a good accuracy/computational cost relation approximation.

In this work, the Simple Parabolic Interpolation Search (SPIS) algorithm proposed by Rezasefat et al. [89] is used.

The method consists in dividing the total search interval in 18 different intervals bounded by 19 supporting points, evaluating the value of the failure index, F_{mc}, at each one of them.

After determining the failure index of the 19 supporting points, those which are neighbored by lower failure index valued points are isolated, this will allow the definition of sub ranges that most probably contain a local and/or global maximum.

Then, to neglect the local maxima, the isolated point with the highest failure index is taken while the others are discarded.

After defining the possible sub range containing the global maximum (constituted by the isolated and the respective neighboring points), the critical angle is estimated by a parabolic interpolation.

The overall procedure can be seen on Figure 3.5.

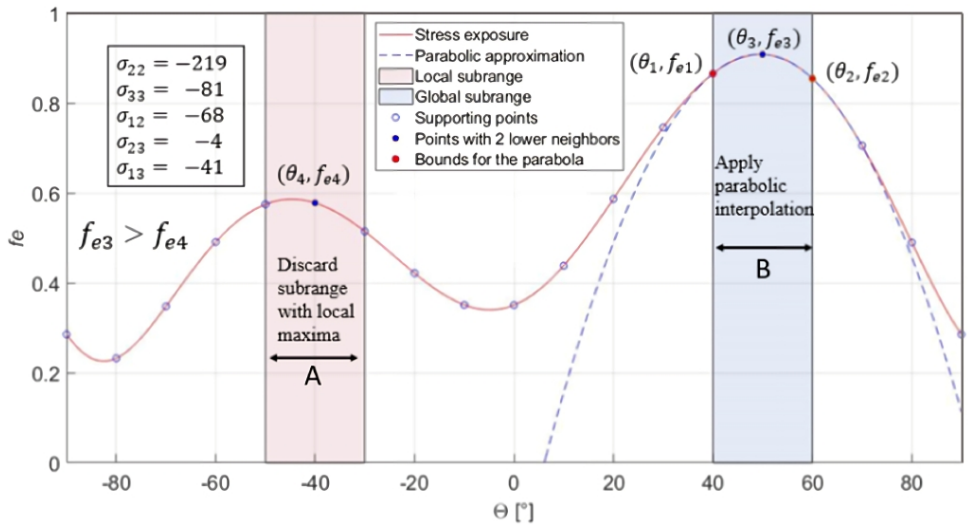

Figure 3.5: SPIS method for a specific 3D load case with two local maxima [89].

As observed, the isolated points are the f_{e4} and f_{e3}, having the latter a higher value of the failure index than the former, thus, meaning that the global maximum will be interpolated in the following interval $[\theta_1, \theta_2]$.

The parabolic interpolation is done via the following expression:

$$\theta_{cr} \approx \theta_2 - \frac{1}{2}\frac{(\theta_2-\theta_1)^2(f_{e2}-f_{e3})-(\theta_2-\theta_3)^2(f_{e2}-f_{e1})}{(\theta_2-\theta_1)(f_{e2}-f_{e3})-(\theta_2-\theta_3)(f_{e2}-f_{e1})} \tag{15}$$

Once the critical angle is estimated, its failure index is calculated and compared to the extreme cases which are not taken into account during the procedure, namely, $\theta = -90°$ and $\theta = 90°$. The failure index value for each time increment will be assumed to be the maximum value of these three last candidates.

Following this procedure, the fracture plane stresses only have to be calculated 19+1 times instead of 180 (considering a 1 degree resolution) substantially reducing the computational costs.

For the sake of simplicity, henceforth, this mixed criterion will be addressed as Puck criterion, despite the Puck formulation being only used for matrix compression.

Strain Rate Dependent Failure Criterion

It is widely known and established that some material properties change significantly with different values of strain rate, therefore, efforts have been made to develop more accurate material and failure models especially for the simulation of high speed loading such as crashes and impacts, highly relevant for the aerospace industry [90].

Some strain rate dependent failure criterion have already been developed being the common factor between them the necessity of a wide range of experimental data to calibrate the models [91–93].

In this work, the approach followed by Millen et al. [94] will be used to represent the effect of the stain rate on the behaviour of the composite parts.

The proposed method is based on three strain rate values that are usually used in literature: quasi-static, 0.1 s^{-1}, high strain rate, 100 s^{-1} and the intermediate values.

The values of the different properties such as fracture energies and failure loads were retrieved for the lower and higher strain rate values from previously obtained experimental results of the literature including several different sources and a scaling parameter able to capture the global trend of the changes was created [94].

This scaling parameter, is defined as a linear interpolation between the extreme values of the properties. The calculation of the scaling factor, β, is then defined as follows:

$$\beta = \begin{cases} 1.0 \text{ if } \dot{\varepsilon_2} \leq 0.1 \\ \dfrac{(\dot{\varepsilon}_2 - 0.1)(1.29 - 1)}{100 - 0.1} + 1 \text{ if } 0.1 < \dot{\varepsilon_2} < 100 \\ 1.29 \text{ if } \dot{\varepsilon_2} \geq 100 \end{cases} \tag{16}$$

The given example is for the in-plane transversal stiffness (dependent on $\dot{\varepsilon_2}$), which, for instance, will be used for the out-of-plane transversal stiffness, meaning that the final values of the transversal stiffnesses each element will be given by the following expression:

$$E_{2f} = E_{3f} = \beta E_2 \tag{17}$$

Where E_{2f} and E_{3f} are the final values of the stiffness in both transversal directions. For the sake of clarity, the orientation of the strain components are shown on Figure 3.6.

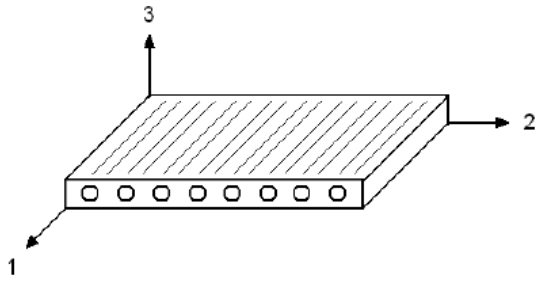

Figure 3.6: Ply material orientation [95].

The scaling factor for the stiffness has a maximum value of 1.29, verified for high strain rates, however, the same does not apply for other properties. In Table 3.2, the values of the scaling factor[3] are shown for each mechanical property.

Table 3.2: Scaling factors.

	G_C^{mc}	G_C^{mt}	X_C	X_T	Y_C	Y_T
Scaling Factor	1.63	1.23	1.39	1.38	1.37	1.38

[3]In this context, scaling factor is used to address its maximum value. To determine the value to multiply by the property, a similar procedure to Eq. 16 substituting its value wherever 1.29 appears needs to be followed.

It is worth noticing that there is no stiffness change in the longitudinal direction since it is considered to be strain rate insensitive [96]. The matrix, being made of polymeric materials, is the one mainly affected by the strain rate, explaining why the stiffness changes are only being made on the transverse directions. The approximation to a linear change of properties between the two strain rate regimes may also be not totally accurate given the viscoelatic behavior of polymers, however, applying these changes may be more desirable than not considering the effect of strain rate at all.

3.1.2 Damage evolution

Once damage is initiated, subsequent loading leads to stiffness degradation, which evolution has been tried to be predicted through different models [97]. In fact, the previously presented failure criteria were thought to predict damage initiation, not considering a damage evolution, however, some damage evolution laws have been proposed by different authors to get closer to the reality.

One of the proposed behaviour, consists in an instantaneous degradation of the material properties once the damage initiation criteria is met, being reduced entirely or to a fraction of their original value, depending on a degradation factor. However, this instantaneous degradation may not be completely adequate, since the sudden total or partial loss of stiffness might not be realistic. Their adequacy depends on the problem being modelled.

More physically based degradation models are the gradual degradation models (GDM). Contrarily to the instantaneous degradation models (IDM), after the failure criteria is met, and given that the specimen/part is still being loaded, a material gradual degradation (also known as softening phase) takes place [98]. This gradual change in stiffness can be modelled in different ways, being the most common the linear and exponential models.

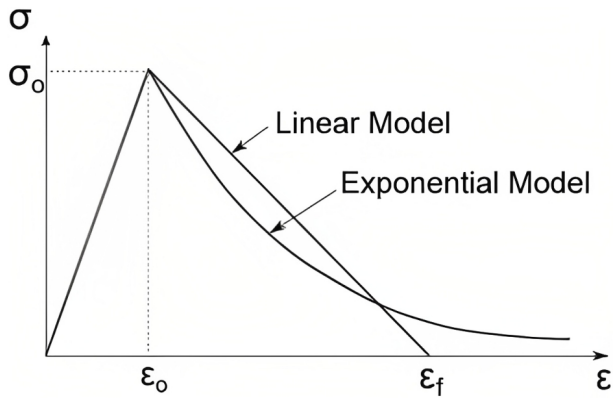

Figure 3.7: Linear and exponential degradation models [97].

As it can be seen from Figure 3.7, there is a linear elastic behaviour until the strain reaches the value of ε_0, which is the equivalent strain value at which the failure criteria is met, followed by a softening phase.

The equivalent strain and stress formulations for each failure mode that will be used in this work can be seen on the table below:

Table 3.3: Equivalent displacement and stress for each failure mode.

Failure modes	Equivalent displacement	Equivalent stress
Fibre Tension	$\delta_{eq}^{ft} = l_c\sqrt{\langle\varepsilon_{11}\rangle^2 + \varepsilon_{12}^2 + \varepsilon_{13}^2}$	$\sigma_{eq}^{ft} = \frac{l_c(\langle\sigma_{11}\rangle\langle\varepsilon_{11}\rangle + \sigma_{12}\varepsilon_{12} + \sigma_{13}\varepsilon_{13})}{\delta_{eq}^{ft}}$
Fibre Compression	$\delta_{eq}^{fc} = l_c\langle-\varepsilon_{11}\rangle$	$\sigma_{eq}^{fc} = \frac{l_c\langle-\sigma_{11}\rangle\langle-\varepsilon_{11}\rangle}{\delta_{eq}^{fc}}$
Matrix Tension	$\delta_{eq}^{mt} = l_c\sqrt{\langle\varepsilon_{22}\rangle^2 + \langle\varepsilon_{33}\rangle^2 + \varepsilon_{12}^2 + \varepsilon_{23}^2 + \varepsilon_{13}^2}$	$\sigma_{eq}^{fc} = \frac{l_c(\langle\sigma_{22}\rangle\langle\varepsilon_{22}\rangle + \langle\sigma_{33}\rangle\langle\varepsilon_{33}\rangle + \sigma_{12}\varepsilon_{12} + \sigma_{23}\varepsilon_{23} + \sigma_{13}\varepsilon_{13})}{\delta_{eq}^{mt}}$
Matrix Compression	$\delta_{eq}^{mt} = l_c\sqrt{\langle-\varepsilon_{22}\rangle^2 + \langle-\varepsilon_{33}\rangle^2 + \varepsilon_{12}^2 + \varepsilon_{23}^2 + \varepsilon_{13}^2}$	$\sigma_{eq}^{fc} = \frac{l_c(\langle-\sigma_{22}\rangle\langle-\varepsilon_{22}\rangle + \langle-\sigma_{33}\rangle\langle-\varepsilon_{33}\rangle + \sigma_{12}\varepsilon_{12} + \sigma_{23}\varepsilon_{23} + \sigma_{13}\varepsilon_{13})}{\delta_{eq}^{mt}}$

The symbol,$\langle\rangle$, represents the Macaulay operator which is defined by the following expression:

$$\langle a\rangle = \frac{a + |a|}{2}, \forall a \in \mathbb{R} \tag{18}$$

It should also be noted that the equivalent displacement is obtained by multiplying the equivalent strain by a characteristic length, l_c, which, in this work, will be considered equal to the cubic root of the total element volume. This characteristic length, allows the reduction of the mesh dependence problems (although not entirely for elements with high aspect ratios) [98].

The final failure displacement value, δ_f, can be either be set to be a multiple of the displacement at failure initiation or it can be obtained through an energy based degradation.

Following the latter, and considering a linear degradation law, the final equivalent displacement value can be calculated from the following equation:

$$\delta_{I,eq}^{f} = \frac{2G_{Ic}}{\sigma_{I,eq}^{0}} \tag{19}$$

where G_{Ic} is a material property and is the fracture energy of the failure mode $I, I = \{ft, fc, mt, mc\}$, thus, representing the area enclosed below the two lines (damaged and undamaged stiffness), as shown on Figure 3.8. The value of the stress at damage initiation can be calculated through Equation 22.

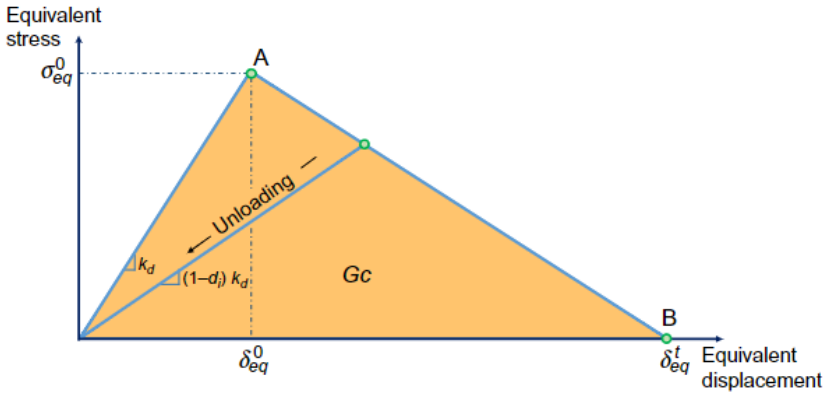

Figure 3.8: Fracture energy represented by the enclosed area [99].

This area should represent the energy dissipated per unit area, thus, being dependent on the element size. In fact, despite the usage of a characteristic length, mesh sensitivity problems may appear due to the enforcement of the dissipated energy, as schematically represented by Figure 3.9 [98].

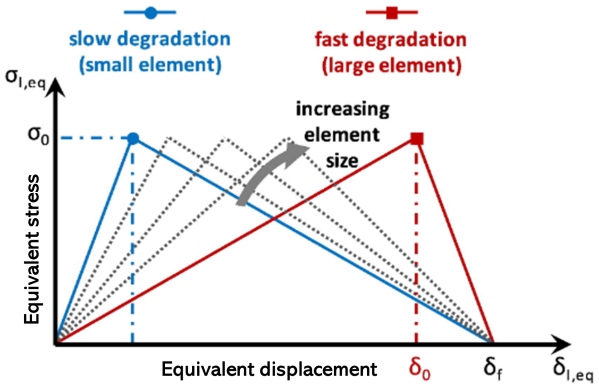

Figure 3.9: Influence of the characteristic length l_c on the constitutive model. Adapted from [98].

Both generation of the mesh and element size selection should be done carefully to ensure that the solution is as mesh independent as possible, specially for energy based damage models [100].

After the damage onset, the damage variable for each failure mode can be calculated through the following expression:

$$d_I = \frac{\delta^f_{I,eq}(\delta_{I,eq} - \delta^0_{I,eq})}{\delta_{I,eq}(\delta^f_{I,eq} - \delta^0_{I,eq})} \qquad (d_I \in [0,1], I = ft, fc, mt, mc) \tag{20}$$

where $\delta^f_{I,eq}$ is the final equivalent displacement defined by Eq.19, $\delta^0_{I,eq}$ is the equivalent displacement for the damage onset, and $\delta_{I,eq}$ is the equivalent displacement at each time increment.

There are different ways of determining both the equivalent displacement and stress at damage initiation. In this work, the following relations will be used:

$$\delta^0_{I,eq} = \frac{\delta_{I,eq}}{\sqrt{F_I}} \tag{21}$$

$$\sigma^0_{I,eq} = \frac{\sigma_{I,eq}}{\sqrt{F_I}} \tag{22}$$

where F_I is the value of the damage initiation criterion.

3.1.3 Damage model

Composite plies are considered as orthotropic materials, meaning that they have different properties for each of the three orthogonal axis. Consequently, the stiffness matrix has the following configuration:

$$[C_d] = \frac{1}{\Lambda}\begin{bmatrix} C_{11} & C_{12} & C_{13} & 0 & 0 & 0 \\ C_{21} & C_{22} & C_{23} & 0 & 0 & 0 \\ C_{31} & C_{32} & C_{33} & 0 & 0 & 0 \\ 0 & 0 & 0 & C_{44} & 0 & 0 \\ 0 & 0 & 0 & 0 & C_{55} & 0 \\ 0 & 0 & 0 & 0 & 0 & C_{66} \end{bmatrix} \tag{23}$$

Note that the subscript d stands for damaged (stiffness matrix), which, in this work, is formulated so that it can be used for both undamaged and damaged steps.

Following a modified Matzenmiller et al.[101] approach employed by Zhou et al. [86], the matrix components are defined as:

$$C_{11} = d_f E_{11}(1 - d_m \nu_{23}\nu_{32}) \tag{24}$$

$$C_{22} = d_m E_{22}(1 - d_f \nu_{13}\nu_{31})$$
$$C_{33} = E_{33}(1 - d_f d_m \nu_{12}\nu_{21})$$
$$C_{12} = d_f d_m E_{11}(\nu_{21} + \nu_{23}\nu_{31})$$
$$C_{13} = d_f E_{11}(\nu_{31} + d_m \nu_{21}\nu_{32})$$
$$C_{23} = d_m E_{22}(\nu_{32} + d_f \nu_{12}\nu_{31})$$
$$C_{44} = \Lambda d_f d_m G_{12}$$
$$C_{55} = \Lambda d_f d_m G_{23}$$
$$C_{66} = \Lambda d_f d_m G_{13}$$

where

$$\begin{cases} d_f = (1 - d_{ft})(1 - d_{fc}) \\ d_m = (1 - S_{mt} d_{mt})(1 - S_{mc} d_{mc}) \\ \Lambda = 1 - d_f d_m \nu_{12}\nu_{21} - d_m \nu_{23}\nu_{32} - d_f \nu_{13}\nu_{31} - 2 d_f d_m \nu_{21}\nu_{32}\nu_{13} \end{cases} \tag{25}$$

where $d_{ft}, d_{fc}, d_{mt}, d_{mc}$ are the damage parameters for fibre and matrix for both tensile and compression loads. In order to control shear stiffness loss due to the failure of the matrix, two parameters S_{mt} and S_{mc} with the values of 0.9 and 0.5 respectively are introduced.

3.2 Inter-Laminar damage

Inter-Laminar damage or delamination, is one of the most common form of composite failure, specially when impact phenomena is involved [22]. Delamination can be considered to have two different stages: initiation and propagation. While the former is usually modelled through maximum stress/strain criteria or quadratic laws, the latter is frequently reduced to an energy based evolution [22]. In this work, a cohesive element approach will be used to simulate the interaction (initiation and propagation of delamination) between the plies.

Under several if not the majority of cases, delamination of composite plies takes place under mixed-mode loadings, which onset cannot be effectively predicted employing the general rule of comparing the tractions to their corespondent allowables, once it can happen before any of the allowables is met by the individual traction components [102].

Taking this into account, Camanho and Dávila [102] developed a quadratic failure based criterion to determine the initiation of delamination under mixed mode loadings. This method, used on this work, is presented below:

$$\left\{\frac{\langle t_n \rangle}{t_n^0}\right\}^2 + \left\{\frac{t_s}{t_s^0}\right\}^2 + \left\{\frac{t_t}{t_t^0}\right\}^2 = 1 \tag{26}$$

where $t_i (i = n, s, t)$ are the traction forces in the normal, n, and shear directions, respectively, and the denominators are the corresponding allowables.

These tractions, are proportional to the difference of nodal displacements by a factor of a penalty stiffness K, which is considered the same for all the modes:

$$t_i = K\delta_i, \ i = n, s, t \tag{27}$$

Following the same behaviour as the intra-laminar damage, after delamination is started, there is an irreversible linear softening of the cohesive element being the corresponding evolution described by the following equation:

$$D = \frac{\delta_m^f(\delta_m^{max} - \delta_m^0)}{\delta_m^{max}(\delta_m^f - \delta_m^0)} \tag{28}$$

where δ_m^0 is the effective displacement at damage initiation, i.e. the value of δ_m^{max} when Equation 26 is verified, and δ_m^f is the effective displacement at complete failure.

The value of the maximum attained displacement during the loading, δ_m^{max}, can be determined by the following expression:

$$\delta_m^{max} = max\left\{\sqrt{\langle\delta_n\rangle^2 + \delta_s^2 + \delta_t^2}\right\} = max\left\{\sqrt{\langle\delta_n\rangle^2 + \delta_{shear}^2}\right\} \tag{29}$$

The effective displacement at complete failure, δ_m^f, needs to be determined using the fracture toughness. Once again, it should be equal to the total area enclosed by the bi-linear evolution:

$$\delta_m^f = \frac{2G_C}{T_m^0} \tag{30}$$

being G_C the fracture energy and T_m^0 the effective traction, given by:

$$T_m^0 = K\delta_m^0 \tag{31}$$

Contrarily to the intra-laminar constitutive formulation, for the inter-laminar damage, bi-linear laws will not be generated for each failure mode exclusively, meaning that there must be a way to account for the change in fracture energy based on the loading modes.

There are different ways to account for this variation, being one of them the power law criterion [103], presented below:

$$\left\{\frac{G^n}{G_C^n}\right\}^2 + \left\{\frac{G^s}{G_C^s}\right\}^2 + \left\{\frac{G^t}{G_C^t}\right\}^2 = 1 \tag{32}$$

where $G_C = G^n + G^s + G^t$ when the expression above is verified.

However, it was observed that it would not draw acceptable results for some mixed-mode loading conditions [102]. Instead, Benzeggagh and Kenane [104] proposed an accurate model (B-K) to determine the mixed-mode fracture energy, which is dependent on Mode I, Mode II and Mode III fracture toughnesses and an experimentally determined parameter, η, which accounts for the mode ratio.

The proposed relation can be written as:

$$G_C = G_C^n + (G_C^s - G_C^n)\left\{\frac{G^S}{G^T}\right\}^\eta \tag{33}$$

where $G^S = G^s + G^t$, is the sum of the critical fracture energies in the first and second shear directions and $G^T = G^n + G^S$ the sum of all the critical fracture energies [102].

As a summary, and for the sake of clarity, a schematic of the overall cohesive element mixed-mode behaviour can be seen on Figure 3.10.

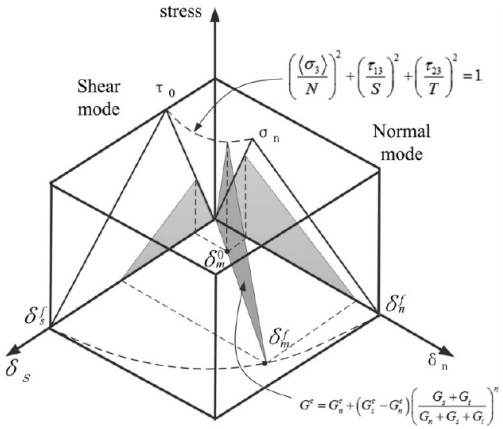

Figure 3.10: Mixed-mode behaviour of a cohesive element [105].

3.3 Numerical Implementation

Having disclosed the methods and criteria that will be used in this work, in this section, the details of how they were implemented in the finite element explicit scheme will be presented. Before further details of the developed models are conveyed, the difference between the explicit and implicit schemes needs to be addressed.

3.3.1 Explicit and Implicit Schemes

Structural dynamic problems such as crash tests and low velocity impact of composite plates are all defined by the following equation:

$$M\ddot{u} + C\dot{u} + Ku = f \tag{34}$$

where M, C and K are the mass, damping, and stiffness matrices, f is the vector of nodal forces (both body and external) and $\ddot{u}$, $\dot{u}$, and u are the acceleration, velocity and displacement nodal vectors, respectively.

As it can be seen, it is a second order differential equation (with respect to the time t) and thus, needs to be integrated to obtain the solution. It is on the way this expression is integrated that lies the difference between the explicit and implicit schemes.

The explicit method is based on the central differences method [106], and, therefore, the values of the velocity and acceleration are given by the following expressions:

$$\dot{u}^t = \frac{1}{2\Delta t}(u^{t+\Delta t} - u^{t-\Delta t}) \tag{35}$$

$$\ddot{u}^t = \frac{1}{(\Delta t)^2}(u^{t+\Delta t} - 2u^t + u^{t-\Delta t}) \tag{36}$$

Where Δt is a small time interval of the total simulation time, t. Substituting these new expressions, on the dynamic equation, it is easily shown that the value of the displacement, u, at the instant $t + \Delta t$ can be obtained knowing the values of both $u^{t-\Delta t}$ and u^t and the respective force at that instant f^t.

If the mass and damping matrices are diagonal, also known as 'lumped', the problem does not require the solution of a linear system of equations,thus, making this method computationally cheap [106]. However, it is conditionally stable, meaning that the time increment, Δt, should be sufficiently small to ensure numerical stability. A critical value based on the smallest natural period is commonly used:

$$\Delta t < \Delta t_{cr} = \frac{2}{\omega_n} \tag{37}$$

On the other hand, the implicit method is based on a linear acceleration approximation [106], where the velocity and displacement vector at an instant $t + \Delta t$ are given by:

$$\dot{u}^{t+\Delta t} = \dot{u}^t + \Delta t(\gamma \ddot{u}^{t+\Delta t} + (1-\gamma)\ddot{u}^t) \tag{38}$$

$$u^{t+\Delta^t} = u^t + \Delta t \dot{u}^t + (\Delta t)^2(\beta \ddot{u}^{t+\Delta t} + \left(\frac{1}{2} - \beta\right)\ddot{u}^t) \tag{39}$$

where the parameters β and γ are determined to ensure stability. Common values for these parameters are the ones following Newmark's method, where $\beta = \frac{1}{4}$ and $\gamma = \frac{1}{2}$ [106]. Substituting these expressions on the problem equation, it is found that the response at $t + \Delta t$ can only be obtained by solving a linear system of equations based on the force equilibrium at $t + \Delta t$. These calculations make this method computationally more expensive than the explicit, however, it is unconditionally stable, meaning that the time increment can be larger than the one required for the explicit.

Given this, the implicit method is preferred whenever 'slow' events need to be simulated, because the time increment can be set to any value. The explicit scheme, having a small imposed time increment, is optimal for fast events, generally under a second, being also computationally cheaper. The explicit scheme also simplifies contact interactions and uses a large deformation theory, good for when large deformations or rotations are involved. The accuracy of each step is also not calculated by ABAQUS as it is done for the implicit scheme, which, for instance, may overcome to convergence problems [106]. Besides, both methods can be used for slow quasi-static analysis, some of which have been done in this work.

Therefore, in this work, since crash analysis are being considered, the explicit scheme will be used.

3.3.2 Element Formulation

Despite the fact that ABAQUS commercial software already has the Hashin failure criterion with linear degradation [106], it is only possible to use it on elements with plane stress formulation (e.g., shell, continuum shell, membrane, etc.).

However, the common feature between these type of elements is that the stress in the thickness direction, which is necessary to employ the presented failure criteria, is considered to be zero ($\sigma_{33} = 0$) and the respective Poisson effects are not included. Therefore, for the implementation of the 3D Hashin or other 3D methods, it is necessary to create our own material behavior, using a set of constitutive equations.

3.3.3 VUMAT development

To do this, ABAQUS allows the implementation of user defined materials, which, for the ABAQUS/Explicit package, is also known as VUMAT [106]. In this work, a VUMAT was implemented for three dimensional brick solid elements (Figure 3.11).

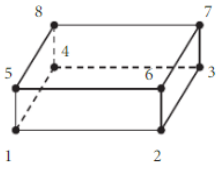

Figure 3.11: Example of a 3D element (C3D8, 8-node linear brick) [107].

This subroutine, programmed in FORTRAN, includes, for each iteration (time step) and for each integration point: the strain calculation and the corresponding stress components, which allow the assessment of damage onset and, consequently, the damaged stiffness matrix update and other variables such as solution-dependent state or field ones.

As observed in Figure 3.12, after defining the material constants and the number of necessary solution dependent state variables, a small strain increment (considering a purely elastic step) is given to initialize the analysis. Then, for all the next time increments, the strain is updated based on the nodal displacements followed by the calculation of the correspondent stresses. After the new stress state is determined, the failure criterion is calculated to verify if damage has started.

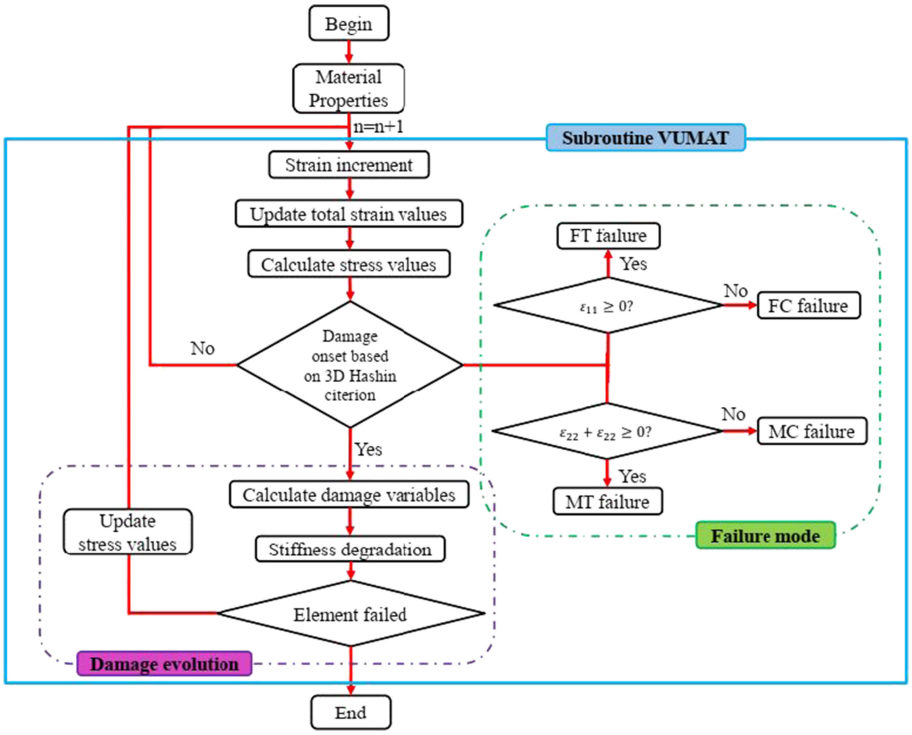

Figure 3.12: Flowchart of 3D Hashin VUMAT [84].

If damage has not occurred, the new stress tensor is kept, the internal energy is calculated and the process continues for the next time step, however, if damage has started, a new stiffness matrix is computed (damaged stiffness matrix) and based on the same strain, new stresses are calculated and updated. It is worth noticing that this routine is followed for every element and time increment, being each strain increment automatically given by the ABAQUS solver.

The developed VUMAT was based on a preexisting 3D Hashin with instantaneous degradation developed by H.N.R. Wagner [108]. Given that, in this work, gradual degradation is implemented.

To account for the stiffness change that may occur in each time increment, after damage has initiated, state variables capable of storing the damage variable needed to be added to the code.

The developed routine requires 16 independent material properties shown in Table 3.4 and 28 solution dependent state variables (30 for the strain rate dependent VUMAT) disclosed in Table 3.5.

These variables are automatically operated by the ABAQUS software, which, for each time increment, copies their values from a stateNew array to a stateOld one. The original code state variables that were kept were: the damage control variables (4 state variables, one for each mode) and the stress and strain tensors (6+6 state variables in total).

In order to employ the gradual degradation, eight additional solution state dependent variables were added to store the initial and final displacement values for each failure mode, which values are given by Equations 21 and 19, respectively. Their values cannot be defined beforehand since they are only determined once damage onset takes place. Other four auxiliary state variables were created to work as 'triggers' for each type of damage, i.e. binary based variables which values change to 1 once the correspondent damage onset has been reached.

For the case of the strain rate dependent criterion, two extra state variables were added to store the values of the stiffness scaling parameter for both transverse directions. The strain rate in each time step is estimated by the following expression:

$$\dot{\varepsilon} = \frac{\varepsilon^{t} - \varepsilon^{t-\Delta t}}{\Delta t} \tag{40}$$

where Δt is the stable time increment and the numerator is the difference in strain between two time increments. Naturally, deep structural changes needed to be made to the original VUMAT to accommodate this new gradual degradation routine, ranging from creating mechanisms to appropriately update the state variables to the implementation of the gradual degradation equations and functions.

Table 3.4: VUMAT required material constants.

Elastic Properties	
props(1)	E_1 (Longitudinal Young's Modulus)
props(2)	E_2=E_3 (Transverse Young's Modulus)
props(3)	$\nu_{12} = \nu_{13}$ (Poisson's ratio)
props(4)	ν_{23} (Poisson's ratio)
props(5)	G_{12}=G_{13} (Shear Modulus)
props(6)	G_{23} (Out-of-plane Shear Modulus)
Damage Initiation Properties	
props(7)	X_T (Longitudinal Tensile Strength)
props(8)	X_C (Longitudinal Compressive Strength)
props(9)	Y_T (Transverse Tensile Strength)
props(10)	Y_C (Transverse Compressive Strength)
props(11)	S_{12}=S_{13} (Shear Strength)
props(12)	S_{23} (Out-of-plane Shear Strength)
Intra-laminar Fracture Toughness	
props(13)	G_C^{ft} (Longitudinal Tension Fracture Toughness)
props(14)	G_C^{fc} (Longitudinal Compression Fracture Toughness)
props(15)	G_C^{mt} (Transverse Tension Fracture Toughness)
props(16)	G_C^{mc} (Transverse Compression Fracture Toughness)

Some other new features needed to be implemented into the code so that the material would behave closer to the reality. For instance, for each time increment, the damage variable is controlled so that there no is way of decreasing its value nor reaching above the 1 or negative values, done by enforcing the following relations:

$$d_I = min\{d_I, 1\} \tag{41}$$

$$d_I = max\{d_I, 0\} \tag{42}$$

$$d_I = max\{d_I, d_I^{old}\} \tag{43}$$

The last relation, where d_I^{old} is the damage variable value obtained at the previous time step, is to ensure that the there is no decrease in the damage variable from one time step to another, preventing the material from 'healing' if the stress state changed in a way that would allow it.

Table 3.5: State variables.

stateNew(1)	i_svd _dmgfT : tensile fibre damage
stateNew(2)	i_svd _dmgfC : compressive fibre damage
stateNew(3)	i_svd _dmgmT : tensile matrix damage
stateNew(4)	i_svd _dmgmC : compressive matrix damage
stateNew(5-10)	i _svd _Stressij: stress in ij direction, $i, j = x, y, z$
stateNew(11-16)	i _svd _Strainij: strain in ij direction, $i, j = x, y, z$
stateNew(17)	i _svd _deq0t: equivalent displacement at fibre tensile damage onset
stateNew(18)	i _svd _dfeqt: equivalent displacement at fibre tensile total failure
stateNew(19)	i _svd _deq0c: equivalent displacement at fibre compressive damage onset
stateNew(20)	i _svd _dfeqc: equivalent displacement at fibre compressive total failure
stateNew(21)	i _svd _deq0mt: equivalent displacement at matrix tensile damage onset
stateNew(22)	i _svd _dfeqmt: equivalent displacement at matrix tensile total failure
stateNew(23)	i _svd _deq0mc: equivalent displacement at matrix compressive damage onset
stateNew(24)	i _svd _dfeqmc: equivalent displacement at matrix compressive total failure
stateNew(25)	i _svd _fttrigger: fibre tensile damage onset trigger
stateNew(26)	i _svd _fctrigger: fibre compressive damage onset trigger
stateNew(27)	i _svd _tttrigger: matrix tensile damage onset trigger
stateNew(28)	i _svd _tctrigger: matrix compressive damage onset trigger
Only for the SRD criterion	
stateNew(29)	i _svd _beta2: strain rate on the Yy direction
stateNew(30)	i _svd _beta3: strain rate on the Zz direction

4 Composite Failure Model Numerical Development and Validation

In this chapter, the procedures followed to evaluate the performance of the developed models will be explained and presented.

4.1 One element test

Initially, a simple 1 mm sided cubic element test, representing a unidirectional ply, is conducted to verify not only the elastic behavior but also the damage onset and evolution.

To accomplish this, the element was loaded in two of its principal directions, both longitudinal and transverse. For each direction, one of the normal faces is constrained on the load direction and the corresponding opposite face is imposed a finite displacement, δ, as observed on Figure 4.1.

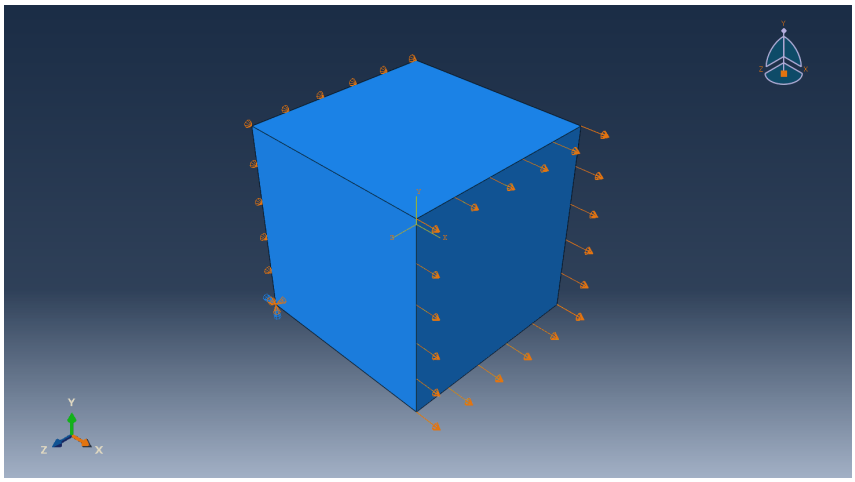

Figure 4.1: One millimeter side cubic element loaded in the longitudinal direction.

The imposed displacement was of 10 mm over a 1 s time period to ensure total failure for each mode. Additionally, a node of the constrained face is clamped to ensure that no movement occurs in other translational directions.

The element type is a C3D8R meaning it is a three dimensional, 8-node linear brick element with reduced integration (one integration point in the centre). The total number of outputs was set to 100 (every 0.01 s) and due to the simplicity of the model, no mass scaling was employed.

The material properties used to verify the VUMAT are the ones used in [98] and can be found on Table 4.1.

Table 4.1: Material properties for numerical verification [98].

Property	**Value**
E_1 (Longitudinal Young's Modulus)	127.6 GPa
E_2=E_3 (Transverse Young's Modulus)	10.3 GPa
$\nu_{12} = \nu_{13} = \nu_{23}$ (Poisson's ratio)	0.32
G_{12} (In-plane Shear Modulus)	6.0 GPa
G_{13} (Out-of-plane Shear Modulus)	6.0 GPa
G_{23} (Out-of-plane Shear Modulus)	3.0 GPa
X_T (Longitudinal Tensile Strength)	2023.0 MPa
X_C (Longitudinal Compressive Strength)	1234.0 MPa
Y_T (Transverse Tensile Strength)	92.7 MPa
Y_C (Transverse Compressive Strength)	176.0 MPa
S_{12} (In-plane Shear Strength)	82.6 MPa
S_{13} (Out-of-plane Shear Strength)	82.6 MPa
S_{23} (Out-of-plane Shear Strength)	100.0 MPa

Since the damage evolution is dependent on the value of the intra-laminar volumetric fracture energy, these are obtained from the same source and can be consulted on Table 4.2

Table 4.2: Intra-laminar volumetric fracture energy for numerical verification [98].

Volumetric fracture energy	**Value**
G_C^{ft}	128.0 kJ/m^3
G_C^{fc}	128.0 kJ/m^3
G_C^{mt}	5.6 kJ/m^3
G_C^{mc}	9.31 kJ/m^3

Once the material properties are defined, they need to be appropriately inserted in the Finite Element Analysis software. To do this, it is necessary to input them in the "User Material" option while creating a new material, making sure that the order and units of the properties are in accordance with the developed VUMAT.

After defining the boundary conditions, loading, mesh and material properties, the analysis of the behavior for each loading case can be performed.

4.1.1 Hashin Failure Criterion

In this section, the results for the 3D Hashin VUMAT verification are presented. In Figure 4.2, the bi-linear curve obtained for longitudinal tension can be observed

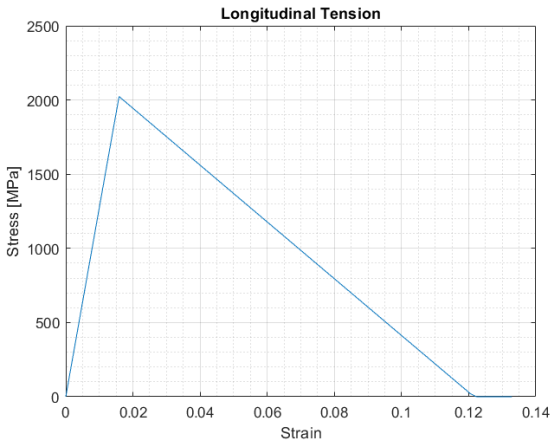

Figure 4.2: Longitudinal Tension VUMAT verification.

The same procedure was followed for compression and for the transverse direction. The resultant bi-linear curves can be found on Figure 4.3.

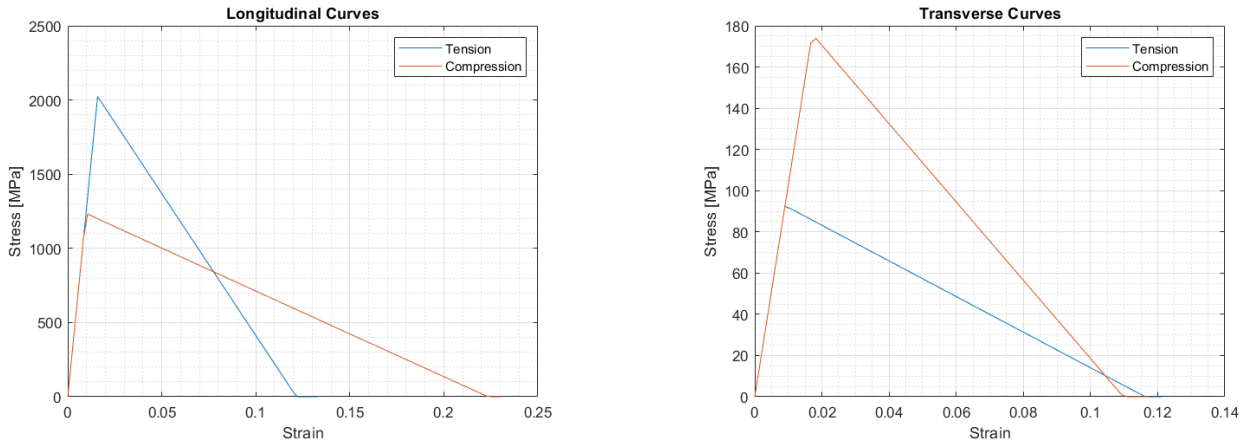

(a) (b)

Figure 4.3: Tension and Compression bi-linear curves for (a) longitudinal and (b) transverse directions.

As observed in the figures, all of the loading modes followed a bi-linear behaviour, being the positive slope relative to the elastic part and the negative slope part relative to the damage evolution. The trapezoidal shape found on the transverse compression curve is due to the number of outputs of the simulation, which skipped the load peak part.

In order to further verify the correct definition of the VUMAT, the obtained failure stresses and volumetric fracture energies are compared with the expected values, given by the material properties. The results are shown on Table 4.3.

Table 4.3: Expected and obtained values of relevant properties for the 3D Hashin element verification.

Failure mode	**Property**	**Expected**	**Obtained**
Fibre Tension	X_T [MPa]	2023.0	$2023.2(0.01\%)$
	G_C^{ft} [kJ/m^3]	128	$123.4(3.6\%)$
Fibre Compression	X_C [MPa]	1234.0	$1235(0.08\%)$
	G_C^{fc} [kJ/m^3]	128	$138.9(8.5\%)$
Matrix Tension	Y_T [MPa]	92.7	$92.3(0.4\%)$
	G_C^{mt} [kJ/m^3]	5.6	$5.4(3.6\%)$
Matrix Compression	Y_C [MPa]	176.0	$174(1.1\%)$
	G_C^{mc} [kJ/m^3]	9.31	$9.57(2.8\%)$

From Table 4.3, it is possible to assume that the VUMAT is functioning as intended, at least for a simple stress state.

The obtained value for the fibre compression volumetric fracture energy is slightly higher than desirable for a 'patch test' and it is also true that relative errors are also dependent on the field output frequency, meaning that with a higher frequency of variables output, these errors would possibly be even lower. However, since all the estimated errors are below the 10% threshold of acceptance, it is safe to assume the VUMAT is well defined.

4.1.2 Puck Failure Criterion

The numerical verification of the Puck failure criteria deemed nearly identical results, since in this work, as previously mentioned, a Hashin + Puck formulation is being used. Therefore, differences are only expected at the matrix compression level.

The matrix compression unidirectional test result is shown on Figure 4.4 and the corresponding relative errors to the expected values on Table 4.4.

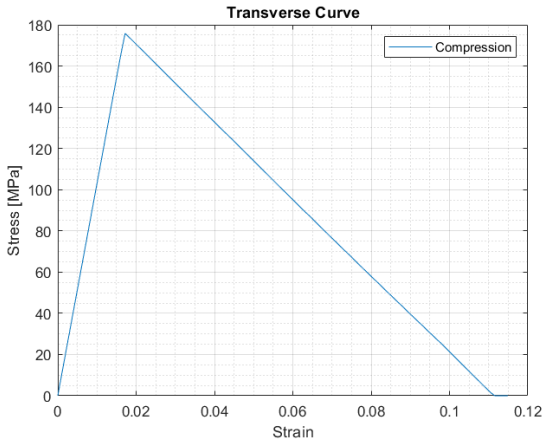

Figure 4.4: Compression bi-linear curves for the tranverse direction using Puck criterion.

Table 4.4: Expected and obtained values of relevant properties for the Puck element verification.

Failure mode	**Property**	**Expected**	**Obtained**
Matrix Compression	Y_C [MPa]	176.0	$175.9(0.06\%)$
	G_C^{mc} [kJ/m^3]	9.31	$9.67(3.9\%)$

As expected, the value of the failure transverse compressive stress is very similar if not practically equal to those previously obtained for the Hashin failure criterion.

In fact, both methods are expected to give equal results for uniaxial transverse compression [109].

4.1.3 Strain Rate Dependent Failure Criterion

In order to verify the strain rate dependency of the material model, at least three different regimes need to be tested: quasi-static, high strain rate and the intermediate region. Therefore, the selected values for the strain rate were 0.1 s^{-1}, 100 s^{-1} and 10 s^{-1} respectively.

In Figure 4.5, the obtained stress-strain curves for each failure mode and strain regime are presented:

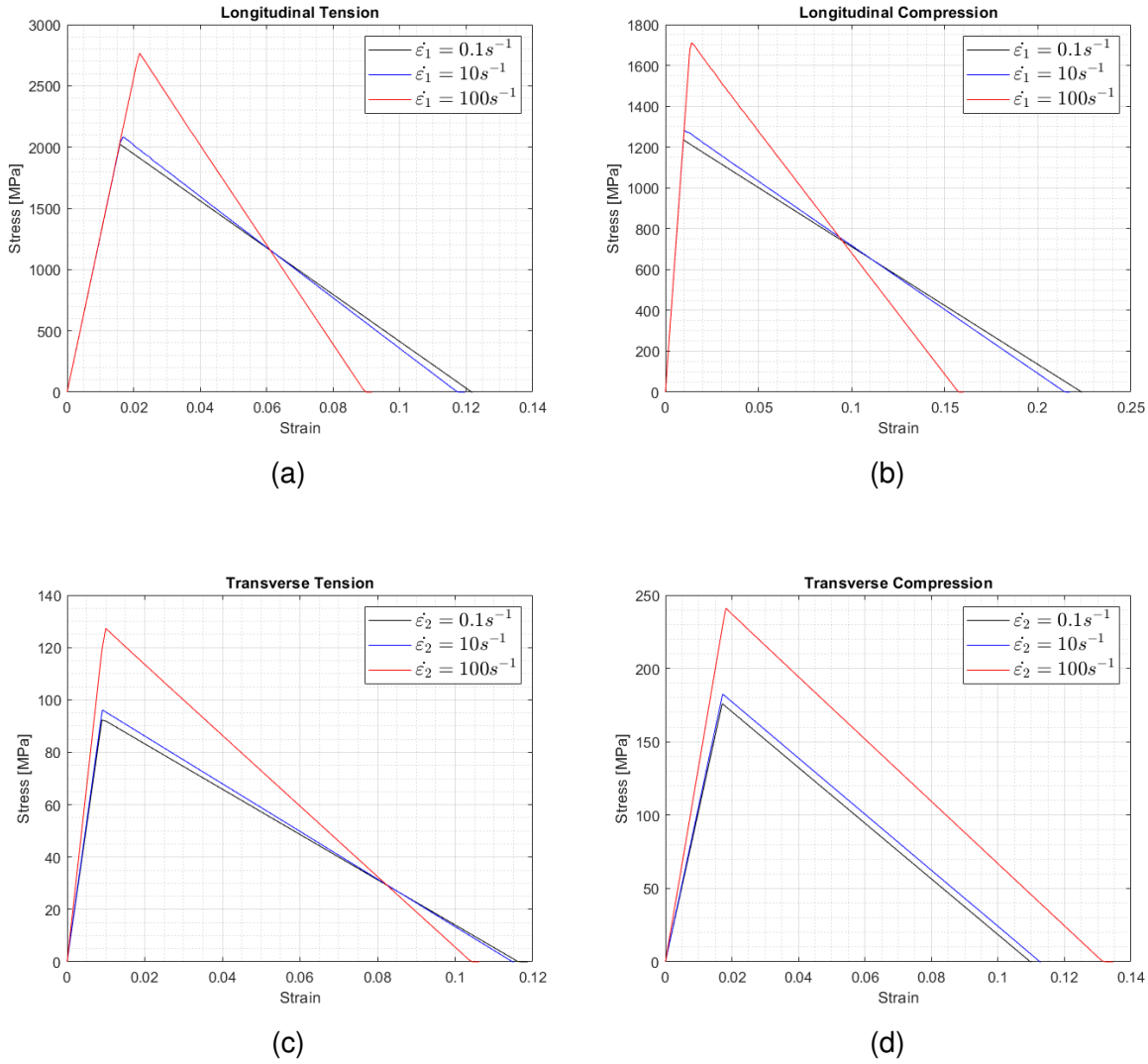

Figure 4.5: Strain rate dependent stress-strain curves for (a) longitudinal tension, (b) longitudinal compression, (c) transverse tension and (d) transverse compression.

From the displayed strain rate dependent stress-strain relations, there are some points that should be highlighted. While the stiffness does not change with the strain rate for the longitudinal cases, the same is not verified for the transverse ones, as expected.

Furthermore, the failure strain decreases with increasing strain rate for the longitudinal loading scenarios, explained by the necessity of keeping the same fracture energy (area) with increasing damage onset load, while for the transverse loading, the failure strain may increase, since the fracture energy is increased the higher the strain rate.

To assess the performance of the developed VUMAT for this specific strain rate dependent criterion, a set of tables (Tables 4.5-4.8) containing the expected, obtained by employing Equation 16 on the model material constants, numerical and relative error values for each strain rate regime (Quasi-Static, QS, Medium Strain Rate, MSR, and High Strain Rate, HSR) are presented for each failure mode.

Table 4.5: Longitudinal tension properties.

Regime	E [MPa]		X_T [Mpa]		G_C [kJ/m^3]	
	Expected	Obtained	Expected	Obtained	Expected	Obtained
QS	127600	127601(0.0%)	2023	2023(0.0%)	128	123(3.9%)
MSR	127600	127724(0.1%)	2099	2083(0.8%)	128	122(4.7%)
HSR	127600	128367(0.6%)	2792	2766(0.9%)	128	125(2.3%)

Table 4.6: Longitudinal compression properties.

Regime	E [MPa]		X_T [Mpa]		G_C [kJ/m^3]	
	Expected	Obtained	Expected	Obtained	Expected	Obtained
QS	127600	127590(0.0%)	1234	1235(0.1%)	128	138(7.8%)
MSR	127600	127710(0.1%)	1282	1282(0.0%)	128	138(7.8%)
HSR	127600	127970(0.3%)	1715	1712(0.2%)	128	134(4.7%)

Table 4.7: Transverse tension properties.

Regime	E [MPa]		X_T [Mpa]		G_C [kJ/m^3]	
	Expected	Obtained	Expected	Obtained	Expected	Obtained
QS	10300	10301(0.0%)	92.7	92.3(0.4%)	5.6	5.4(3.6%)
MSR	10596	10595(0.0%)	96.2	96.1(0.1%)	5.73	5.52(3.7%)
HSR	13287	13285(0.0%)	127.9	127.3(0.5%)	6.88	6.62(3.8%)

Table 4.8: Transverse compression properties.

Regime	E [MPa]		X_T [Mpa]		G_C [kJ/m^3]	
	Expected	Obtained	Expected	Obtained	Expected	Obtained
QS	10300	10300(0%)	176.0	175.9(0.1%)	9.31	9.96(7.0%)
MSR	10596	10604(0.1%)	182.5	182.5(0.0%)	9.89	10.27(3.8%)
HSR	13287	13317(0.2%)	241.1	241.0(0.0%)	15.18	15.8(4.1%)

Analysing the tables, it is possible to verify that the obtained values fall under the 5% error relatively to the expected values, being the exception on the fracture energies which, for instance, do not go over the 8% error threshold. Given these results, it can be securely considered that the VUMAT routine is defined accordingly to the theoretical background that supports it.

5 Model Development and Validation

5.1 Open Hole Tensile Test

Having verified the VUMAT for a simple, uni-axial test case, it would be beneficial to employ the routine in a more complex engineering problem to assess the performance for more complex stress states.

Open-hole tensile (OHT) tests are one of the essential steps for the certification of composite parts which will have to be joined via mechanical solutions (i.e. bolts, rivets, etc.) [110].Therefore, an OHT model was defined to assess and compare the obtained results with previous investigated numerical models and experimental data.

5.1.1 Model description

The geometric details of the simulated specimen can be found on Figure 5.1.

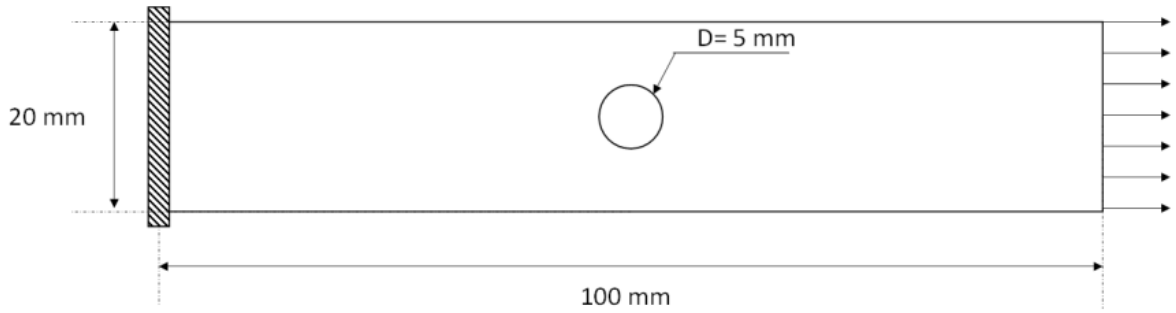

Figure 5.1: Geometric details and boundary conditions of the problem [27].

Figure 5.1 also shows the model boundary conditions, where one of the sample short faces is fixed and the other is subject to a uniform displacement type loading.

The specimen has a total of 16 plies with a thickness of 0.125 mm each and the stacking sequence is $[0,45,90,-45]_{2S}$.

The size of the mesh was set to 2 mm being refined to approximately 1 mm in the rectangular partition around the hole based on the satisfactory results obtained by Riccio et al. [27]. Regarding the thickness one element per ply was employed.

The meshed part is shown on Figure 5.2.

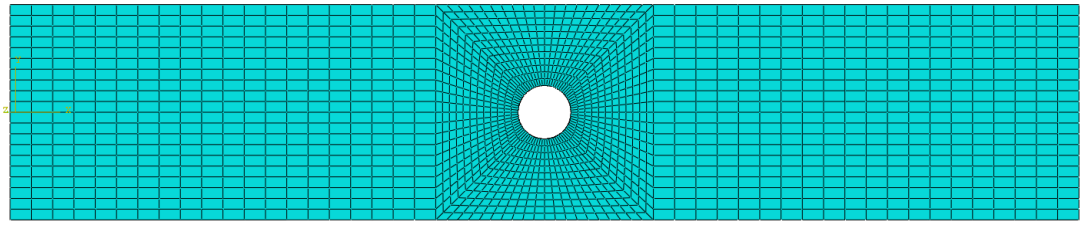

(a)

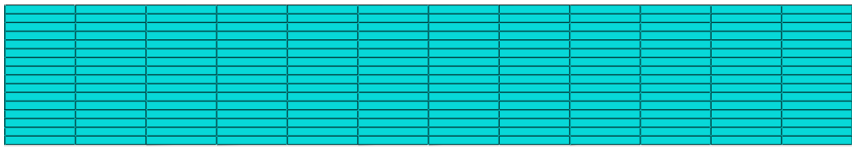

(b)

Figure 5.2: Meshed OHT part: (a) top view and (b) partial lateral view.

The model has a total of 28160 C3D8R elements with 31960 nodes, meaning 95880 degrees of freedom (DOF). The smallest element is the closest to the open hole and has top face area of 0.146 mm^2 and a thickness of 0.125 mm. The material is the same used on the previous section for the one element verification (Tables 4.1 and 4.2).

The applied displacement was of 1 mm over a 3 second period to simulate a quasi-static tensile test, being the strain rate approximately of 0.003 s^{-1}.

To decrease the necessary computational time, a mass scaling technique was employed, i.e., the density of the material was artificially increased by four orders of magnitude to increase wave speed of the material c_d given by:

$$c_d = \sqrt{\frac{E}{\rho}} \tag{44}$$

and since the stable time increment is defined as follows:

$$\Delta t = \frac{l_c}{c_d} \tag{45}$$

this increase in the density will lead to a simulation one hundred times faster. Since no dynamic effects are being considered for this specific analysis, this method can be employed and is a good way of keeping computational times low.

To obtain the load displacement curve, two node sets were created, one containing all of the clamped nodes, which sum of the reaction forces in the load direction will give the total load, and another with 1 element in the face to be displaced (Figure 5.3), to keep track of the displacement.

Figure 5.3: Boundary conditions and highlighted displacement track node (top right).

5.1.2 Results

The obtained load-displacement curve employing the 3D Hashin failure criteria with degradation is shown on Figure 5.4.

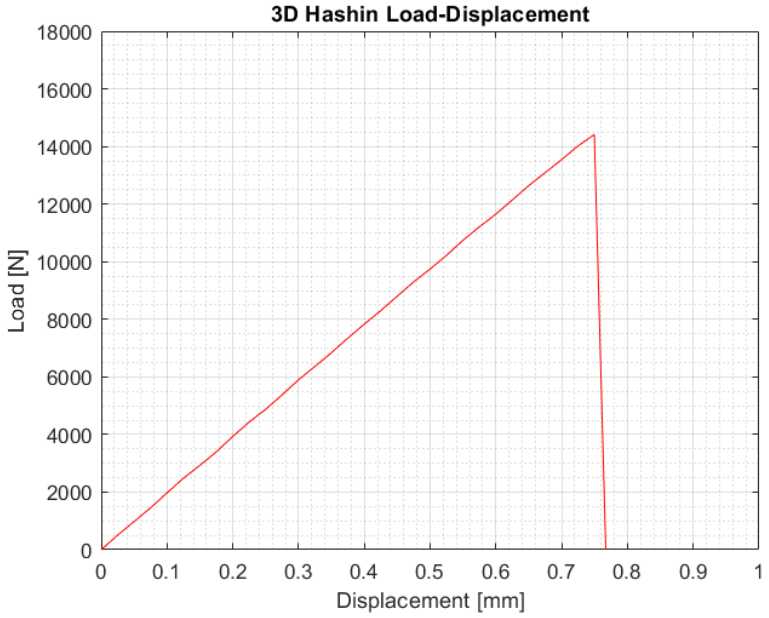

Figure 5.4: Load-displacement curve using Hashin failure criterion.

The simulation took a total of 2348 seconds to finish. For the sake of completion, the same analysis was done for instantaneous degradation, meaning that after the damage onset, the damage variable, d, is automatically converted to $d = 1$.

On the same graph, the value of the experimental result mentioned in [27] is added to assess which of the simulation methods deems better results. The results are found on Figure 5.5.

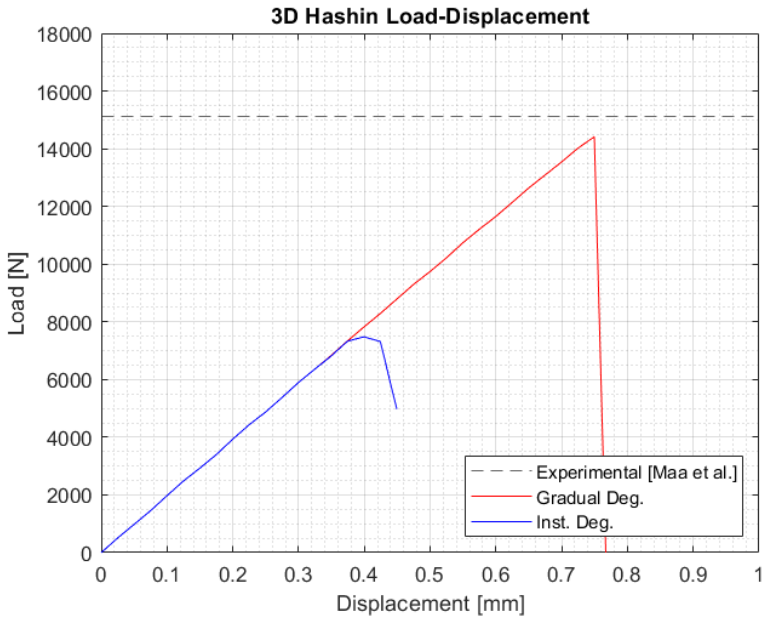

Figure 5.5: Load-displacement curve using Hashin failure criterion with instantaneous and gradual degradation.

As it can be seen from Figure 5.5, the model with instantaneous degradation is not suitable for this analysis leading to an under-prediction of the experimental failure load by approximately 50%, while its gradual counterpart led to a relative error of 4.5%.

Therefore, henceforth, gradual damage evolution will be employed in all the following simulations.

To better visualise the damage distribution, a path trough the thickness was created in one of the critical spots (Figure 5.6), and the damage variables were extracted right before total failure, being the results displayed on Figure 5.7.

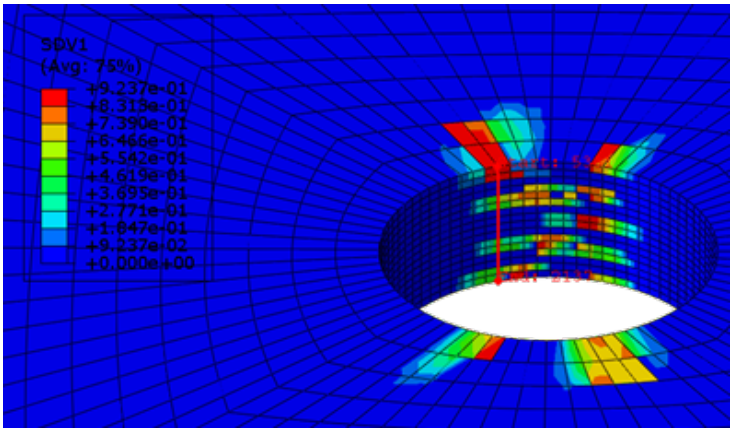

Figure 5.6: Selected path for the assessment of damage through the thickness.

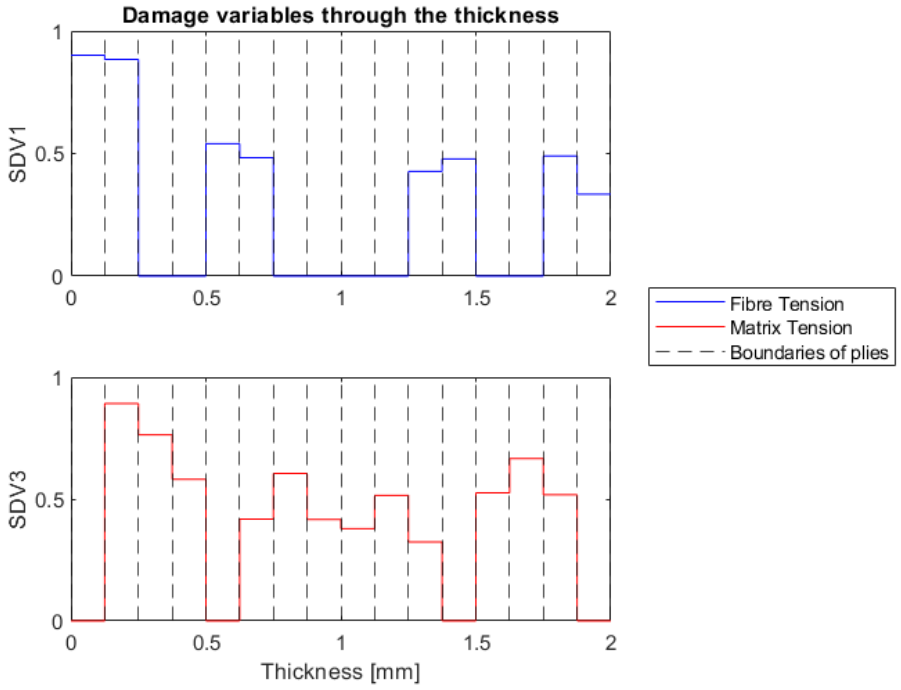

Figure 5.7: Distribution of the non-zero damage variables employing Hashin criterion.

From the graph, it is observed that are the both tensile failure modes that drive the total failure of the laminate. The fibre tensile damage is only verified on both 0° and 45° plies while the matrix tensile damage dominates on the remaining ones.

The same procedure was followed employing the Puck failure criterion for matrix compression. The obtained load-displacement is found on Figure 5.8.

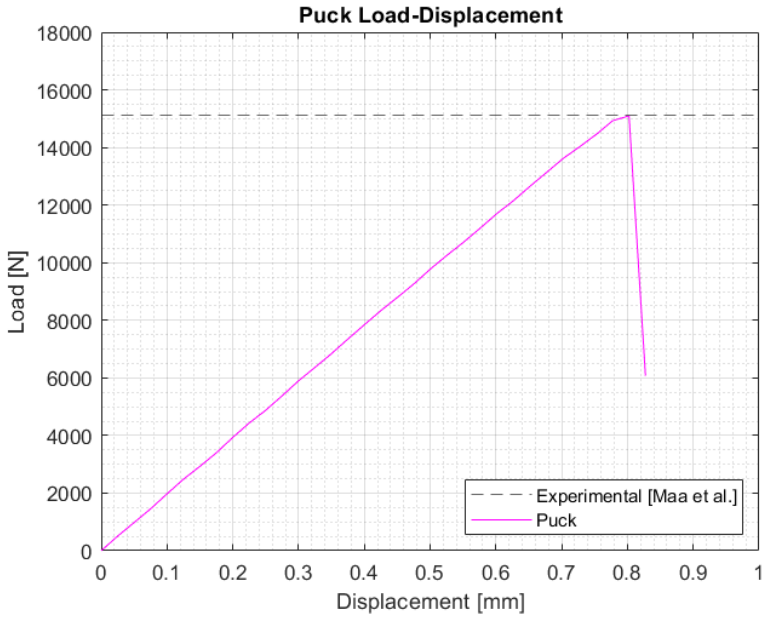

Figure 5.8: Load-displacement curve using Puck failure criterion.

From the graph, it is possible to observe the maximum withstood load is closer using the Puck formulation than Hashin's, in fact, the predicted and the experimental failure load differ by 1 N, meaning there is an excellent agreement between them. The damage distribution through the thickness (in the same previous path) is also shown on Figure 5.9.

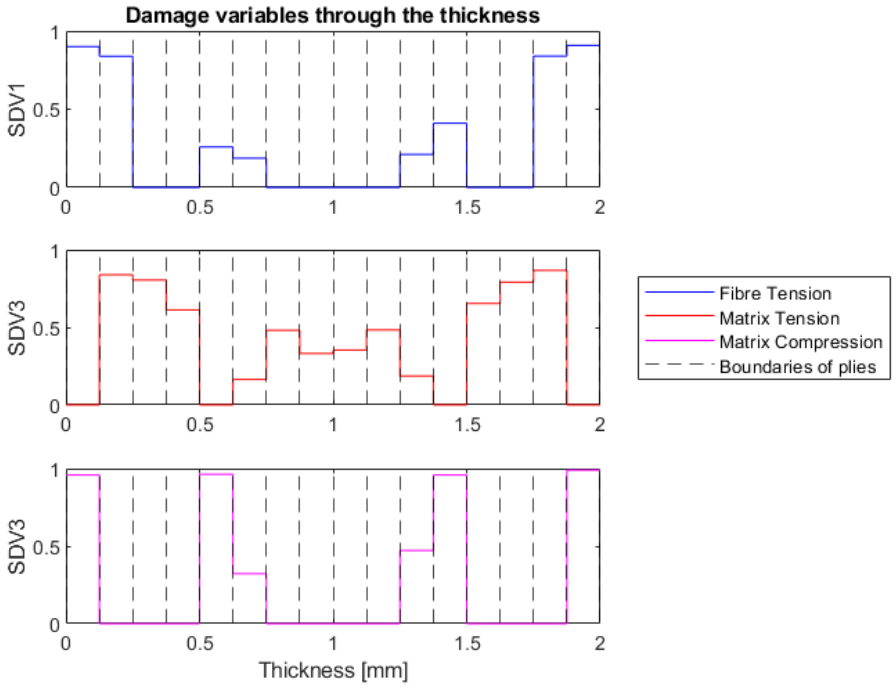

Figure 5.9: Distribution of the non-zero damage variables employing Puck criterion.

Contrarily to the previous results, employing this formulation, some matrix compressive damage is also found on the same plies where fibre tensile damage is verified.

On Table 6.7, the summary of the maximum loads an their relative error to the experimental results can be found.

Table 5.1: Obtained maximum loads.

Criterion	Maximum load	Rel. Error
Experimental	15.100 kN	[-]
Hashin (Inst. deg.)	7.480 kN	50.4%
Hashin (Grad. deg.)	14.413 kN	4.55%
Puck (Grad. deg.)	15.099 kN	0.00%

In Figures 5.10 and 5.11, the damaged area after failure for three different plies is shown, for distinct failure modes and failure criterion. On the same figure are the numerical results obtained by Riccio et al. [27] as a mean of comparison.

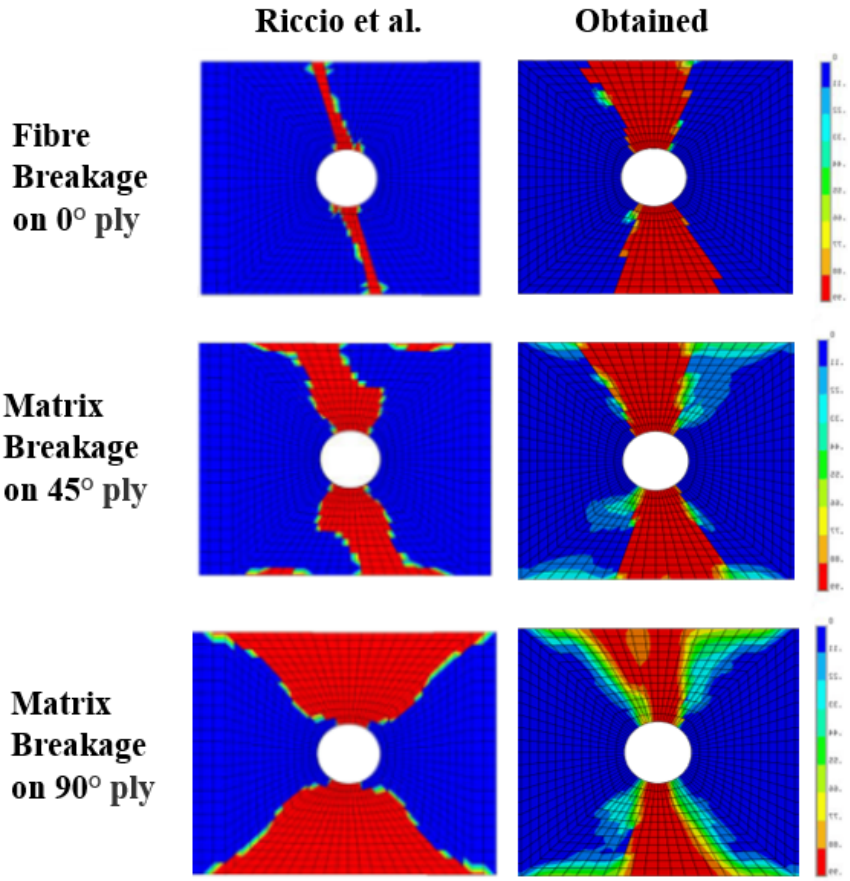

Figure 5.10: Damage distribution comparison for each ply orientation following Hashin criterion. Adapted from [27].

As observed in the figures, the size an shape of the damaged zones are generally close to those previously obtained. However, there are some relevant differences that should be addressed such as the under-prediction of the matrix damage or the size of the fibre tensile failure.

In fact, relatively to the literature, there is an under-prediction of the matrix damage on all of the examples but the 45° ply employing Hashin criterion. However, comparing to other results from the literature for the same specimen, such as the one by Chen et al. [111], as illustrated in Figure 5.12, it can be seen that the obtained shapes are very similar, presenting a smaller and more gradual damaged zone.

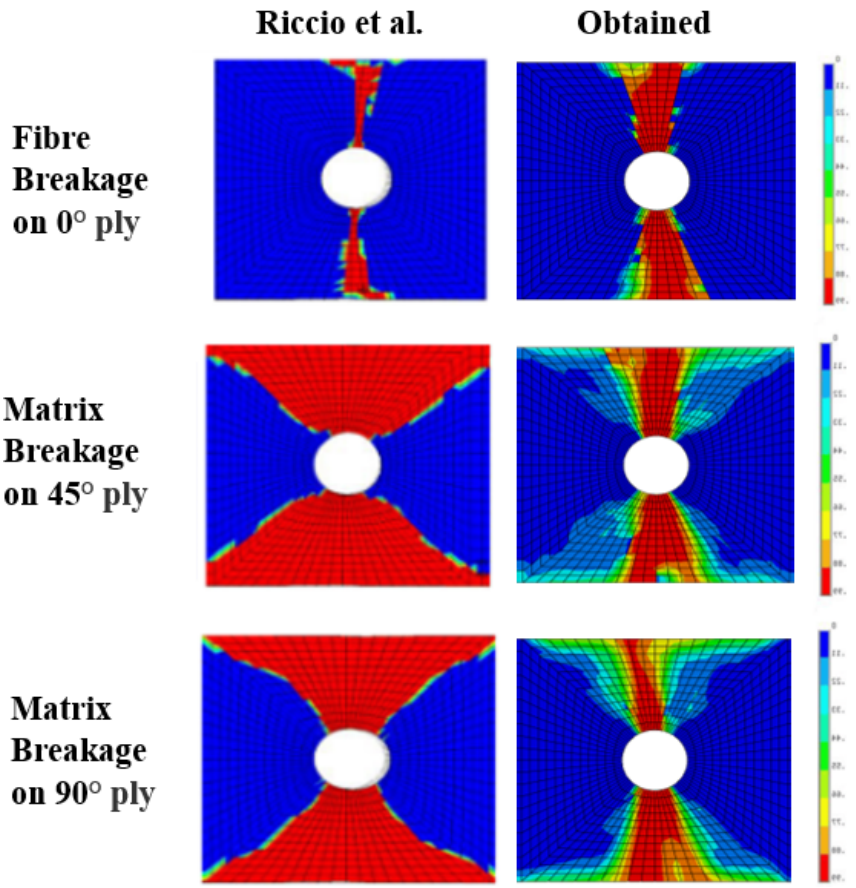

Figure 5.11: Damage distribution comparison for each ply orientation following Puck criterion. Adapted from [27].

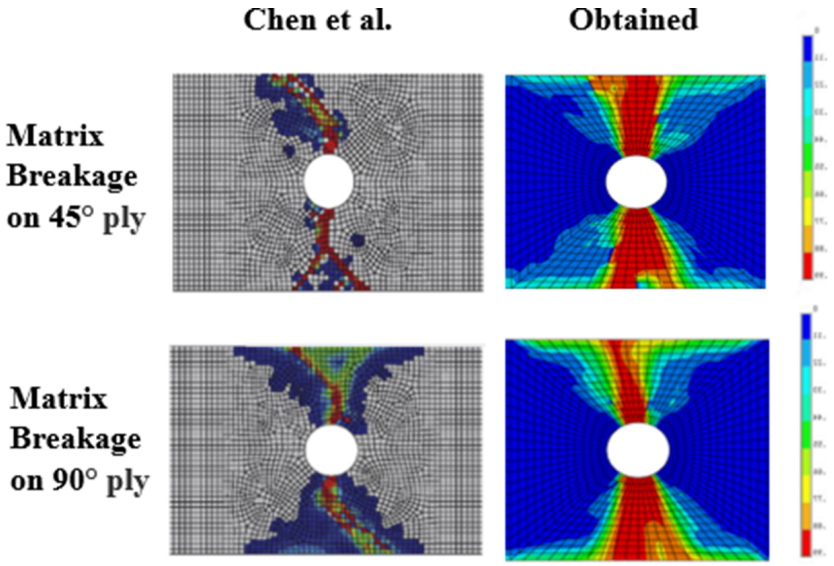

Figure 5.12: Damage distribution comparison with [111], for matrix damage following Puck criterion. Adapted from [27].

These differences might be related to the different damaged stiffness matrix models that were used or even the VUMAT formulation, which is not disclosed by the authors and can lead to differences in the material behaviour.

Relatively to the fibre damage the difference might be due to the output frequency of the model, since after catastrophic failure, damaged zones increase significantly and lead to distributions such as the ones observed. In order to verify this, the same analysis was run with one hundred times more field outputs, i.e. 100 outputs per second. The obtained fibre failure at the first ply (0°) immediately before total failure is shown on Fig.5.13.

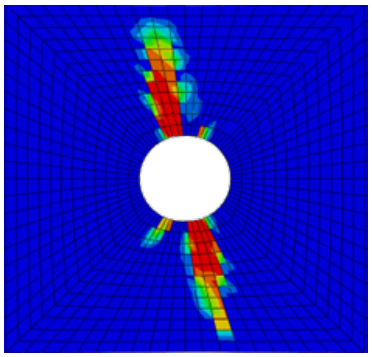

Figure 5.13: Fibre tensile damage on 0° ply immediately before total failure (Hashin criterion).

With a more refined output, a slender damaged area was captured which is more on par with previously obtained results.

Refining the mesh may also lead to a more clear damage distribution, since the degradation may evolve in a slower way. Nevertheless, at a global mechanical response, the developed VUMAT were able to accurately predict the failure loads and modes of an open hole tensile test, further validating their formulation.

Given that the strain rate value (0.003 s^{-1}) is below the threshold for the medium strain rate regime of the Strain Rate Dependent criterion, this method was employed in this model, since it would return equal results.

5.2 Low Velocity Impact

Low velocity impact is currently one of the main concerns relatively to the integrity of aerospace components, mainly due to the barely visible damage effects [112].

Ranging from matrix cracks and fibre breakage (intra-laminar) to delaminations (inter-laminar), being the latter the most dangerous due to the reduction of compressive strengh that comes with it, impact problems require rather complex computational models to accurately predict a real case scenario [112, 113].

To further verify the developed VUMAT and cohesive elements modelling, low velocity impact simulations were conducted and compared to previously obtained results.

5.2.1 Model description

The composite plate is a cylindrical shaped plate with 75 mm in diameter with eight composite UD plies, 0.25 mm each, with a $[0/90]_{2S}$ stacking sequence and seven cohesive interfaces with 0.0075 mm height each.

The impactor is a cylinder with an hemisperical head, with 15 mm in diameter and is modelled as an analytical rigid body to save computational time and resources.

The initial velocity of the impactor is set to 3.83 m/s while the given mass is 2 kg, leading to a total impact energy of 14.7 J. The impactor is also restrained in all the others degrees of freedom but the one necessary for the drop movement.

Regarding the boundary conditions, the plate is clamped at its outer face as seen on Figure 5.14.

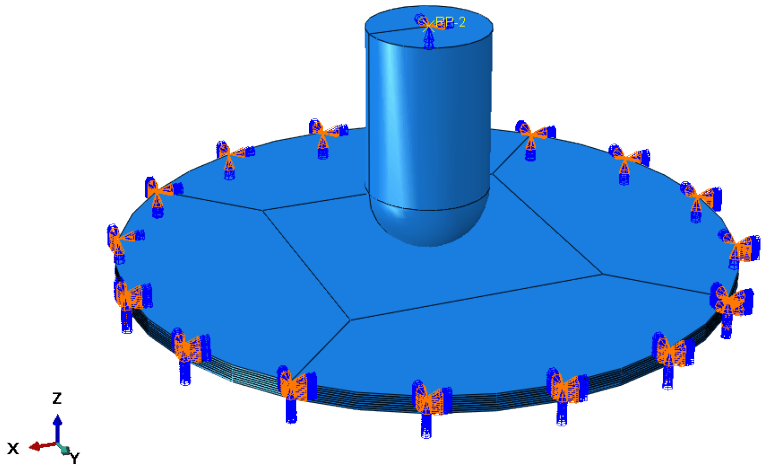

Figure 5.14: Plate, impactor and respective boundary conditions.

In the same figure, a square partition neighbored by other four can be observed. While the former is where the mesh will be refined (in order to have a better definition at the impact zone), with an approximately 1 mm sized mesh, the latter, being less relevant given the context of the problem, has an average element size of 3 mm. This partition strategy also allows the definition of a fully structured mesh. Once again, 1 element per ply and 1 element per cohesive layer was used through the thickness. The meshed plate is found on Figure 5.15.

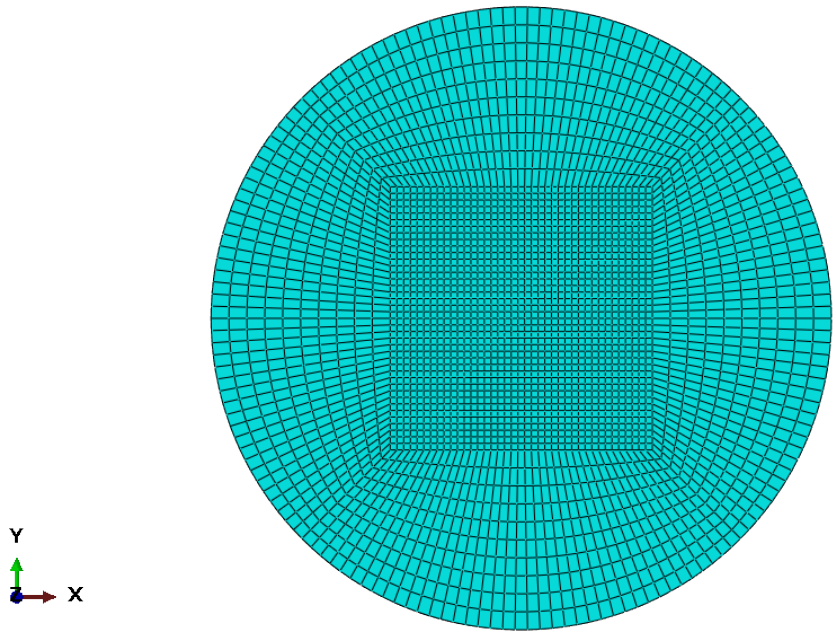

Figure 5.15: Meshed plate.

Overall, there are 25120 C3D8R elements and 51520 nodes (154560 DOF) representing the 8 composite plies, and the 7 cohesive interfaces are composed of 21980 COH3D8 elements in total. The smallest C3D8R element has an 8 mm side square top face with a total thickness of 0.250 mm^3.

One could argue that the same simulation could be done employing a quarter plate and enforcing the appropriate symmetry boundary conditions. However, it was known beforehand from the literature that the damaged zones are not totally symmetric and then, for the sake of a proper comparison, the full plate was considered.

The material properties used for the composite plies can be seen on Table 5.2.

The values of the volumetric fracture energies of the composite plies are listed in Table 5.3 and on Table 5.4, the mechanical properties of the cohesive interface are disclosed. The maximum degradation of the cohesive elements was set to 0.99 to prevent any excessive deformation that may compromise the analysis and to match the simulation parameters used in the literature [115], ensuring a proper comparison basis.

Table 5.2: Material properties for impact numerical verification [114].

Property	**Value**
Density	1600 kg/m^3
E_1 (Longitudinal Young's Modulus)	153.0 GPa
E_2=E_3 (Transverse Young's Modulus)	10.3 GPa
$\nu_{12} = \nu_{13}$ (Poisson's ratio)	0.3
ν_{23} (Poisson's ratio)	0.4
G_{12}=G_{13} (Shear Modulus)	6.0 GPa
G_{23} (Out-of-plane Shear Modulus)	3.7 GPa
X_T (Longitudinal Tensile Strength)	2537.0 MPa
X_C (Longitudinal Compressive Strength)	1580.0 MPa
Y_T (Transverse Tensile Strength)	82.0 MPa
Y_C (Transverse Compressive Strength)	236.0 MPa
S_{12}=S_{13} (Shear Strength)	90.0 MPa
S_{23} (Out-of-plane Shear Strength)	40.0 MPa

Table 5.3: Intra-laminar volumetric fracture energies for impact numerical verification [114].

Intra-laminar Volumetric Fracure Energy	**Value**
G_C^{ft}	91.6 kJ/m^3
G_C^{fc}	79.9 kJ/m^3
G_C^{mt}	0.22 kJ/m^3
G_C^{mc}	1.1 kJ/m^3

Table 5.4: Material properties of the cohesive interface for impact numerical verification [114].

Property	**Value**
Density	1600 kg/m^3
E_n=E_s=E_t (Young's Modulus)	5000.0 MPa
$T_n = T_s = T_t$ (Normal and shear strengths)	30.0 MPa
G_C^n (Mode I Fracture toughness)	0.6 N/mm
$G_C^s = G_C^t$ (Mode II and III Fracture Toughnesses)	2.1 N/mm
η (Material coefficient)	1.45

In order to simulate the interaction between the impactor and the plate, contact needs to be enforced. A general contact algorithm with hard contact normal behaviour and a penalty type tangential behaviour with a friction coefficient of 0.5 is employed for this analysis.

Since linear elements with reduced integration are being used to keep computational costs low, and some bending behavior and localised loading are expected due to the impact, the default ('Relax Stiffness') hourglass control method was employed.

Hourglassing is a purely numerical instability that happens whenever linear elements with reduced integration are being used and subjected to either localised forces/boundary conditions or bending [116].

This effect happens because instead of the stiffness matrix being integrated in all of the Gauss Points (used for the numerical integration) it is only integrated in one (reduced integration), which is in the centroid of the element. This will lead to the decrease of the rank of the matrix which introduces zero energy strain modes, as seen on Figure 5.16 [117].

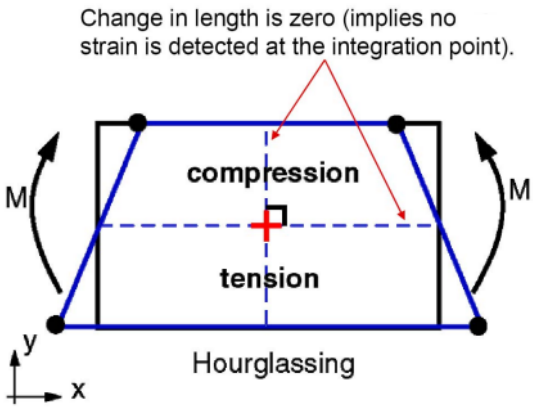

Figure 5.16: Bending behaviour of a linear reduced integration element [118].

This can either be solved by using fully integrated or quadratic elements, however, the computational cost will be higher. Therefore, some hourglass control strategies were created in order to minimize the hourglass effect while using simpler elements, which introduce internal forces (or moments) to counter-act the hourglass modes [119].

Some of these strategies and their effect is analysed and discussed further on section 5.2.3.

5.2.2 Preliminary results

Firstly, after running the analysis employing Hashin failure criterion, with the default 'Dynamic,explicit' step settings, the energy-time curve of the composite plate was extracted. This energy, including several types of energy such as internal, kinetic and frictional, allows the assessment of the energy absorbing capability and evolution of the composite structure when it comes to low velocity impact.

To obtain this plate energy, the kinetic energy of the impactor (Eq.46) was removed from the total energy of the system, whose value should be approximately constant during the analysis, since there are no external energy sources. Thus, allowing the determination of all the energy of the plate.

$$E_{impactor} = \frac{m}{2} v(t)^2 \tag{46}$$

$$E_{plate} = E_{total} - E_{impactor} \tag{47}$$

where $v(t)$ is the velocity of the impactor with respect to time. Both this value and total energy are given by the ABAQUS post processing tools.

The obtained energy-time curve of the plate can be seen on Figure 5.17. The experimental and the numerical curve obtained by Shao et al. [115] are also included as a mean of comparison.

As observed, there is a slow initial energy absorption rate followed by a steady evolution, slowing again near the 2 ms mark. While the former is caused by shape and partial contact of the impactor, which then increases in the first milliseconds of the simulation, the latter is caused by the damage the plate has endured, reducing the global stiffness and, consequently, decreasing the strain energy increase rate.

At the maximum point, the plate has absorbed all of the kinetic energy of the impactor and right after, some part is returned mainly due to the accumulated strain energy, resulting in the descent curve.

After returning some of the stored energy, the energy of the plate will reach a plateau, which allows the determination of the percentage of impact energy absorbed by the plate.

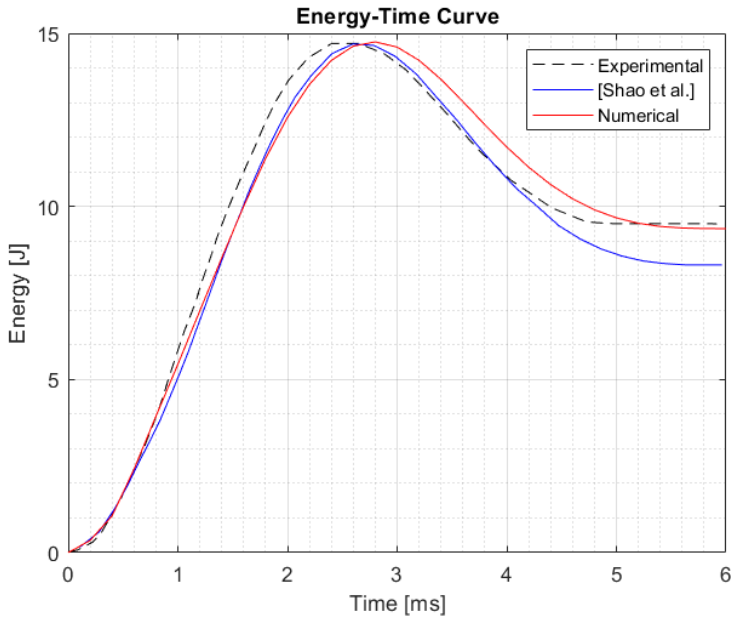

Figure 5.17: Numerical and previously existing literature energy-time curves.

The obtained curve, follows the previous numerically obtained one but then over-predicts the time at which maximum stored energy is reached and fails to represent the kinetic energy return, despite presenting a very similar evolution. However, the value of the plateau was actually much closer to the experimental result than the previous developed model, meaning that the overall inter and intra-laminar damage was better predicted in this simulation.

The total absorbed energy by the plate is 9.36 J which account for approximately 64% of the impact energy being the remainder of the energy converted to elastic deformation and vibrations.

The force-time curve was also obtained by extracting the reaction forces in the impact direction of the clamped nodes. The curve is displayed on Figure 5.18.

From the figure it is observed that there is a slight but significant under-prediction (approx. 15%) of the maximum registered experimental force. However, the predicted elastic return phase followed closely the literature results.

Some oscillations are also verified which are explained by the loss of global stiffness and other load redistribution due to the damage evolution in the plate [120]. This damage, dominated by matrix breakage and delaminations, is progressive, leading to a slower and not steep decrease of the impact force [121].

In Figure 5.19, the comparison between the literature and the obtained results matrix tensile damage distribution (layer wise) is shown.

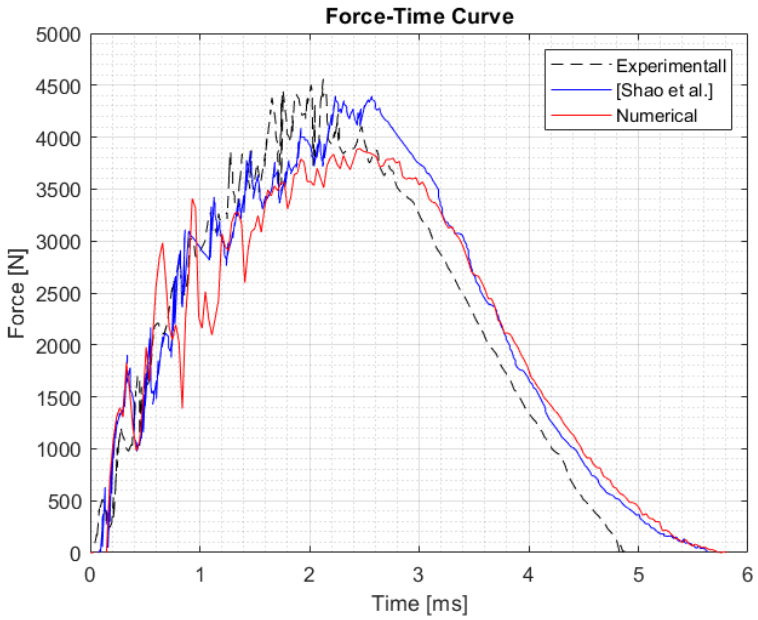

Figure 5.18: Numerical and previously existing literature force-time curves.

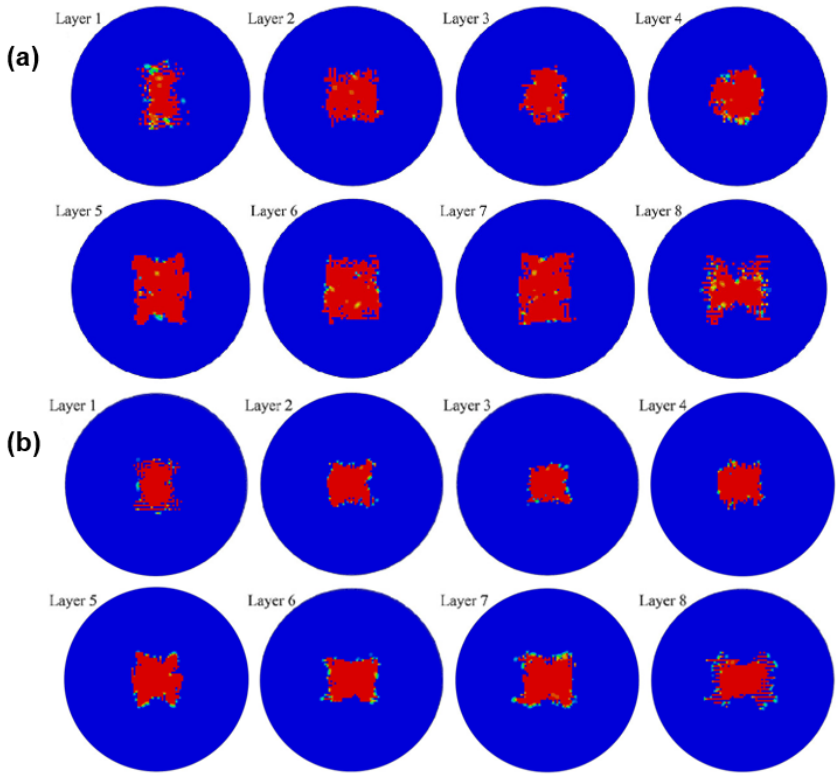

Figure 5.19: Matrix tensile damage on each composite layer: (a) Shao et al. (b) Numerical. Adapted from [115].

The size of the obtained damage zone is slightly smaller, in a general way, than the literature results, which, is most probably related to small differences in the VUMAT formulation, since, once again, it is not disclosed by the authors. However, the damage growth trend through the overall thickness remains the same, i.e., there is an increase

of the damage zone going deeper in the laminate, much due to the increased bending induced stress that is verified in the bottom of the plate. Some of the obtained shapes present an 'X' or butterfly shape that is due to the stress interaction between the perpendicular oriented plies [115].

As aforementioned, delaminations (inter-laminar damage) are one of the most important factors taking into account concerning impact on composites. In Figure 5.20, the delaminated area for each cohesive interface is shown, and the overall dimension of the delaminated zone is compared to the experimentally obtained results in Figure 5.21.

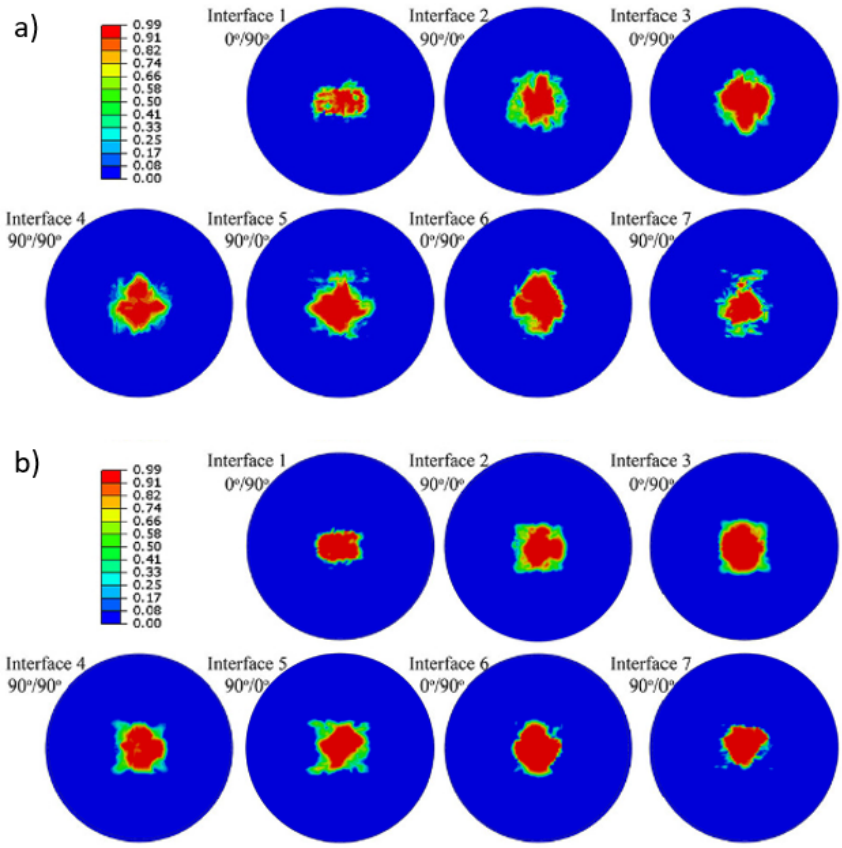

Figure 5.20: Inter-laminar damage on each interface: a) Shao et al. b) Numerical. Adapted from [115].

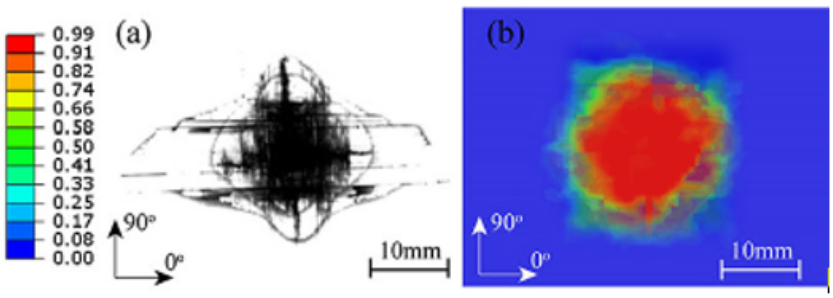

Figure 5.21: Overall delamination: a) X-ray radiograph b) Numerical. Adapted from [115].

From direct observation it is possible to say that the obtained inter-laminar damage distribution has a similar size to the ones previously obtained, although some of the interfaces such as the fifth an the seventh suggest that the damage is mirrored 180°, which, for instance, does not constitute a problem due to the symmetry of the phenomenon being studied.

The obtained overall delaminated zone is also on par with the previous obtained experimental results, showing once again that the developed material sub-routine is able to accurately predict the real life behaviour of composite parts subjected to damage.

5.2.3 Sensitivity analysis

The previous analysis was conducted using the 'Relax Stiffness' hourglass control, which, is the default method concerning explicit analysis for these kind of elements [106]. However, the type and how it is applied may have an influence in the result, and, consequently, provide less accurate results than those which may be obtained following a different formulation.

As previously mentioned, hourglass controls act by introducing internal forces (or moments) to counteract the hourglass modes. These can be either proportional to the nodal velocities, also called the viscous forms, or proportional to the nodal displacements, known as stiffness forms [119]. From ABAQUS documentation [106], the Relax stiffness formulation is given by the following expression:

$$Q = \int_0^t sK(t-t')\frac{dq}{dt}\,dt' \tag{48}$$

where q is the hourglass mode magnitude and Q the respective resistant force or moment. The hourglass stiffness is given by K and s is one scaling factor. This method is also called integral viscoelastic approach since it takes both the nodal displacement and velocity into account, the former given by the fraction inside the integral [106].

On the other hand, the enhanced hourglass method is based on the pure stiffness method which is given by setting $\alpha = 0$ in the equation below:

$$Q = s\left[(1-\alpha)Kq + \alpha C\frac{dq}{dt}\right] \tag{49}$$

where K and C are the linear stiffness and viscous coefficients respectively and s a scalling parameter. Note that the value of α controls the weight of the stiffness and the viscosity on the internal force to be added, being the method purely viscous when $\alpha = 1$, mixed when $0 < \alpha < 1$, and pure stiffness when $\alpha = 0$, the latter giving:

$$Q = sKq \tag{50}$$

On this expression, the dynamic effect of the system is not taken into account, which, in turn, might provide overly stiff responses and may not be totally adequate for high strain rate problems [106].

These introduced forces will also have some energy contribution, given by the nodal displacement times the controlling force acting on it. This additional energy is called artificial strain energy [106].

The analysis was also run with the default step viscosity. This feature, related to the bulk viscosity, works as a damper for the volumetric straining and its particularly used for high-speed events, such as the ones usually performed with explicit, preventing elements from collapsing in high speed events [106]. There two parameters controlling the bulk viscosity, one linear, b_1, and one quadratic, b_2. Recalling the expression of the stable time increment (Equation 37):

$$\Delta t = \frac{2}{\omega} \tag{51}$$

which ABAQUS/Explicit adds a damping to control oscillations [106] and thus, becomes:

$$\Delta t = \frac{2}{\omega}(\sqrt{1+\xi^2} - \xi) \tag{52}$$

this new parameter, ξ, is dependent on the user defined values for b_1 and b_2 via the following expression:

$$\xi = b_1 - b_2^2 \frac{l_c}{c_d} min(0, \dot{\varepsilon}_{vol}) \tag{53}$$

where $\dot{\varepsilon}_{vol}$ is the volumetric strain rate and l_c the previously mentioned characteristic length. Note that the quadratic parameter is only applied if the volumetric strain rate is compressive.

The bulk linear and quadratic viscosity pressures are given in the equations below:

$$p_1 = b_1 \rho c_d l_c \dot{\varepsilon}_{vol} \tag{54}$$

$$p_2 = \rho (b_2 l_c)^2 |\dot{\varepsilon}_{vol}| min(0, \dot{\varepsilon}_{vol}) \tag{55}$$

where p_1 and p_2 are the linear and quadratic bulk pressures respectively. These pressures will lead to some viscous dissipation energy, expressed as:

$$\int_V \sigma^v : \varepsilon \, dV \tag{56}$$

where σ^v is the viscous stress, which in this case, is only caused by the bulk viscosity [106].

In order to assess the influence of both hourglass control method and the step viscosity, a set of different analysis was run and the results obtained for: minimum total energy, (Min. E_T), maximum total energy, (Max. E_T), total energy difference relative to the minimum value (Δ E_T), maximum artificial strain energy, (Max. A. Strain E.), maximum viscous dissipation energy (Max. Vis. E.) and computational time (CPU time), were compiled on Table 5.5.

Table 5.5: Sensitivity analysis on hourglass control and and step viscosity.

Case	Step viscosity		Method	Min. E_T [J]	Max. E_T [J]	$\triangle E_T$ [%]	Max. A. Strain E. [J]	Max. Vis. E. [J]	CPU time [s]
	Linear	Quad.							
1	0.06	1.2	Relax	14.669	14.754	0.58	1.248	0.998	18915
2	0.06	1.2	Stiffness	14.669	14.729	0.41	0.920	1.478	15000
3	0.06	1.2	Enhanced	14.669	14.731	0.42	2.194	0.032	42474
4	0	1.2	Stiffness	14.669	14.707	0.26	0.816	1.308	25150
5	0	1.2	Enhanced	14.669	14.727	0.4	2.208	0.022	57024
6	0	0.6	Stiffness	14.669	14.703	0.23	0.769	1.041	31590
7	0	0.6	Enhanced	14.669	14.719	0.34	2.121	0.045	50996
8	0	0	Stiffness	14.669	14.699	0.21	0.722	0.809	34630
9	0	0	Enhanced	14.669	14.732	0.43	2.247	0.035	65328
10	0	0	Viscous	14.669	14.803	0.91	2.921	0.225	9897
11	0	0	Mixed (0.5)	14.669	14.731	0.42	2.228	0.112	56000
12	0	0	Relax	14.669	14.721	0.36	0.888	0.903	35121

From the table it is possible observe some trends:

- As expected, the lower the step viscosity is, the lower the viscous dissipated energy becomes;
- The pure viscous hourglass control is computationally cheaper than the remaining, however, it introduces the most artificial strain energy and higher total energy delta;
- The pure stiffness method causes less total energy unbalance than the remaining;
- The enhanced hourglass control leads to higher computational times than all of the other methods;

From these points, a generalised conclusion can be made, which is: the more viscous dependent the hourglass method is, the more artificial strain energy is introduced in the system, due to the imposed velocity on the nodes by the impact.

From all the cases, the ones with best energy evolutions were the cases 1 and 3, whose respective energy curves can be seen on Figure 5.22.

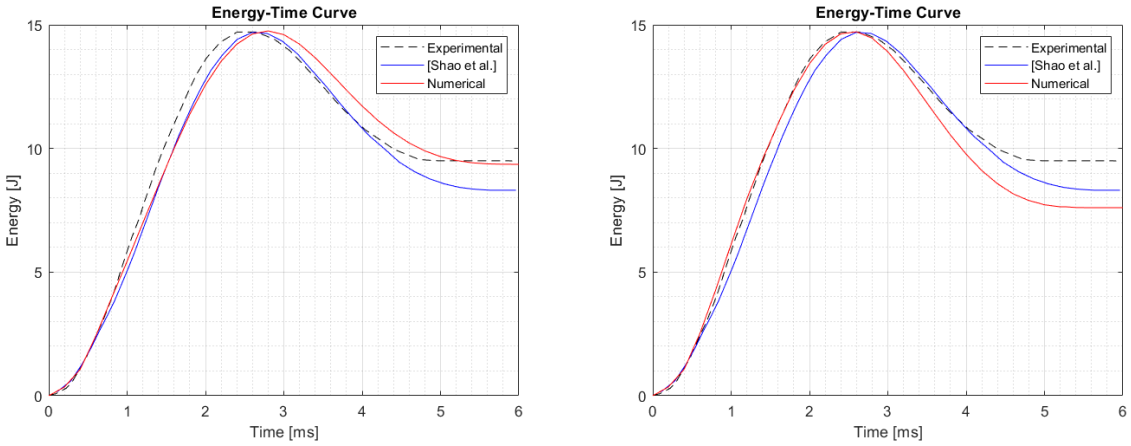

(a) (b)

Figure 5.22: Energy-time curves of case (a) one and (b) three.

The difference between them is only the hourglass control methodology, being the relax stiffness method used for one of them whereas for the other the enhanced was employed.

It is also possible to observe that both approaches present their advantages and downsides, while one of them is on par with the previous conducted simulations and predicts accurately the total final value of absorbed energy, the other predicts exactly the experimental impact phase energy absorption but underestimates the final energy value of the plate.

Given these two options, a study was conducted on the hourglass control formulations to better understand how they could influence the overall response of the plate and if there could be any other parameter that could deem better results.

Knowing the stiffness formulations and their effect on the energy-time curves, a mix between the two was tested, with the objective of getting a solution that holds a good prediction for both the beginning and end of the impact.

Given this, a relax stiffness formulation was used but with the s parameter set to 1.5, to possibly increase the stiffness effect, and, since the velocity of deformation is not substantially high, not radically change the viscous part contribution.

It should be stated that this value was not analytically estimated, being an assumption based on mathematical reasoning of the hourglass control formulations.

This new case, (relax stiffness with $s = 1.5$) will be addressed from now on as Case 13.

Following this methodology, the obtained energy-time curve is presented on Figure 5.23.

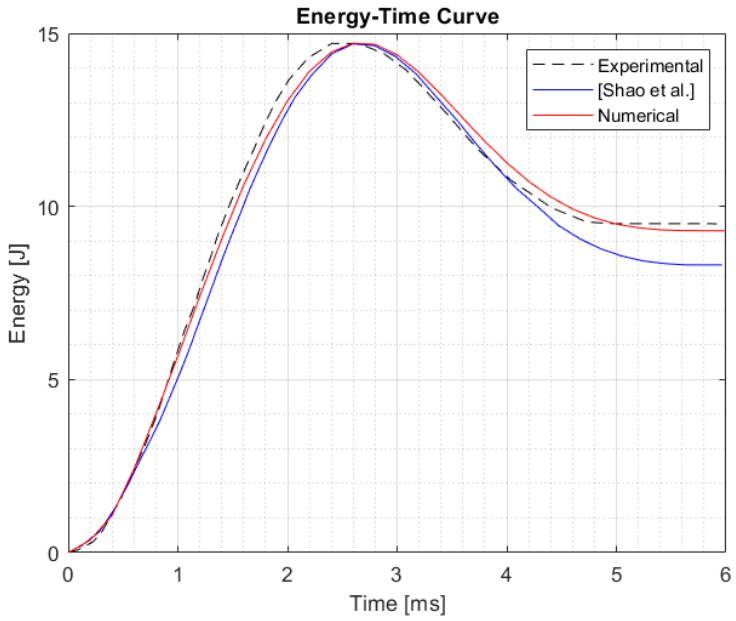

Figure 5.23: Case 13 (relax stiffness with $s = 1.5$) energy-time curve.

It is possible to observe that although the model does not predict the initial phase as accurately as the solution using the pure stiffness hourglass control, it holds a better global response compromise.

A similar table as the one previously presented for the sensitivity analysis was created for these three cases and can be seen below (Table 5.6):

Table 5.6: Energy summary and computational time for cases 1, 3 and 13.

Case	Step viscosity		Method	Min. E_T [J]	Max. E_T [J]	Δ E_T [%]	Max. A. Strain E. [J]	Max. Vis. E. [J]	CPU time [s]
	Linear	Quad.							
1	0.06	1.2	Relax	14.669	14.754	0.58	1.248	0.998	18915
3	0.06	1.2	Enhanced	14.669	14.731	0.42	2.194	0.032	42474
13	0.06	1.2	Relax ($s = 1.5$)	14.669	14.735	0.45	1.172	1.170	27772

From the table it can be seen that case 13 led to a decrease in the maximum artificial strain energy, which, as aforementioned, is typical of 'stiffer' hourglass control methods, meaning that the increase in the scaling parameter, s, led to a stiffening effect.

The computational time increased relative to the 'Relax' method but was still lower than the enhanced, meaning better results could be obtained with lower computational costs, just by numerical tuning of the parameters (i.e. hourglass control).

In order to assess the similarity to the experimental results of [114], a MATLAB [122] script was created to calculate the correlation between the different curves.

Since the experimental and obtained curves do not present the same array dimensions (having the former less sample points), it is necessary to interpolate the values of the obtained curves at the time intervals where the experimental value is known. This was done using a modified Akima Piecewise Cubic Hermite [122] interpolation strategy.

After having the interpolated values, the proximity between the two curves was calculated via the mean squared error (MSE), defined by hte following expression:

$$MSE = \frac{1}{n}\sum_{i=1}^{n}(E_i - e_i)^2 \tag{57}$$

where n is the total number of time instants evaluated, E_i, the ordinate values of the experimental curve and e_i the ordinate values of the curve being evaluated.

The obtained MSEs relatively to the experimental result can be found on Table 5.7

Table 5.7: Mean square error relatively to the experimental curve of the best results.

Case	MSE
Case 1	0.3558
Case 3	0.7143
[Shao et al.]	0.4566
Case 13	0.0801

As expected, the curve from case 13 presented the lowest MSE between the options, therefore, being the most accurate of all the studied cases.

Given this a similar analysis to the preliminary results was done for case 13 and is presented in the next section.

5.2.4 Results

Having already determined the energy-time evolution (Figure 5.23), the force-time curve was also computed and shown on Figure 5.24.

From the figure, it is possible to observe that there was an improvement on the force evolution as well, being this method capable of more accurately predicting the impact phase and reaching a slightly closer maximum load than with the default configurations (Case 1).

Once again, the predicted elastic return force evolution is closer overall to the experimental results than that obtained by previous authors.

Similarly to the preliminary results, the matrix tensile damage is shown in Figure 5.25.

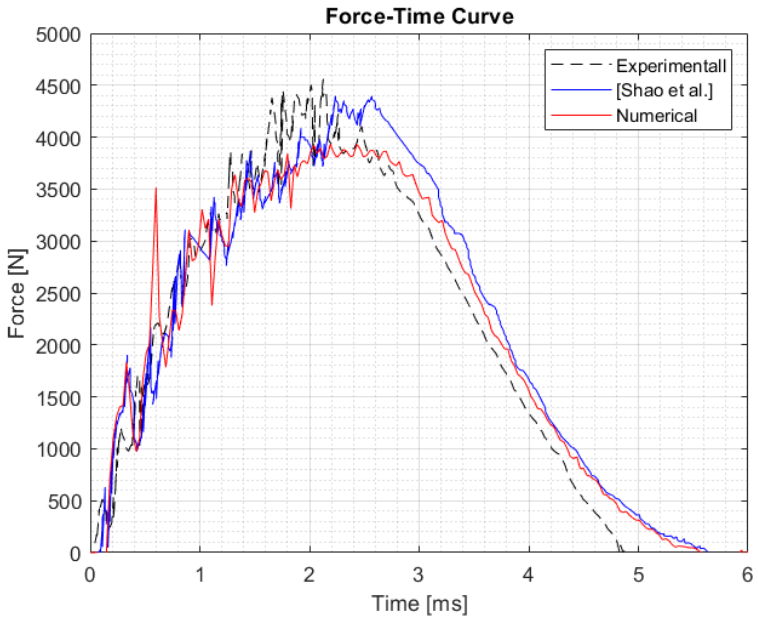

Figure 5.24: Case 13 force-time curve.

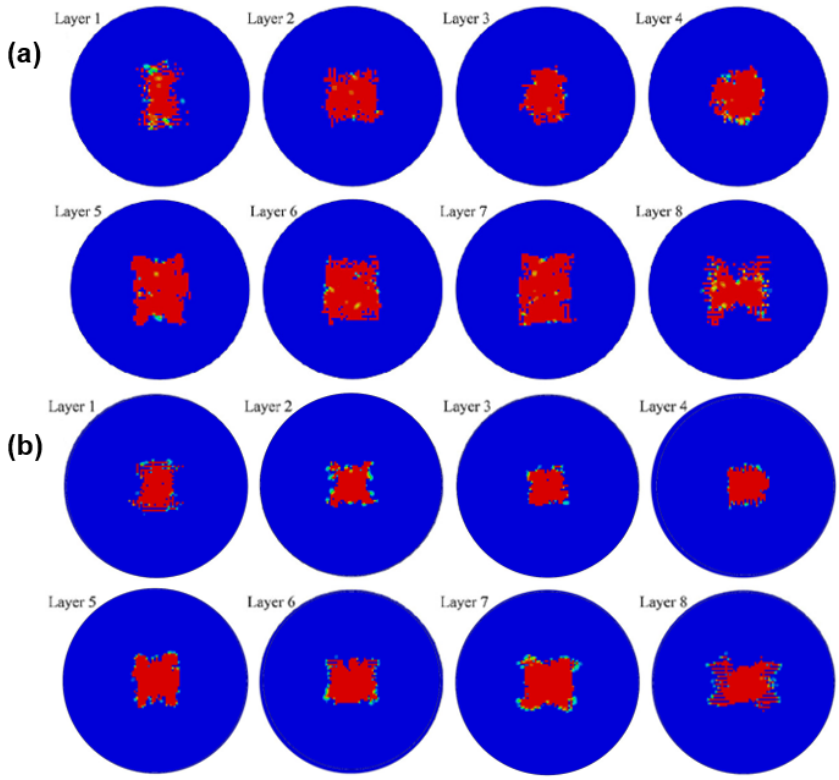

Figure 5.25: Case 13 matrix tensile damage on each composite layer: a) Shao et al. b) Numerical. Adapted from [115].

From the analysis of the damaged zones it is possible to conclude that the obtained distributions are smaller in a global level, however, the damage shapes are close to those previously obtained.

It is worth noticing that there is no experimental data to fully validate these results, meaning that this comparison is mainly being used to assess if the developed VUMAT returns similar results than those previously obtained, assuming the benchmark VUMAT was properly defined.

This way, and given that the overall energy-time curve is closer to the experimental one, it might be possible that the obtained damaged distribution is closer to the reality, however, there is no available data to support this hypothesis.

The cohesive damage for each interface is also shown of Figure 5.26 as well as the global delaminated area 5.27.

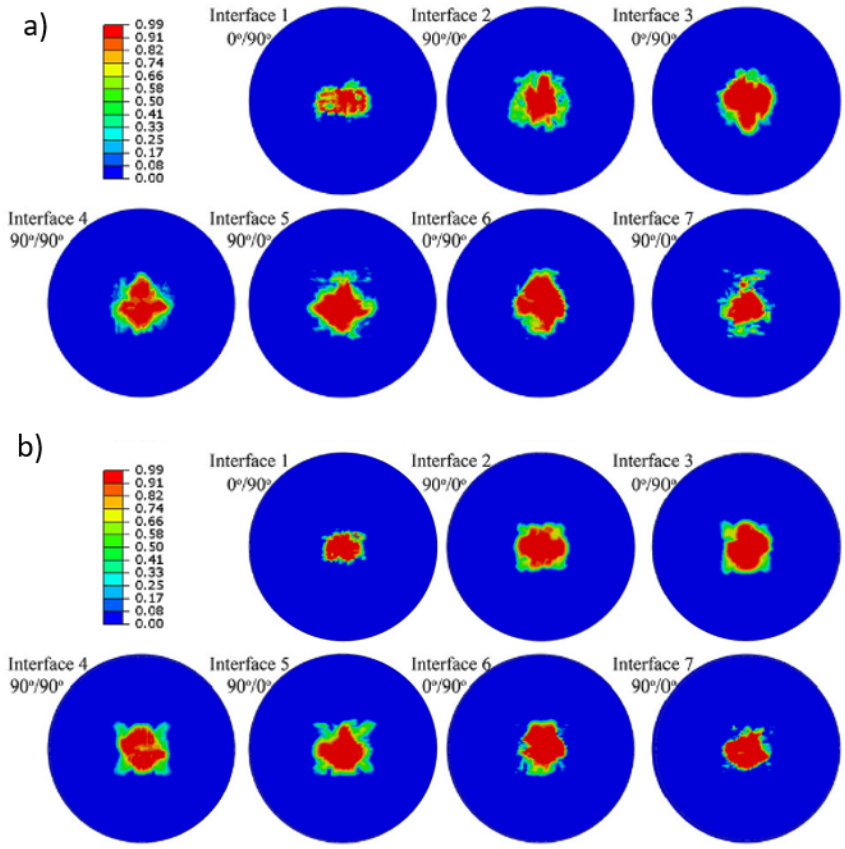

Figure 5.26: Inter-laminar damage on each interface: a) Shao et al. b) Case 13. Adapted from [115].

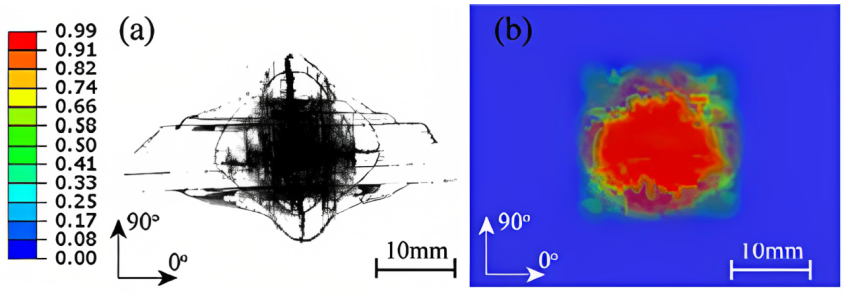

Figure 5.27: Overall delamination: a) X-ray radiograph b) Case 13. Adapted from [115].

From the figures is possible to see that the size and shape of the delaminated areas is on par with previously obtained results, which, similarly to the matrix damage distribution, do not have any experimental data to compare to.

However, the global delaminated area was captured via X-ray and the obtained results are very close if not equal to the expected results.

Following these comparisons, it can be firmly assumed that the developed VUMAT is well defined and able to reproduce complex engineering problems.

In order to verify the other developed VUMAT, the same analysis were run employing both the Puck an the strain rate dependent (Hashin) failure criteria.

The obtained curves, running the analysis with the same parameters as case 13, are shown on Figure 5.28.

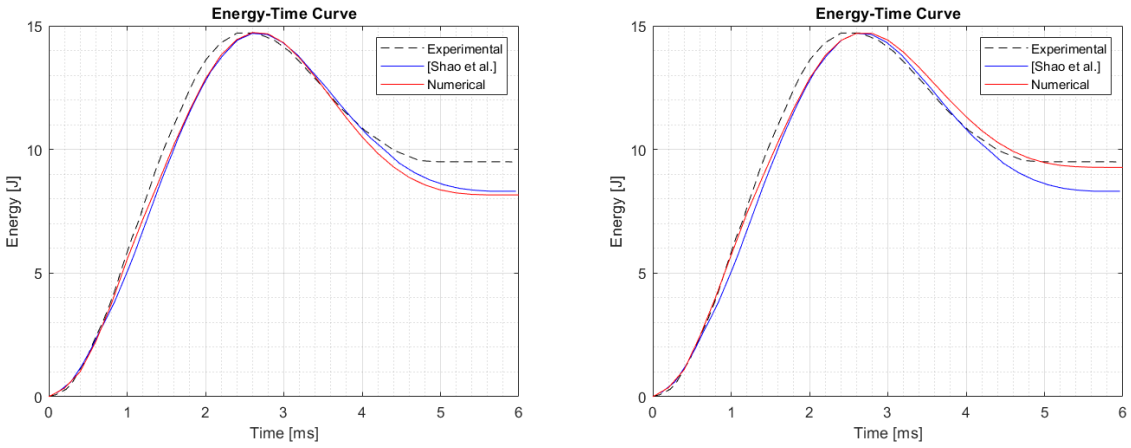

(a) (b)

Figure 5.28: Energy-time curves employing (a) Puck and (b) Strain Rate Dependent criteria.

It can be observed that employing the Puck formulation, a very close result to the previously obtained in literature is achieved, although predicting slightly better the initial impact phase. On the other hand, using the strain rate dependent criteria, a better overall prediction is made, however, slightly worse than the previously presented case 13.

A table (Table 5.8) containing the MSEs of these two new cases is presented below:

Table 5.8: Mean square error relatively to the experimental curve of both Puck and Strain Rate Dependent (SRD) failure criteria.

Case	**MSE**
Case 1	0.3558
[Shao et al.]	0.4566
Hashin	0.0801
Puck	0.4193
SRD	0.1426

Both methods (Puck and SRD) present a better prediction relatively to the previously obtained numerical results in the literature, having the strain rate dependent criterion a more significant improvement, however, the Puck criterion performance is worse than the default (Case 1) one.

This can be explained by the simulation parameters that may not hold valid for these two new cases, moreover, the two shear stiffness loss parameters, S_{mc} and S_{mt}, which have proven to significantly change the results [86], may also need to be tuned to account for the different failure criteria, specially for the Puck formulation, since it has a more significant effect on the damage formulation.

The strain rate set of scaling parameters or even the VUMAT formulation, given it considers the transverse out-of-plane stiffness change equal to the in-plane stiffness one, may also not be totally accurate, despite the relatively good performance of the obtained result following this criterion.

Nevertheless, given that all of the developed criteria presented a closer approximation to the experimental results than the literature, it is possible to confirm that the VUMAT development was done in accordance to what was expected.

6 Sub-Cargo Element

In this section, the impact behaviour of a sub-cargo element of a commercial aircraft fuselage will be studied via a developed virtual certification model.

6.1 Test specimen and model description

The studied feature is a composite 'C' section stanchion used in the sub-cargo zone of the fuselage based on the one analysed by Riccio et al. [123]. However, in this work, a 3D element formulation is employed whereas in the mentioned source, continuum shell elements were used. Moreover, a different element through the thickness configuration was used, as further detailed in this section.

Figure 6.1 shows the overall dimensions of the composite column.

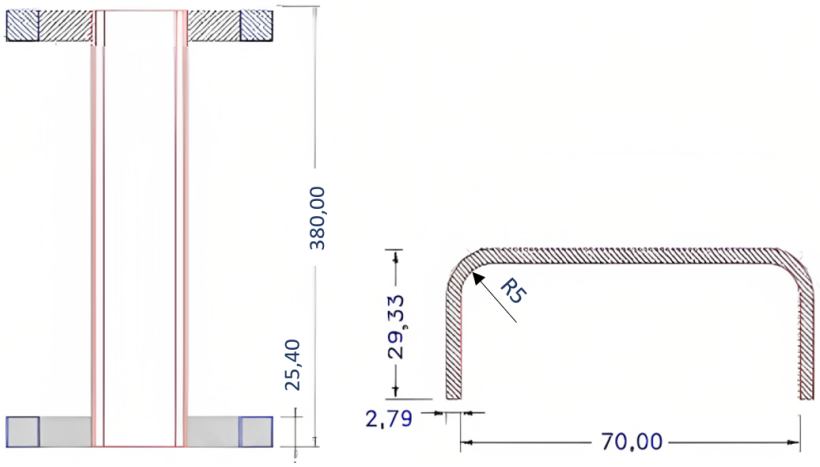

Figure 6.1: Geometric details of the stanchion. Adapted from [124].

The overall thickness of the laminate is 2.79 mm with fifteen plies (whose layup can be seen on Figure 6.2) and fourteen 0.005 mm thick cohesive interfaces.

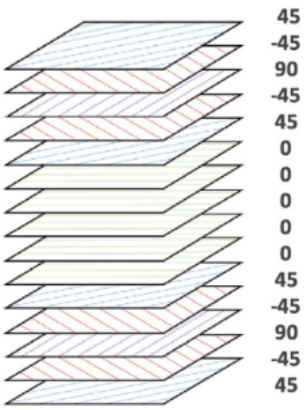

Figure 6.2: Stacking sequence of the stanchion [123].

For this specific case, and for the validity of the comparison with previous results, the Power Law criterion will be used instead of the B-K.

The material and cohesive properties are displayed on Tables [6.1-6.3].

Table 6.1: Material properties of the stanchion laminae [123].

Property	**Value**
Density	1600 kg/m^3
E_1 (Longitudinal Young's Modulus)	137.0 GPa
E_2=E_3 (Transverse Young's Modulus)	8.43 GPa
$\nu_{12} = \nu_{13}$ (Poisson's ratio)	0.26
ν_{23} (Poisson's ratio)	0.4
G_{12}=G_{13} (Shear Modulus)	4160.0 MPa
G_{23} (Out-of-plane Shear Modulus)	3328.0 MPa
X_T (Longitudinal Tensile Strength)	2256.0 MPa
X_C (Longitudinal Compressive Strength)	800.0 MPa
Y_T (Transverse Tensile Strength)	100.0 MPa
Y_C (Transverse Compressive Strength)	171.0 MPa
S_{12}=S_{13} (Shear Strength)	85.0 MPa
S_{23} (Out-of-plane Shear Strength)	40.0 MPa

Table 6.2: Intra-laminar volumetric fracture energies of the stanchion laminae [123].

Intra-laminar volumetric fracure energy	**Value**
G_C^{ft}	47.58 kJ/m^3
G_C^{fc}	6.01 kJ/m^3
G_C^{mt}	1.53 kJ/m^3
G_C^{mc}	4.48 kJ/m^3

Table 6.3: Material properties of the cohesive interfaces of the stanchion [123].

Property	**Value**
Density	1600 kg/m^3
E_n=E_s=E_t (Young's Modulus)	100000 MPa
T_n (Normal Strength)	27.5 MPa
$T_s = T_t$ (Shear Strengths)	60.0 MPa
G_C^n (Mode I Fracture Toughness)	0.288 N/mm
$G_C^s = G_C^t$ (Mode II and III Fracture Toughnesses)	0.61 N/mm

The mesh was set to have an overall element size of 4 mm and is represented on Figure 6.3.

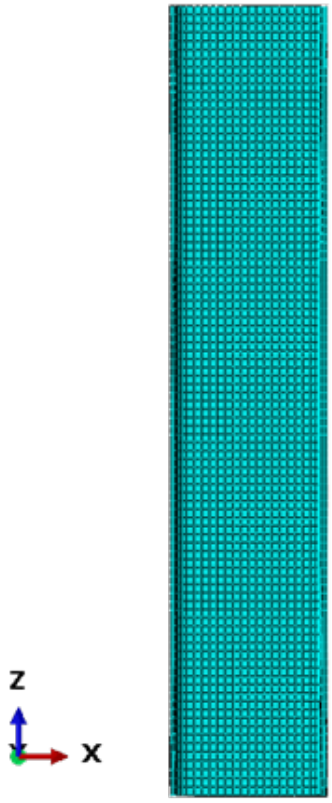

Figure 6.3: Meshed stanchion.

Contrarily to the previously mentioned source, one element for each ply instead of one element for each set of three plies was used, the two different approaches are depicted on Figure 6.4.

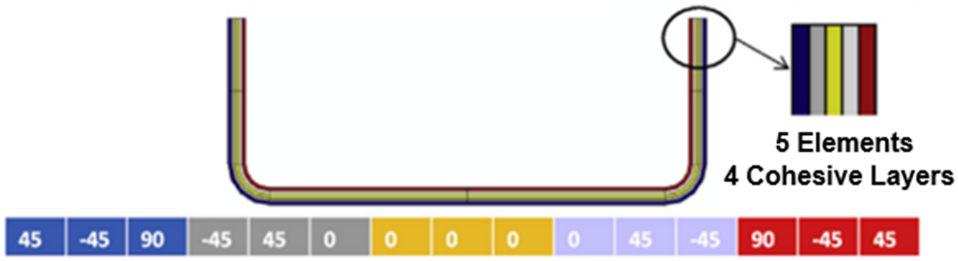

(a)

(b)

Figure 6.4: Number of elements through the thickness. (a) one element per 3 plies [123] and (b) one element per ply. Adapted from [123]

Regarding the interfaces, one element for each was employed, meaning 29 elements in total were employed in the thickness direction. On total, the mesh is composed of 45120 C3D8R and 42112 COH3D8 elements with a total of 94050 nodes (282150 DOF). The smallest element has a top face area of 10.96 mm^2 and a thickness of 0.186 mm.

The boundary conditions were set to match as accurately as possible the experimental setup, shown on Figure 6.5.

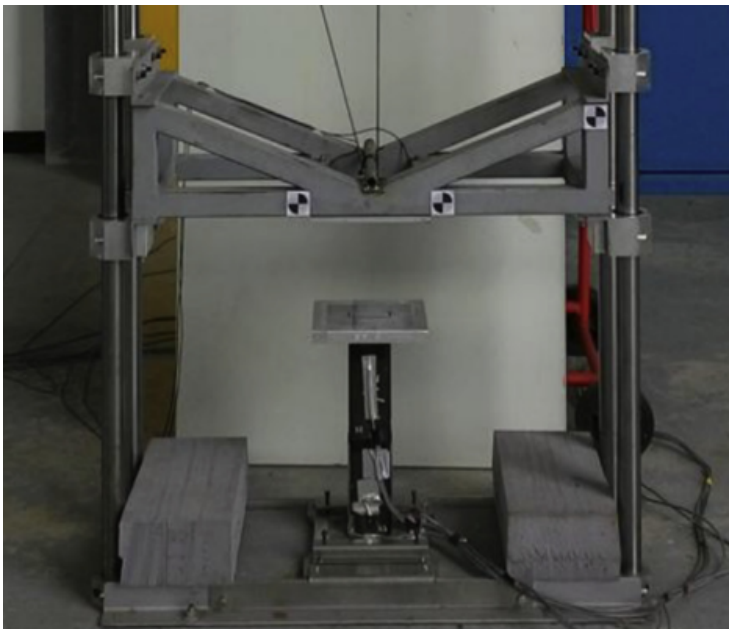

Figure 6.5: Experimental setup [123].

The test specimen was potted in an epoxy resin mould at its extremities, therefore, a constraint of $U_x = U_y = 0$ was applied at the outer surfaces, 25.4 mm from the outer edges (bottom and top). Additionally, the elements at the bottom face were fixed. The boundary conditions can be seen on Fig 6.6.

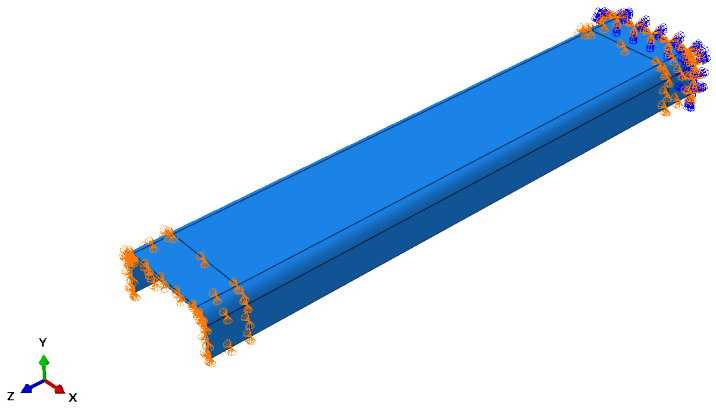

Figure 6.6: Boundary conditions of the model.

Note that with this configuration, the top potted elements are able to move in the vertical (Z) direction. Also, a general ('All with self') contact algorithm with 'Hard' contact setting for normal behaviour and a penalty friction formulation with a coefficient of 0.5 for the tangential behaviour was used.

6.2 Quasi-static test

After generating the numerical model, a quasi-static compression test was performed using ABAQUS/Explicit to assess the overall response and stiffness of the structure.

A vertical displacement of 1 mm over 30 s was imposed at the top face nodes of the stanchion, having the reaction force and displacement been probed by two previously crated node sets, one constituted by the nodes clamped at the bottom face and other by a representative node of the top face, since all of the elements have the same displacement at this zone.

Once again, to keep the simulation time as low as possible, a mass scaling strategy was employed, being the density multiplied by one million times its original value. Figure 6.7 shows the load-displacement curves of the obtained and experimental results while the Figure 6.8 shows the deformed shape of the stanchion at the end of the simulation.

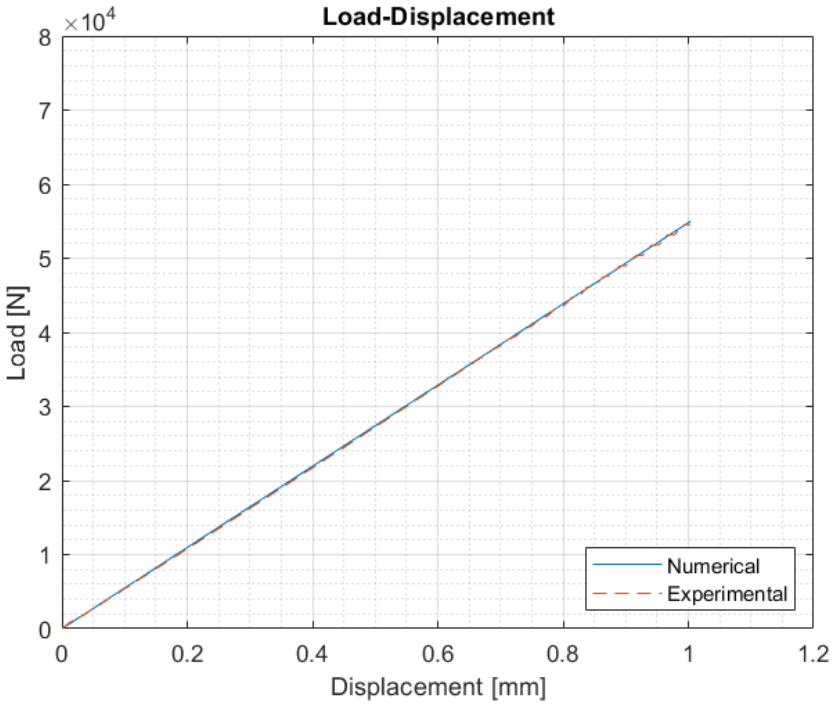

Figure 6.7: Experimental and numerical quasi static load-displacement curves.

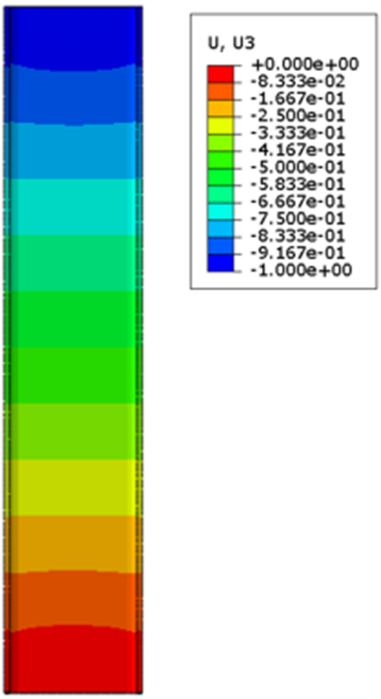

Figure 6.8: Deformed shape after the quasi-static compression.

As observed, the obtained stiffness is nearly identical to the experimental result, which values can be seen on Table 6.4.

Table 6.4: Experimental and numerical stiffness values.

	Stiffness	**Error**
Experimental	54.8 kN/mm	[-]
Numerical	54.673 kN/mm	0.23%

From the very low relative error relatively to the experimental result, it is possible to verify that the orientations of the plies, material properties and the elastic part of the VUMAT are appropriately defined.

6.3 Impact tests

Having verified the model of the stanchion, two impact tests, with different impact energies were conducted, to assess the dynamic behavior in both elastic and crash regimes. To do this, an analytical rigid impactor was created and added to the assembly model, approximately 0.3 mm away from the top face. Its initial velocity and mass were set to the values of the ones used for the experimental test, which can be seen on Table 6.5.

Table 6.5: Impact tests.

	Impact Energy	**Impactor mass**	**Velocity**
Low Energy Impact	42 J	26 kg	1.8 m/s
High Energy Impact	585 J	77 kg	3.9 m/s

In the following sections, the results for each one of the impact tests will be presented and analysed.

6.3.1 Low Energy Impact

The objective of the low energy impact is to evaluate the overall dynamic behaviour of the stanchion. To do this, a spring-mass model as suggested in previous works [123] will be used to determine the analytical solution which will then serve as a mean of comparison for the simulation results.

Each element of the system, both impactor and stanchion have their own equation of motion, however, with some simplifications and assumptions, it is possible to represent the problem in a simple equation:

$$M\ddot{x} + Kx = 0 \tag{58}$$

Where M is total mass of the system and K the previously obtained stanchion stiffness.

The general solution is known and has the following formulation:

$$x = A \sin \omega t + B \cos \omega t \tag{59}$$

where ω is the natural frequency of the system and given by

$$\omega = \sqrt{\frac{K}{M}} \tag{60}$$

Enforcing Equation 60 and the initial conditions ($\dot{x}(0) = V, x(0) = 0$) on Equation 59, where V is the initial velocity of the impactor, the final movement equation is:

$$x = \frac{V}{\omega} \sin \omega t \tag{61}$$

Additionally, knowing the displacement evolution, it is possible to determine the reaction force (symmetric to the impact force) by multiplying the displacement by the stanchion stiffness.

$$F = Kx \tag{62}$$

The analytical and numerical results for the displacement and force are shown on Figures 6.9 and 6.10 respectively.

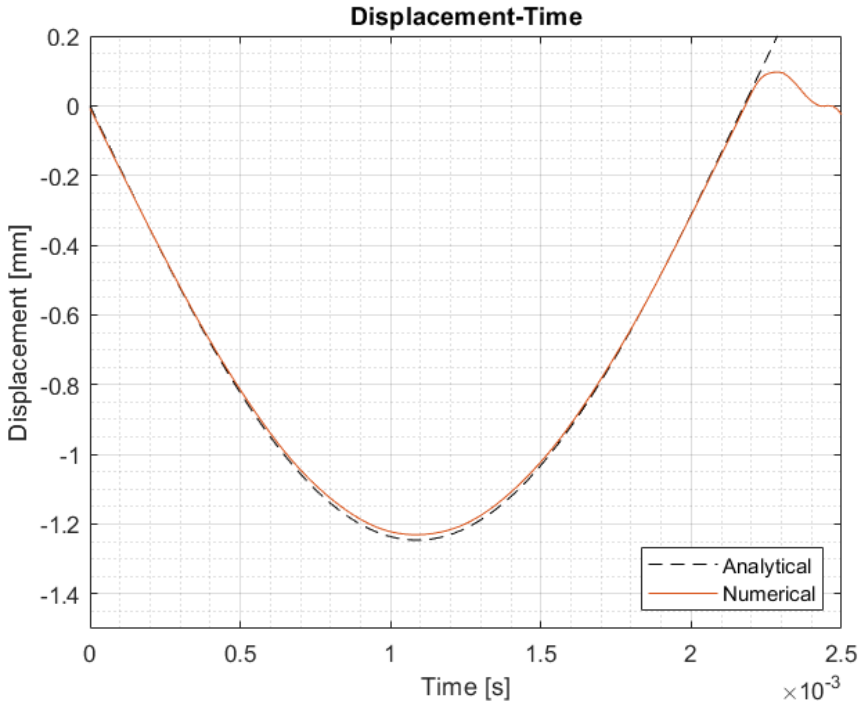

Figure 6.9: Analytical and numerical displacement-time curves.

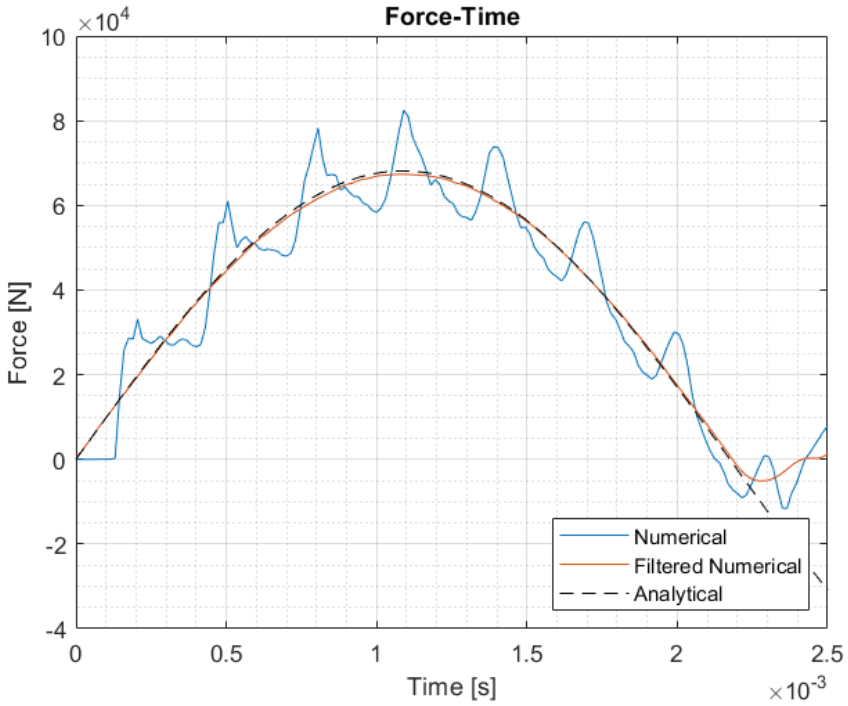

Figure 6.10: Analytical, numerical and filtered numerical force-time curves.

From the figures, an excellent relation between the obtained and the analytical results can be observed. The difference between the analytical maximum displacement, $x = -1.246$, and the obtained, $x = -1.230$, leads to a relative error of about 1.3%, and the relative error between the maximum forces is around 1.1%, meaning that the composite column follows closely the expected behaviour. It can also be observed that around the 2.2 ms mark, the impactor separates from the stanchion

For the force-time plot, a moving average filter (Equation 63) was used to even out the numerical response, which oscillatory behaviour is due to the approximations made considering the same time step for all the elements [125], having the window size been set to 20 (the one that deemed better results) and slightly shifted to start to meet the analytical curve.

$$F(n) = \frac{1}{WindowSize}(f(n) + f(n-1) + ... + f(n-(WindowSize-1))) \tag{63}$$

where $f(n)$ are the values of the numerical obtained force array.

The energy-time curves of both kinetic and internal energies were also compared to the analytical expected values. The analytic value for the kinetic energy was obtained considering the mass of the impactor, and the velocity was considered as the derivative of the previously obtained displacement:

$$\dot{x} = V \cos \omega t \tag{64}$$

Since no other dissipating sources are present or at least not significant to the point they can be considered as negligible, the internal energy is estimated by subtracting the kinetic energy to the total 42 J.

The obtained and analytical results for the evolution of these two energies are shown on Figure 6.11.

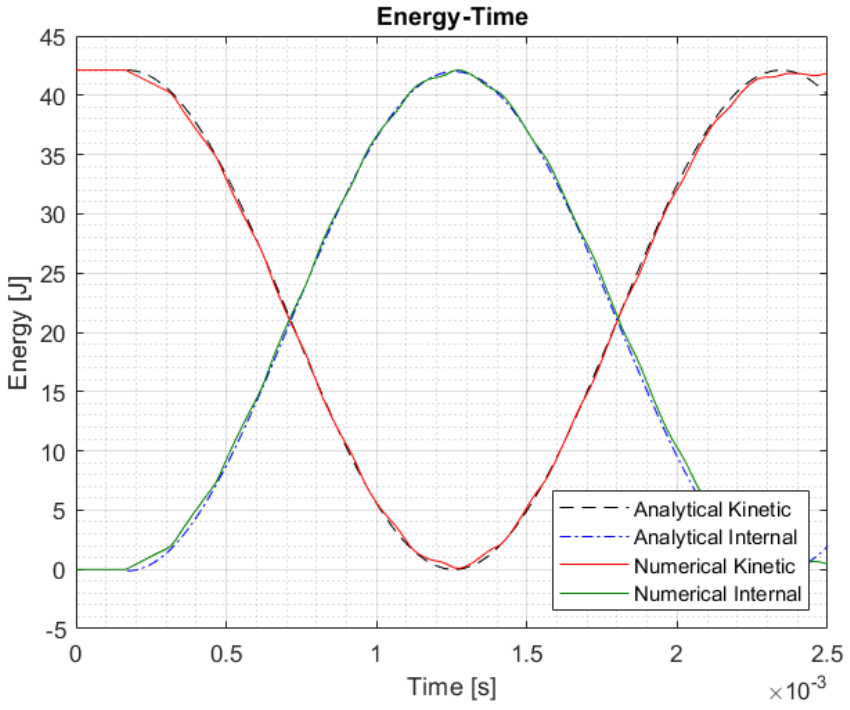

Figure 6.11: Analytical and numerically obtained kinetic and internal curves.

As seen from the figure, since the energy values return to their original values, there was no damage on the composite stanchion. This was confirmed by the state variables which did not indicate any matrix or fibre damage.

It is also verified an exact agreement between the analytical and obtained curves, further reinforcing the well definition of both the stanchion model and the VUMAT.

6.3.2 High Energy Impact

All the previous developed VUMAT, numerical verification and validations end in the topic approached in this section which is the high energy impact (crash) of a composite fuselage element.

The analysis was firstly run using the Hashin failure criterion, and, to avoid excessive deformation or numerical issues, the damage parameter was capped at 0.95 for all the failure modes.

Manufactured parts, contrarily to finite element models, are not geometrically perfect and thus, may present slight imperfections that can and have proven to influence their behavior, specially under compression [126].

To take this into account, a linear buckling analysis of the stanchion was done, which required both the element formulation (from explicit to implicit) and the material definition to be changed, since the VUMAT is only defined for explicit analysis, keeping the same mesh and orientation details.

The new material was set to a purely elastic one, with the same elastic constants of the material of interest.

After determining the first buckling mode shape, the nodal displacements were retrieved and applied, after multiplied by a scaling factor of 0.05, as a perturbation of the initial node coordinates of the high energy impact model.

Hashin Failure Criterion

The analysis was run for a total of 0.015 s, and the obtained shapes during the post-buckling impact are found on Figure 6.12 and the respective final shape details on Figure 6.13.

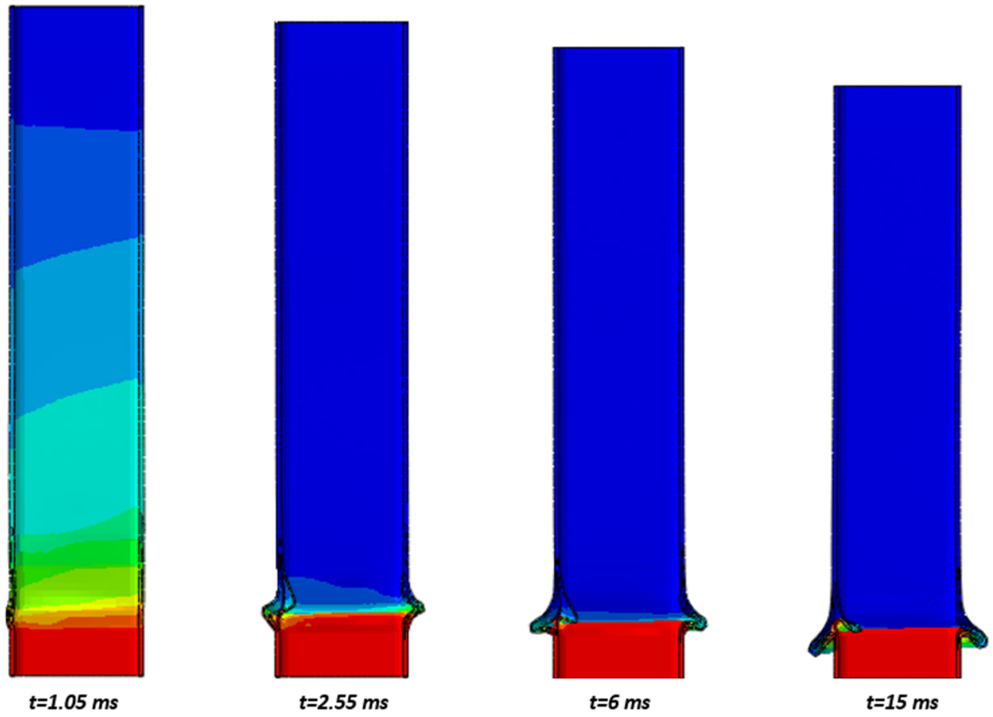

Figure 6.12: Evolution of the deformed shape, using Hashin failure criterion.

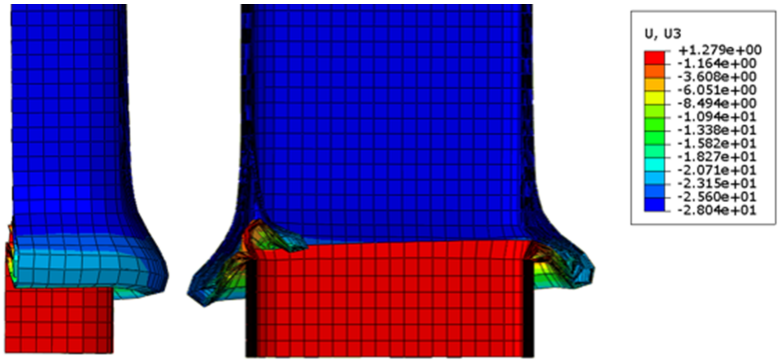

Figure 6.13: Detail of the deformed shape 15 ms after impact, using Hashin failure criterion.

From the deformed shape, it is possible to draw some conclusions about the behaviour of the stanchion. Firstly, the failure occurred in the bottom, near the boundary condition. The occurrence of delaminations is also clearly visible on the formed folds on the sides. Realistically, these folds would not deform beyond the potting surface and would flatten once in contact with it.

Nevertheless, it would be beneficial to determine the type of failure driving global collapse of the structure. Post-processing the results, it is possible to observe that the variable controlling the cohesive damage, SDEG, had already reached the value of 0.675 at 0.3 ms after impact, before any other type of intra-laminar damage had started. However, as seen from Figure 6.14, it is verified close to the boundary condition, thus, possibly being numerically 'contaminated' by it. For the sake of clarity, all of the next images of the model employing Hashin criterion will have the potting elements removed.

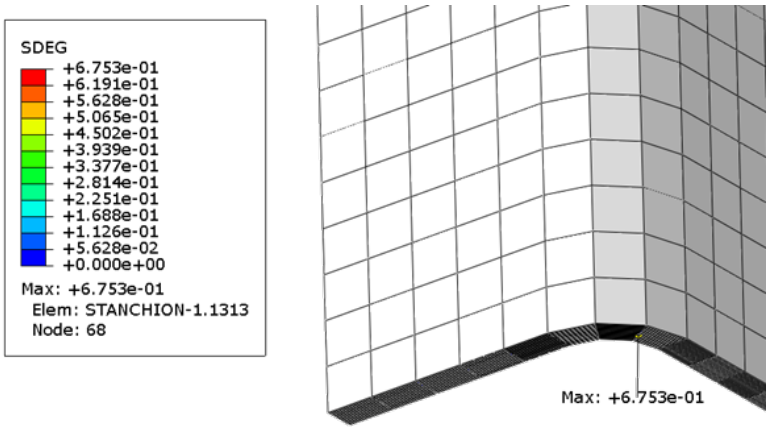

Figure 6.14: First non-zero SDEG value registered at the interface between the stanchion and the potting (0.3 ms after impact).

The first recorded total failure, is the fibre compression mode, mainly verified at the unidirectional set of plies in the lower middle of the laminate (Figure 6.15). At the same time, there is the damage onset of both matrix types of damage and more importantly, the full delamination between the 0° and 45° plies. This is mainly caused by the great difference in stiffness between them (in the impact direction), leading to high shear stresses in the interface.

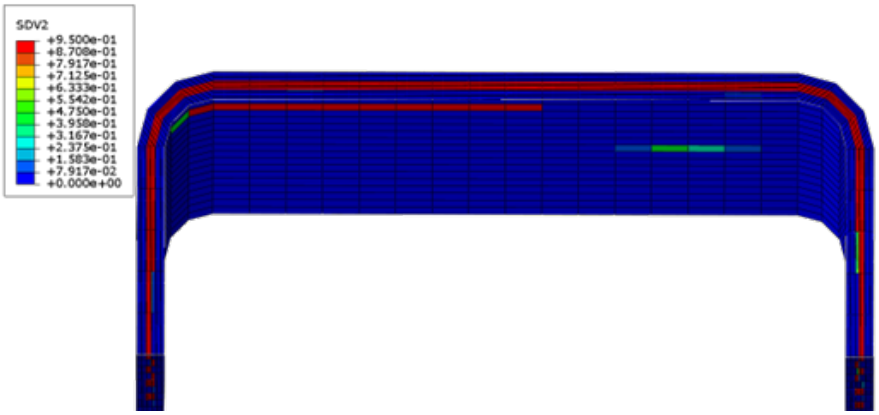

Figure 6.15: Fibre compression failure distribution at the first registered total failure (0.6 ms after impact).

Once the first failure and delaminations occur, the progressive crushing leads to the compressive failure of the matrix and fibres of the outer plies, this time, caused by the loss of load carrying capability of the interior ones. In order to better analyse the damage distribution, an analysis through the thickness of a flange element is shown on Figure 6.16.

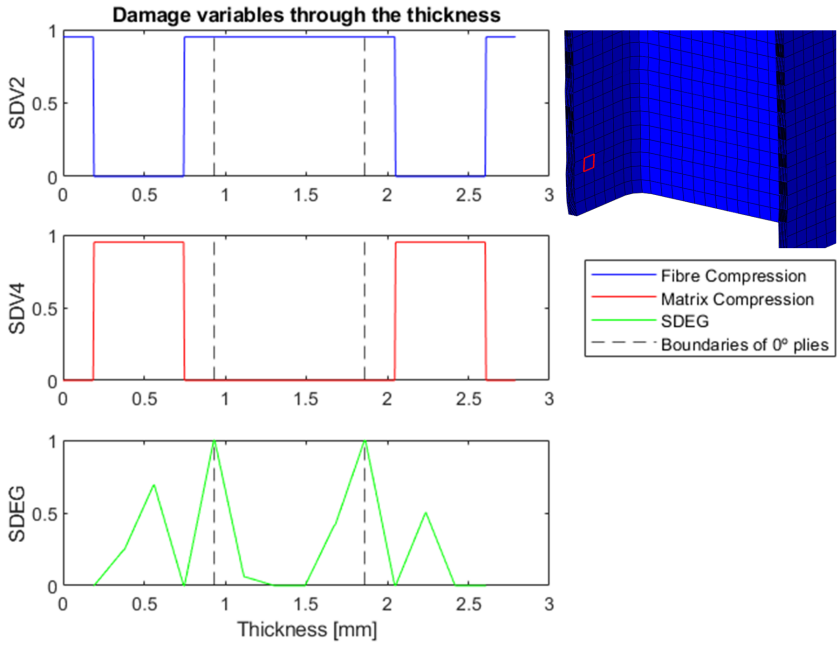

Figure 6.16: Damage variables through the thickness of a 12 mm above potting flange element (0.75 ms after impact).

As it can be observed, at this stage, there is almost a symmetric damage distribution were the central part of the laminate has failed due to fibre compression and the outer parts mainly due to matrix compression. It this figure, the full delamination, given by SDEG=1, between the central 0° block and the remaining of the plies is also clearly demonstrated.

Some 45° plies have also failed under fibre compression mainly due to the local buckling effect that is starting to take place (Fig.6.17). Due to the same phenomenon, matrix tensile failure increases owing to the additional bending stresses.

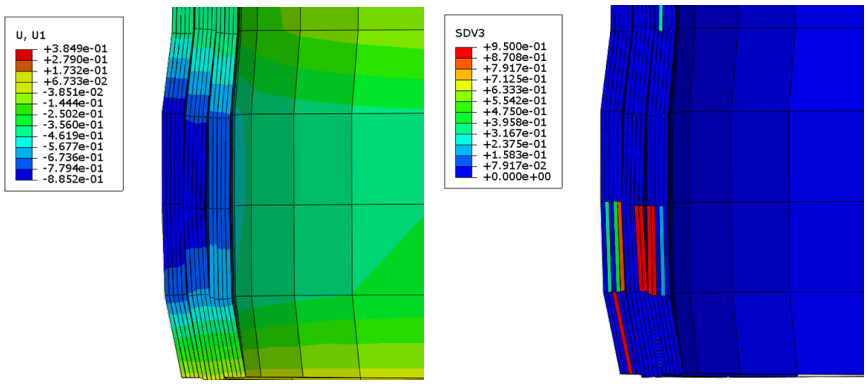

(a) (b)

Figure 6.17: Local buckling (a) lateral displacement and (b) matrix tensile damage due to bending stress (0.85 ms after impact).

Once the local buckling effect increases, there is the unstable failure of the stanchion, the delaminations start to propagate and the structure loses almost all of its load carrying capability, starting the plies to fold on top of each other leading to the final deformed shape. Some of these phenomenons can be seen on Figure 6.18.

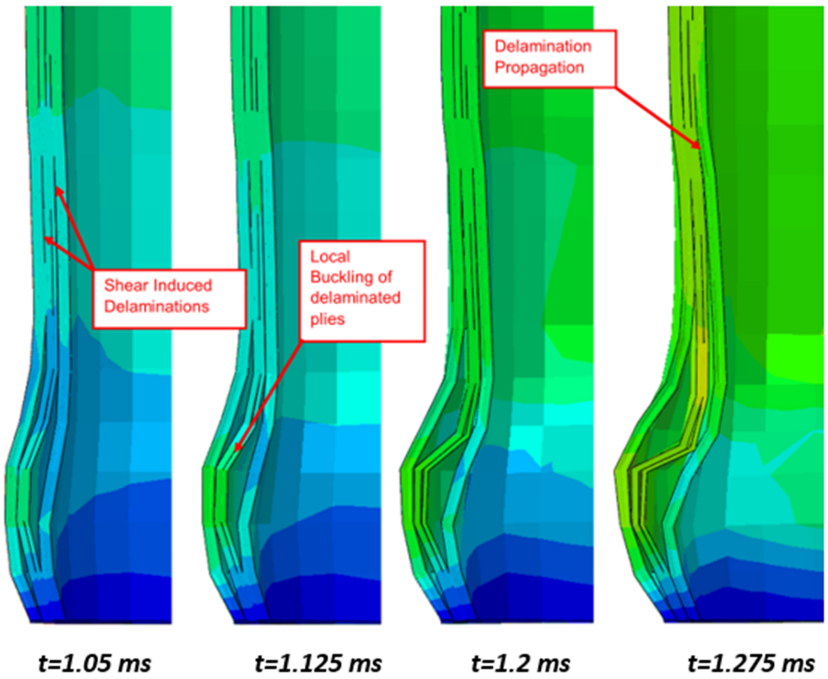

Figure 6.18: Shape and inter-laminar damage evolution (1.05 ms to 1.275 ms after impact).

The propagation of the inter-laminar damage may also be promoted by some mode I opening caused by the buckling of the plies.

Puck failure criterion

After analysing the model with Hashin failure criterion, the same was run employing the Puck criterion.The evolution and final deformed shapes can be seen on Figures 6.19 and 6.20.

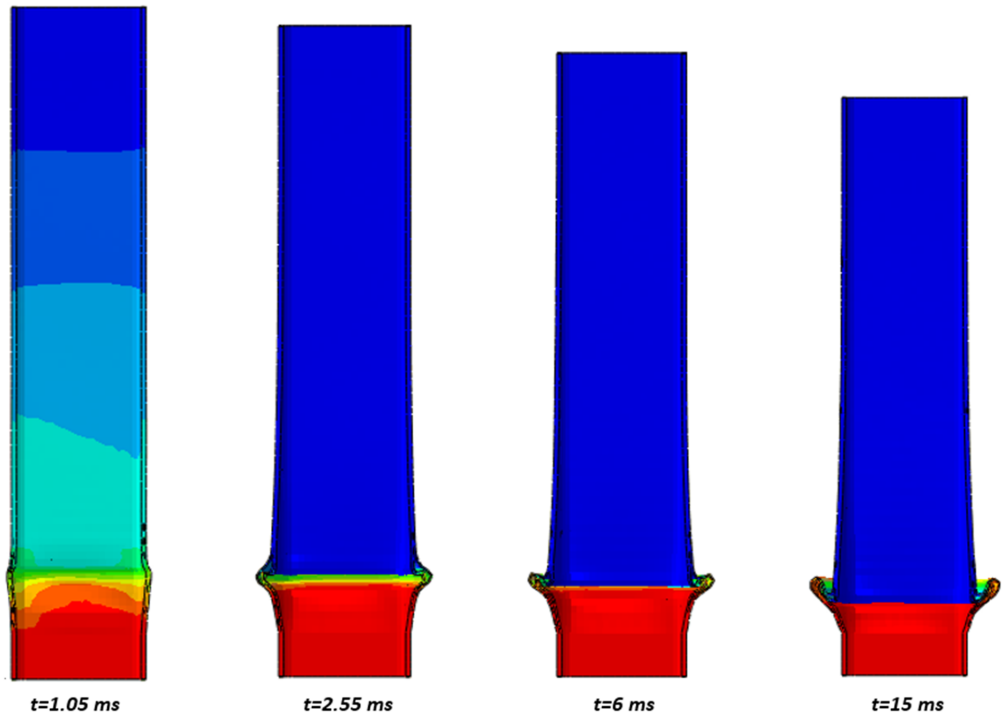

Figure 6.19: Evolution of the deformed shape, using Puck failure criterion.

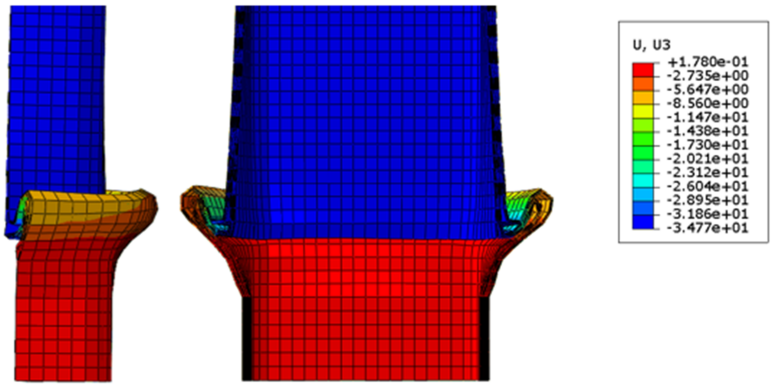

Figure 6.20: Detail of the deformed shape 15 ms after impact, using Puck failure criterion.

While investigating the sequence of events, it was noticed that some matrix compressive failure had occurred in the first 0.5 ms after impact. However, similarly to the previous premature cohesive damage, it was verified mainly inside and close to the boundary conditions, as seen on Figure 6.21, having no other damage onset occurred.

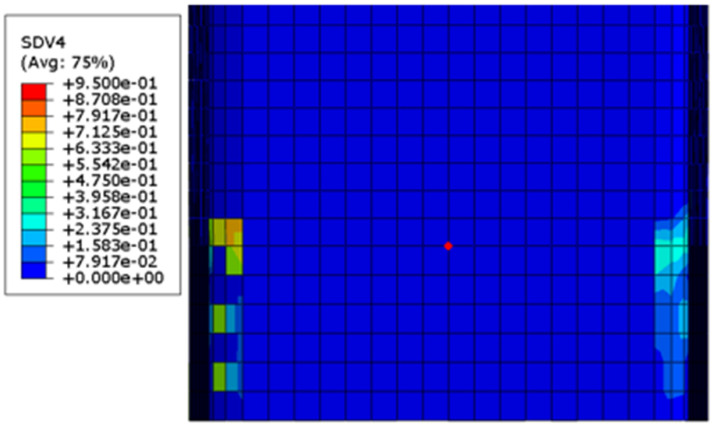

Figure 6.21: Matrix compressive damage near or inside the potting zone, where the dot represents the surface of the potting (0.525 ms after impact).

The fibre compressive failure localized in the same zones and at the same time step of the Hashin, considering the same number of outputs, which, may not be totally true considering a finer output time intervals. Nevertheless, the failure occurs near the same zones, adding to the idea of the similarities of the failure mode. At the same time, an exterior ply (all but the 0°) band of matrix compression damage, non-existent in the previous example, is formed around 20 mm above the potting, reducing locally the stiffness of the structure and promoting buckling Figure 6.22. Once again, these images were retrieved without representing the potting elements.

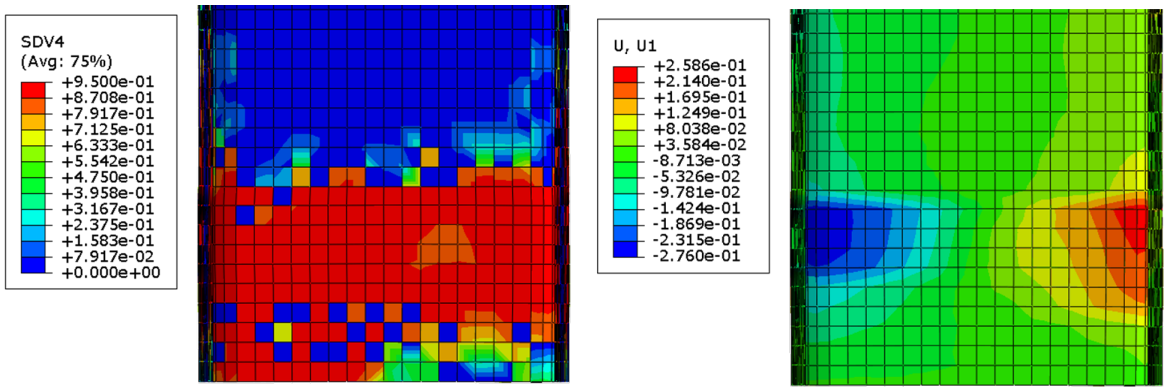

(a) (b)

Figure 6.22: (a) Band of matrix compressive damage and (b) buckling of the structure (0.6 ms after impact).

As observed, and contrarily to the previous case, this phenomenon is symmetric, having the two flanges buckled at the same place and time. Then, delaminations are further promoted due to the bending induced shear (Figure 6.23) and once the plies start folding, some traction separation occurs. After this, there is the stable 'folding' of the structure until the end of the 15 ms. It is also worth noting that in this case, the top part of the column folds on top of the bottom part, while in the previous case, employing Hashin failure criterion, the plies started folding directly on top of the potting surface.

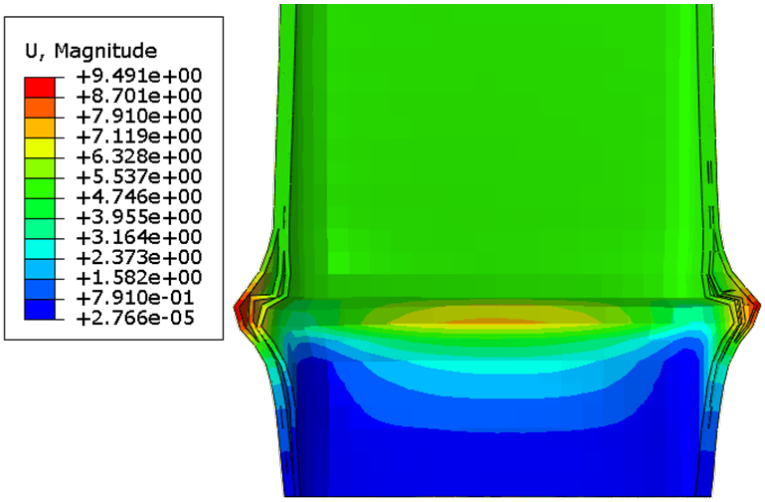

Figure 6.23: Buckling of the delaminated plies employing Puck failure criterion (1.425 ms after impact).

Strain Rate Dependent Failure Criterion

Finally, after employing both Hashin and Puck, the Strain Rate Dependent (SRD) criterion was used. The respective deformation evolution and final obtained shape are displayed on Figures 6.24 and 6.25.

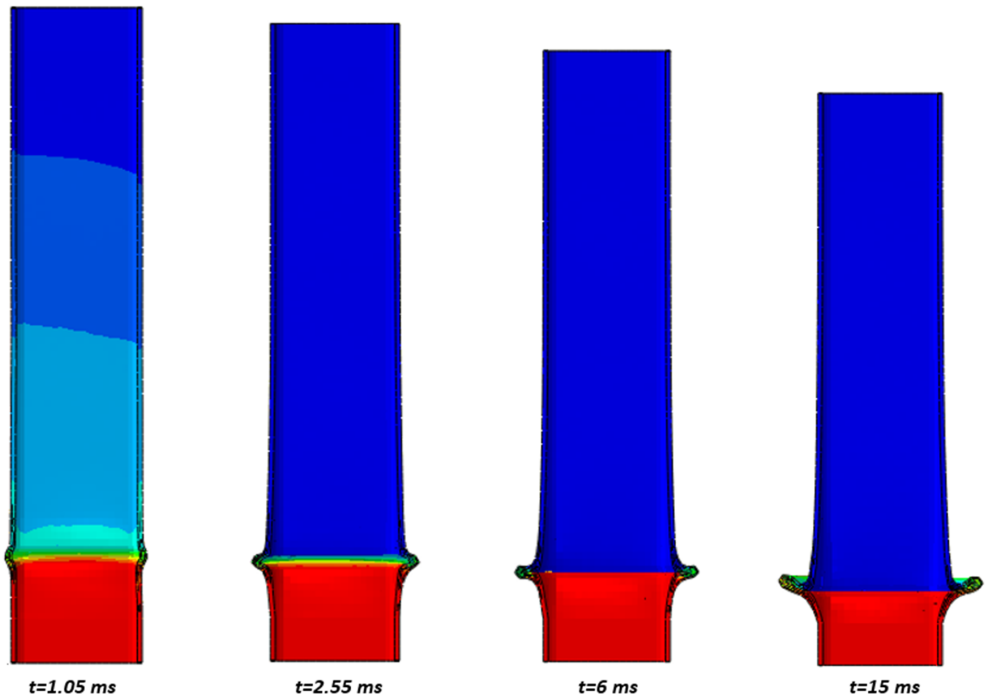

Figure 6.24: Evolution of the deformed shape, using SRD failure criterion.

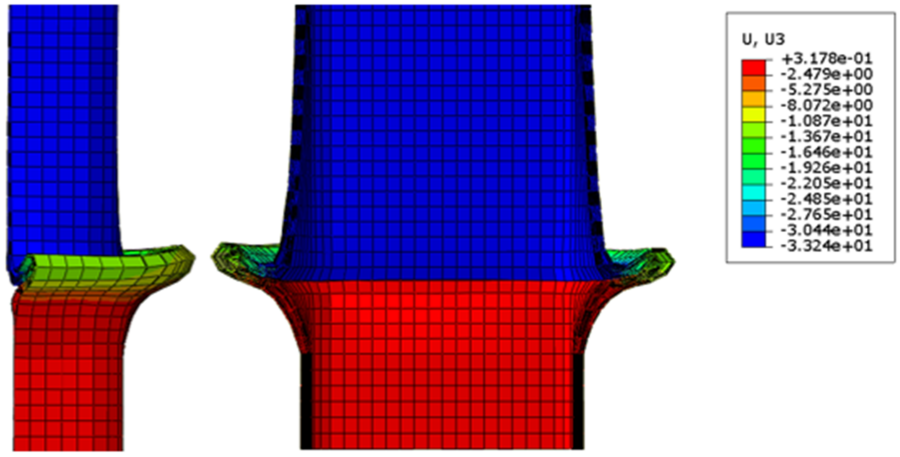

Figure 6.25: Detail of the deformed shape 15 ms after impact, using SRD failure criterion.

Similarly to Puck, the deformed shape has a symmetric configuration and buckled at approximately the same height.

The failure mode is the same as the one employing strain insensitive Hashin i.e. interior fibre compression failure followed by exterior matrix compression failure and local buckling, however, there are some differences to be addressed. Firstly, when the first failure happens, approximately at the same place, as seen in Figure 6.26, a greater number of interior plies fail. As aforementioned, mechanical properties of the brittle fibres are usually insensitive to strain, however, the effect on the matrix combined with the friction coefficient, plus the reduction of the displacement at failure, may explain this phenomenon [53]. Consequently, this localised greater loss of stiffness leads to the migration of buckling phenomenon. After the plies buckle, the same sequence of events occur, but this time, about 20 mm higher up.

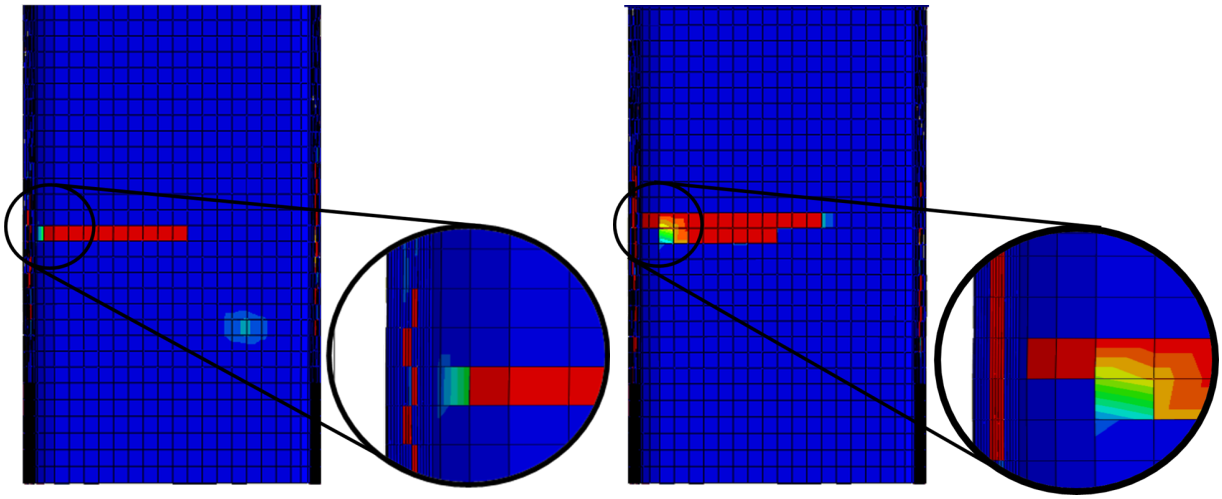

(a) (b)

Figure 6.26: Fibre compression failure, at the same simulation time, in the intermediate zone of the laminate employing (a) Hashin and (b) SRD failure criterion (0.6 ms after impact).

Relatively to the computational time of the simulations, a summarizing table (Table 6.6) is found below:

Table 6.6: Computational times of the three different models.

Criterion	CPU time
Hashin	22 h
Puck	11.5 h
SRD	12.5 h

As it can be seen, the first analysed method, i.e. employing the Hashin criterion, took substantially more time (approximately the double) to compute than the other two. This can be explained by the deformation that occurred in each model, since the stable time increments up to the point of local buckling, were approximately the same for the three models, around 1e−8 s. After that, given the higher degree of deformation, the Hashin time increments reduced approximately an order of magnitude, leading to a higher number of increments and computational time.

6.3.2.1 Acceleration an Energy absorption

Having analysed the failure modes of the three simulated models it would be useful to compare the different energy absorbing capabilities of each one of them. Initially, the full procedure will be explained for the Hashin criterion model and then, only the results for all of the models will be shown.

In order to assess the energy absorbing capability of the stanchion, the total, kinetic and internal energies, are retrieved from the simulation of the of the system and are plotted on Figure 6.27.

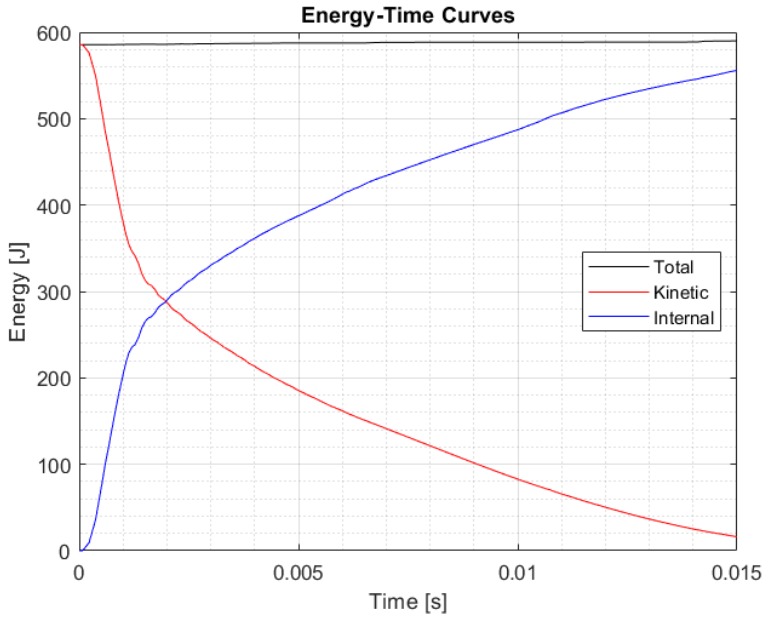

Figure 6.27: Energy-Time curves of the stanchion employing Hashin criterion.

As it can be observed, there is a steep internal energy increase in the first 1.2 ms after impact, at this point, the structure fails due to the buckling of the plies, and then, the internal energy increases in a slower logarithmic way. Up to the buckling failure, the structure absorbed approximately 236 J, nearly 50% of the initial kinetic energy. On the other hand, at the end of the 15 ms, the absorption was of 555 J which accounts for 95% of the total impact energy.

The obtained acceleration-time and force-displacement of the stanchion are also displayed on Figures 6.28 and 6.29 respectively.

On the acceleration-time plot, the previously obtained numerical results [123] and the maximum registered experimental acceleration are represented as well as a mean of comparison.

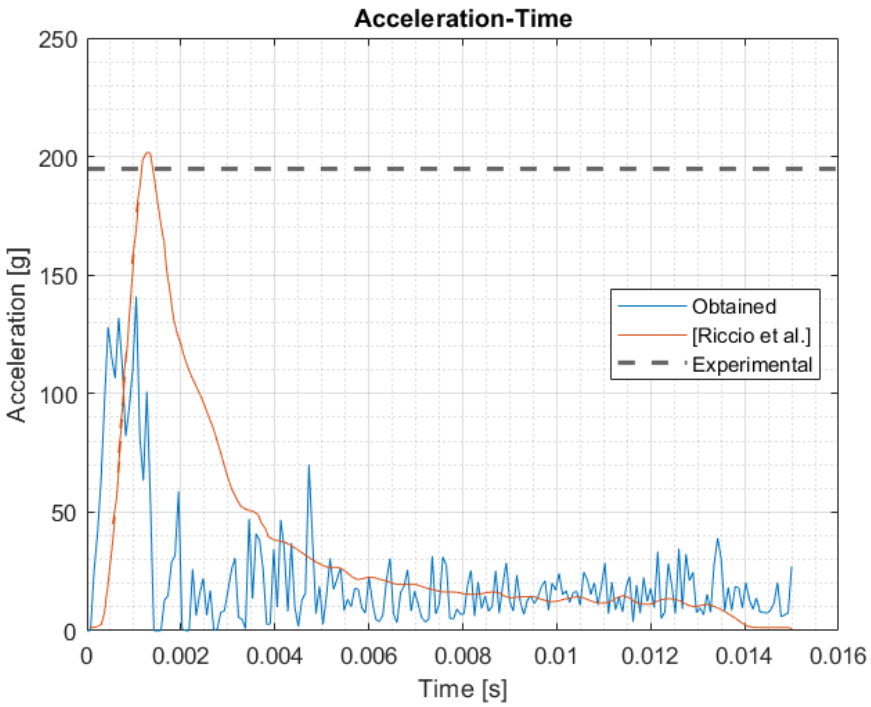

Figure 6.28: Acceleration-Time curves of the stanchion employing Hashin criterion.

Analysing the obtained acceleration, it is shown that the maximum value is around 141 g, which nearly 28% lower than the obtained experimental value. Nevertheless, it was found that this value is somewhat sensible to the number of requested outputs, specially near the peak, therefore, this result may be lower than the real one.

After the peak, there is an almost immediate decrease due to the buckling failure of the structure, leading to a stable acceleration zone around 15 g, corresponding to the progressive splaying of the plies.

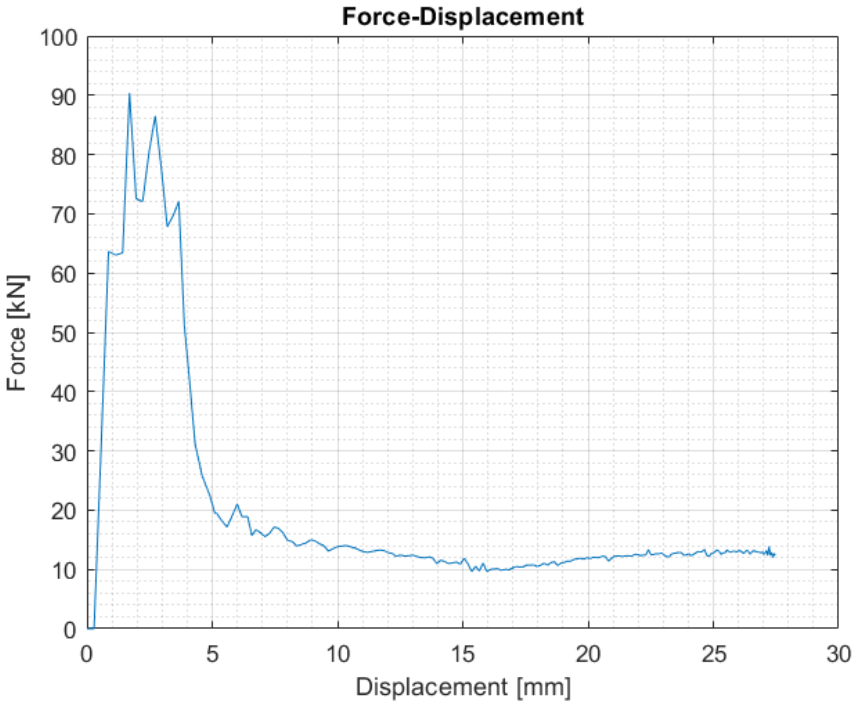

Figure 6.29: Force-Displacement curve of the stanchion employing Hashin criterion.

As expected, the force also reached a peak value changing rapidly to a stable crushing force, being the transition zone very small. The maximum obtained load was about 90.4 kN whereas the stable value averages around 12.5 kN.

Recalling the expression for the mean force of the column:

$$F_{mean} = \frac{\int F\, dl}{L} \tag{65}$$

where F is the force and L the total crushing distance, the MATLAB function 'trapz' (trapezoidal numerical integration) [122] was used. The obtained result was about 20.56 kN.

Revisiting the specific energy absorption (SEA) expression, which is also regularly used to assess the energy absorption capabilities of structures:

$$SEA = \frac{\int F\, dl}{\rho A L} = \frac{F_{mean}}{\rho A} \tag{66}$$

where A is the cross sectional area and ρ the density of the material. For this specific case, the obtained SEA was 37.69 kJ/kg.

After analysing the results employing Hashin failure criterion, the same simulation was performed with the other two criteria, keeping all of the same parameters but the VUMAT formulation. The obtained kinetic energy of the impactor was extracted for the three different models and is presented on Figure 6.30.

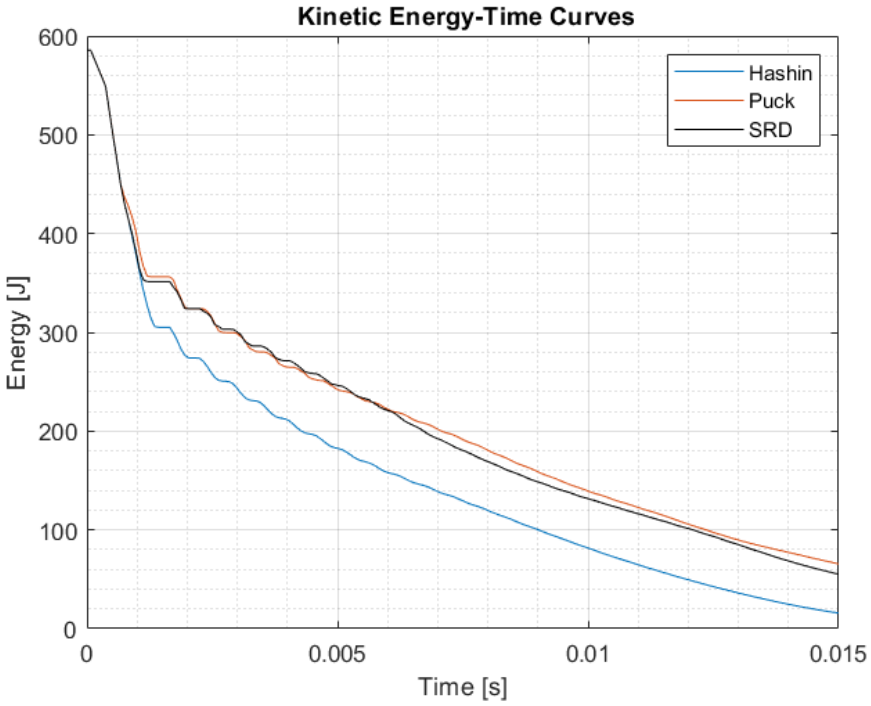

Figure 6.30: Kinetic energy of the impactor for the three different models

As it can be observed, all of the models lead to a similar kinetic energy loss until the 1 ms second mark, after that, an oscillatory transition zone takes place due to the local buckling phenomenon and respective ply folding. The offset between the curves is related to the local buckling occurrence zone, which promoted a different ply deformation behaviour, as seen on Figure 6.31. At the 1 ms instant, the total kinetic energy was of 353 J meaning that the stanchion absorbed approximately 40% of the impact energy, while at the 15 ms mark, the energy absorption was of 97.3% employing Hashin criterion and around 88.8% for the the others.

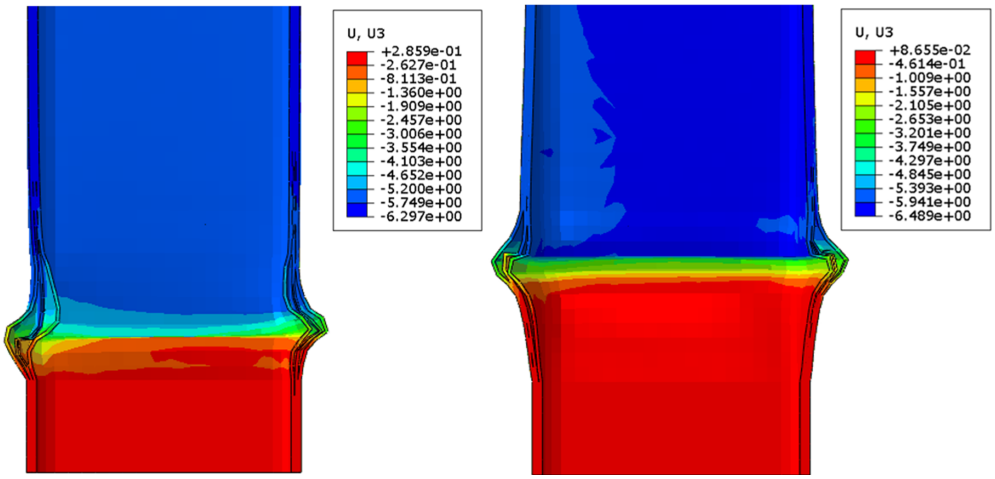

(a) (b)

Figure 6.31: Local buckling zones and shapes employing (a) Hashin and (b) Puck criterion (1.95 ms after impact).

Similarly to what was done previously, the acceleration-time and force displacement of the three models are shown on Figures 6.32 and 6.33 respectively.

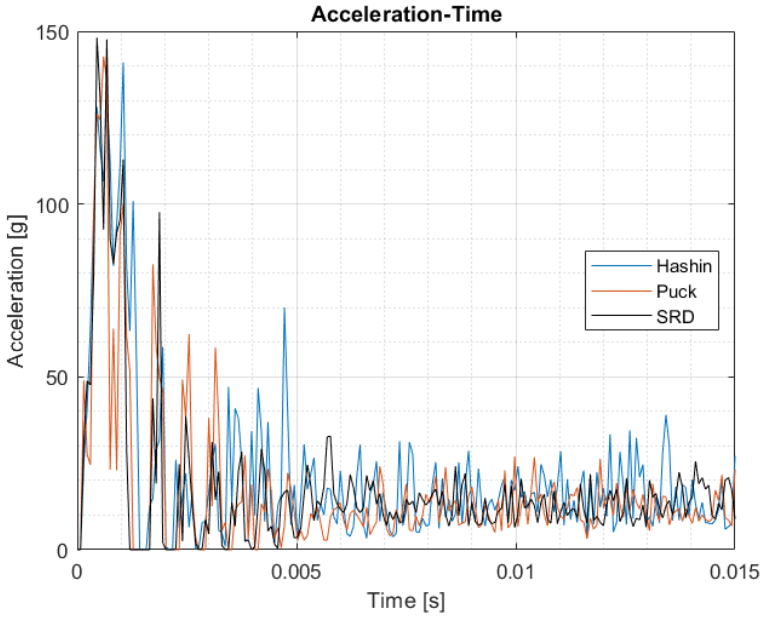

Figure 6.32: Acceleration-time curves of the three different models.

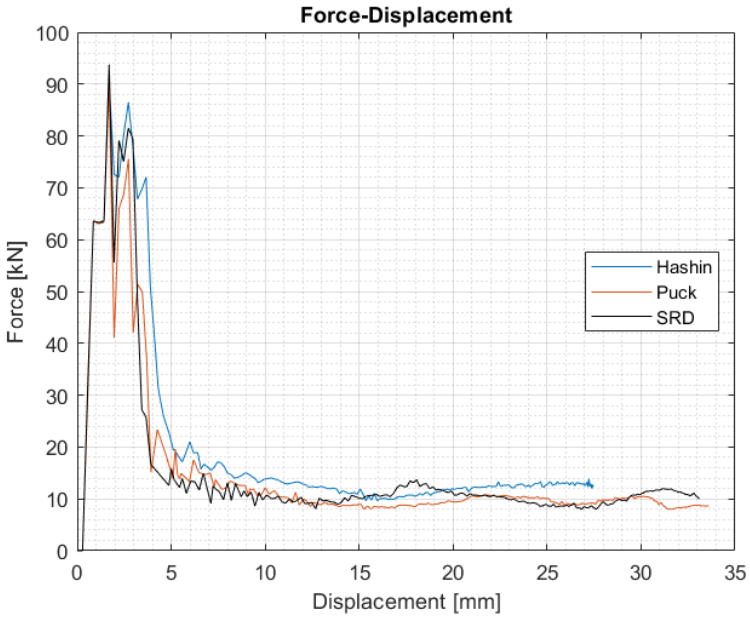

Figure 6.33: Force-displacement curves of the three different models.

From the acceleration-time relations, it is possible to obverse that all of the three criteria led to a similar evolution, having the Hashin and Puck led to a slightly larger transition zone, stabilizing around the same value. The highest peak was obtained by using the SRD failure criterion reaching a magnitude of 148 g, while with the Hashin and Puck the values were 131.9 g and 142.7 g respectively.

Similarly to the accelerations, the force-displacement curves deemed also close results. It is possible to observe that employing the Hashin failure criterion, the column crushed approximately 10 mm less than the other two, which, is caused by different local buckling zone and respective folding phenomena.

On Table 6.7, are the mean crushing forces and respective specific energy adsorptions (SEA) obtained for each case.

Table 6.7: Summary of registered reaction forces and specific energy absorption.

Criterion	F_{max}	F_{mean}	SEA
Hashin	90.39 kN	20.56 kN	37.69 kJ/kg
Puck	90.33 kN	15.09 kN	27.66 kJ/kg
SRD	93.75 kN	15.70 kN	28.77 kJ/kg

From the table it is possible to draw some conclusions. Employing the strain rate dependent criterion, a higher peak force was registered, which is due to the higher stiffness it presents in high strain rate regimes. The mean compressing force of both Puck and the SRD failure criterion are similar and lower than the Hashin's, which is related to the the place and behaviour after buckling of the structure.

6.3.2.2 Comparison with experimental results

In order to validate the numerical simulations, the results were compared to those obtained by the experimental test. The experimental results of the high energy impact of the stanchion can be seen on Figure 6.34.

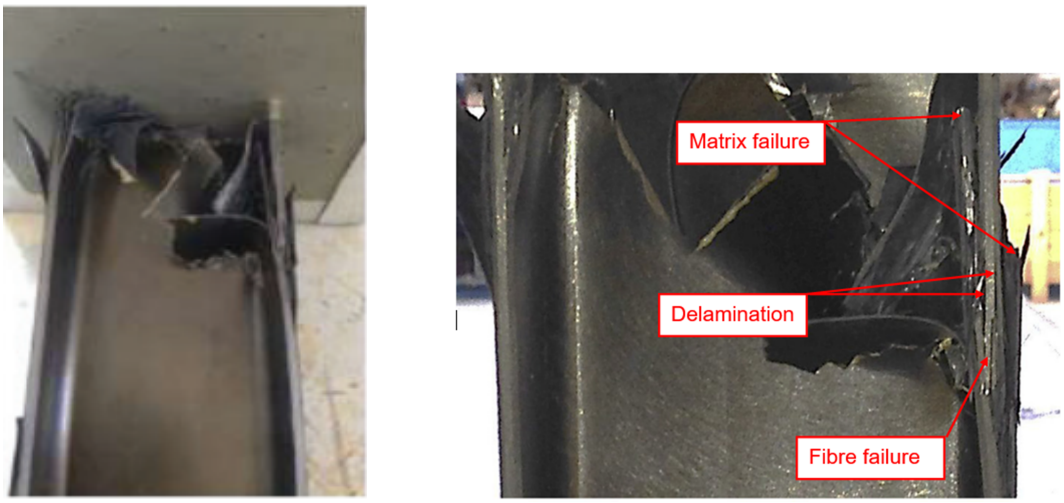

(a) (b)

Figure 6.34: Experimental damage after 585 J impact. (a) Damaged region near potting and (b) respective amplification [123, 124].

From the results it is possible to observe that the major part of the damage occurred near the potting region, particularly, fibre and matrix failure, and delaminations.

From Figure 6.34b, it is also clearly identified that the delaminations are more prominent between the 0° central set of plies and the remaining, which, is in accordance to what was obtained in the numerical results.

Regarding the mean forces and SEAs calculated in the previous section, there are no experimental data to corroborate them, serving purely as a theoretical exploration. However, given the predicted local buckling location and maximum value of acceleration, the numerical model that seems to better predict the experimental results is the Strain Rate Dependent Criterion.

In Figure 6.35 the distribution of the lateral displacement of the SRD model when the local buckling phenomenon initiated was superimposed on the experimental results, at the same distance from the potting. The damage variables through the thickness near the critical zone were also retrieved.

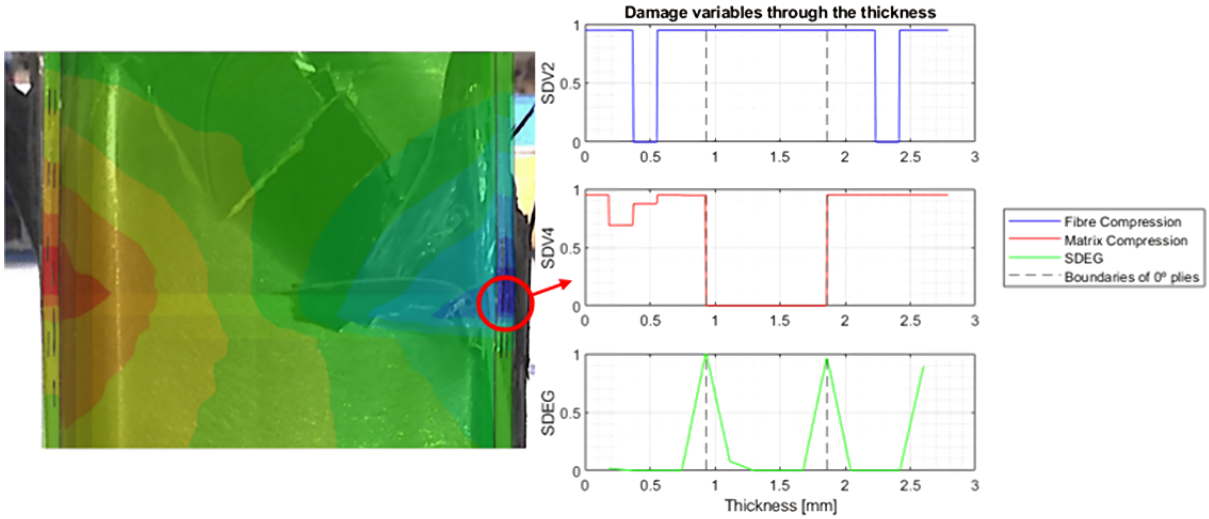

Figure 6.35: Superimposition with the experimental results of the lateral displacement of the SRD model and damage through the thickness near critical zone (7.5 ms after impact).

As it can be observed, there is an excellent agreement between the initial failure location and the experimental results. The damage through the thickness also show exactly the phenomenons evidenced on Figure 6.34b, such as the total delamination between the 0° plies and the compressive damage of the fibre and matrix on the inner and outer sections respectively.

Comparing the obtained results with this criterion to the previous developed numerical simulations in the literature [123], which employed the aforementioned different element formulation and number of elements through the thickness (please recall Figure 6.4), there was an improvement of the results, since in the previous analysis the failure was predicted to happen at the middle part of the stanchion with a wide distribution of fibre compressive damage whereas following the proposed approach in this work, the failure was predicted at same place as the experimental result, being able to identify the present failure modes in a more localised and accurate way (Figure 6.36).

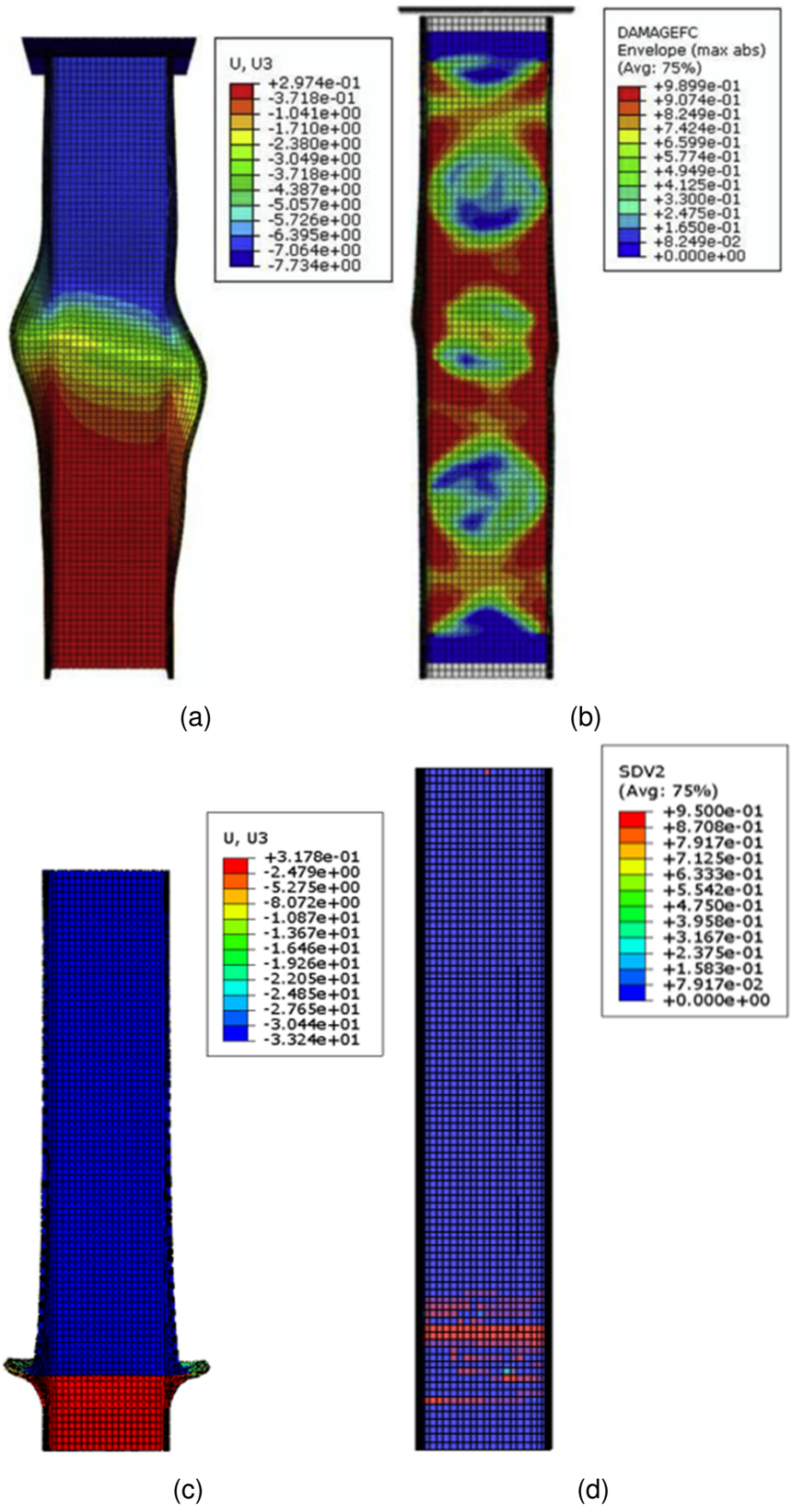

Figure 6.36: Vertical displacement at maximum compression (a) and fibre compressive damage state (b) previously obtained in [123] and vertical displacement at maximum compression (c) and undeformed fibre compressive damage state with transparency (d) obtained with SRD failure criterion.

As it can be seen, both models predicted buckling and fibre failure to happen, however, the proposed model was able to effectively capture the damage onset location. This was due to the different number of elements through the thickness and element formulation, which allow more accuracy in the stress interaction and to the implementation of the 3D failure criterion, respectively. The higher number of cohesive interfaces also allow a more refined assessment of how the stanchion behaves under crash loads.

7 Conclusions & Future Work

7.1 Conclusions

The aim of this work is to simulate a carbon fibre composite fuselage element damage behaviour using a high-fidelity model to improve the accuaracy of current crashworthiness simulation techniques. To this end, material sub-routines (VUMAT) able to employ three dimensional failure criteria with energy based gradual degradation: Hashin, modified Hashin-Puck and a Strain Rate Dependent one, were developed.

It follows that, to verify if the VUMAT development is soundly made, an one element test with simple load cases (i.e., longitudinal and transverse uniaxial compression and tension) is conducted for all of the different criteria, having the Strain Rate Dependent one to be tested for all of its three different regimes: Low, Medium and High Strain Rate. The obtained bi-linear curves are on par with what was expected and all the errors relative to the expected property values fall under the 10% threshold, numerically verifying the routines.

Then, an Open Hole Tensile (OHT) test is simulated and compared to previously obtained experimental results to validate the developed routines under more complex stress states. It is found that material routines with instantaneous failure are not adequate for predicting the failure of the part and that gradual degradation should be employed. The results employing both Hashin and Hashin+Puck are on par with the experimental results and previous literature, having the latter criterion a better performance.

Subsequently, in order to increase the degree of confidence on the created VUMAT and simulation techniques, such as the cohesive elements use, a Low Velocity Impact (LVI) on a composite plate simulation is run. Running on default configurations, the registered absorbed energy by the plate is better than the results of previous literature and is further improved by selecting the most appropriate hourglass control technique obtained by conducting a sensitivity analysis. The results of the other criteria predict better the behaviour than the literature but can be also further improved with appropriate self-dedicated parameter study and sensitivity analysis.

After validating the method with less complex scenarios, the final test case, representing the composite stanchion model, is created and subject to different analysis. Initially, a quasi static followed by a low energy impact are simulated to verify both the stiffness and the overall behavior of the structure under dynamic events. An excellent agreement with the experimental and analytical data was found. Then, a high energy impact is conducted for the three developed criteria and it was observed that the stanchion failure is driven by fibre compression followed by delamination and local buckling. The results were compared to the experimental ones, and a better damage and behaviour prediction was obtained relatively to previous numerical analysis available in the literature.

Overall, the simulation methodology proposed on this work, is generally able to obtain better results than previous developed works , and predicts correctly the failure of a fuselage element crash, which is not obtained in previous works on the same model using a simplified approach. This way, it is concluded that this work provided an effective simulation strategy for getting higher fidelity results.

7.2 Future Work

Despite the fact that better predictions could be achieved employing the proposed methodology in this work, further improvements and additional research can be done. Some suggestions of future work are presented below:

- A low but relevant fibre compression fracture toughness relative error was obtained in the patch test. Given that the failure of the stanchion was mainly related to the fibre compression failure, further investigation should be done to assess if employing any other method, (such as Puck) for fibre compression would deem similar results.

- In the development of the strain rate VUMAT, it was assumed that the strain rate effect on the in-plane transversal stiffness was the same as the lateral one. This is a simplification which consequences are not fully known, therefore, the development of a tri-axial strain rate dependent failure criterion and their employment in the same numerical analysis presented in this work, would allow to assess its validity.

- The computational time of the stanchion numerical simulations of the literature was not disclosed, however, given the simplicity of the model, it can be assumed that they were significantly shorter than the ones required in this work. The use of the proposed methodology in conjunction with other simulation techniques such as solid/shell coupling techniques should be studied for its implementation with lower computational costs.

- In this work, only a vertical loaded composite stanchion was numerically simulated, however, the sub-cargo structure has other different features such as the cargo cross beam and the fuselage skin and frames. As a future work, it would be interesting to apply this proposed methodology on a bigger structure, including those same features and the respective metallic fasteners, in order to assess its impact behavior.

Bibliography

1. Boeing. *53rd Statistical Summary of Commercial Jet Airplane Accidents (1959-2021)* (2022). https://www.boeing.com/resources/boeingdotcom/company/about_bca/pdf/statsum.pdf.
2. IATA. *Global Outlook for Air Transport - June* (2022). https://www.iata.org/en/iata-repository/publications/economic-reports/airline-industry-economic-performance---june-2022---report/.
3. EASA. *Annual safety review 2022* (2022).
4. EASA. *Certification Specifications and Acceptable Means of Compliance for Large Aeroplanes (CS-25)* (2021).
5. FAA. *14 CFR Part 25 Airworthiness Standards: Transport Category Airplanes* (2023).
6. FAA. *AC 20-107B - Composite Aircraft Structure* (2010).
7. FAA. *Special Conditions No. 25-537-SC* (2014).
8. Du Bois, P, Chou, C., Fileta, B. & et al. *Vehicle crashworthiness and occupant protection* (Southfield, Michigan, 2021).
9. Christensen, J., Wilson, A., Bastien, C. & Kayvantash, K. Efficient crash structure design for road traffic accidents of tomorrow. *International Journal of Crashworthiness* **0,** 1–20. eprint: https://doi.org/10.1080/13588265.2022.2114577. https://doi.org/10.1080/13588265.2022.2114577 (2022).
10. Noorsumar, G., Rogovchenko, S., Robbersmyr, K. G. & Vysochinskiy, D. Mathematical models for assessment of vehicle crashworthiness: a review. *International Journal of Crashworthiness* **27,** 1545–1559. eprint: https://doi.org/10.1080/13588265.2021.1929760. https://doi.org/10.1080/13588265.2021.1929760 (2022).
11. Mou, H., Xie, J. & Feng, Z. Research status and future development of crashworthiness of civil aircraft fuselage structures: An overview. *Progress in Aerospace Sciences* **119,** 100644. ISSN: 0376-0421. https://www.sciencedirect.com/science/article/pii/S0376042120300567 (2020).
12. Di Palma, L. *et al.* Vertical Drop Test of Composite Fuselage Section of a Regional Aircraft. *AIAA Journal* **58,** 474–487. eprint: https://doi.org/10.2514/1.J058517. https://doi.org/10.2514/1.J058517 (2020).
13. Katnam, K., Da Silva, L. & Young, T. Bonded repair of composite aircraft structures: A review of scientific challenges and opportunities. *Progress in Aerospace Sciences* **61,** 26–42. ISSN: 0376-0421. https://www.sciencedirect.com/science/article/pii/S0376042113000183 (2013).
14. Norkhairunnisa, M., Chai Hua, T., Sapuan, S. M. & Ilyas, R. A. in *Advanced Composites in Aerospace Engineering Applications* (eds Mazlan, N., Sapuan, S. & Ilyas, R.) 367–385 (Springer International Publishing, Cham, 2022). ISBN: 978-3-030-88192-4. https://doi.org/10.1007/978-3-030-88192-4_18.
15. Marsh, G. Airbus A350 XWB update. *Reinforced Plastics* **54,** 20–24. ISSN: 0034-3617. https://www.sciencedirect.com/science/article/pii/S0034361710702125 (2010).
16. Riccio, A., Saputo, S., Sellitto, A., Di Caprio, F. & Di Palma, L. A numerical-experimental assessment on a composite fuselage barrel vertical drop test:

Induced damage onset and evolution. *Composite Structures* **248,** 112519. ISSN: 0263-8223. https://www.sciencedirect.com/science/article/pii/S0263822320314847 (2020).

17. Heimbs, S., Hoffmann, M., Waimer, M., Schmeer, S. & Blaurock, J. Dynamic testing and modelling of composite fuselage frames and fasteners for aircraft crash simulations. *International Journal of Crashworthiness* **18,** 406–422. eprint: https://doi.org/10.1080/13588265.2013.801294. https://doi.org/10.1080/13588265.2013.801294 (2013).
18. Middendorf, P. & Heimbs, S. Crash Simulation of Composite Structures. *Composite Materials* **2,** 18–22 (Mar. 2007).
19. Ren, Y. & Xiang, J. Energy absorption structures design of civil aircraft to improve crashworthiness. *Aeronautical Journal* **118,** 383–398 (Apr. 2014).
20. Luca, A. D. & Caputo, F. A review on analytical failure criteria for composite materials. *AIMS Materials Science* **4,** 1165–1185. ISSN: 2372-0484. https://www.aimspress.com/article/doi/10.3934/matersci.2017.5.1165 (2017).
21. Jäger, S., Pickett, A. & Middendorf, P. A Discrete Model for Simulation of Composites Plate Impact Including Coupled Intra- and Inter-ply Failure. *Applied Composite Materials* **23** (July 2015).
22. Shi, Y., Pinna, C. & Soutis, C. Modelling impact damage in composite laminates: A simulation of intra- and inter-laminar cracking. *Composite Structures* **114,** 10–19. ISSN: 0263-8223. https://www.sciencedirect.com/science/article/pii/S026382231400155X (2014).
23. Lopes, C. *et al.* Low-velocity impact damage on dispersed stacking sequence laminates. Part I: Experiments. *Composites Science and Technology* **69,** 926–936. ISSN: 0266-3538. https://www.sciencedirect.com/science/article/pii/S026635380900058X (2009).
24. FAA. *14 CFR Part 11 General Rulemaking Procedures* (2000).
25. Xiaochuan, L., Xiasheng, S., Jun, G. & Rangke, M. *Crash simulation and drop test of civil airplane fuselage section* in. **4** (Dec. 2013), 3017–3021. ISBN: 978-1-4799-2565-0.
26. Crashworthiness, T. A. & Group, D. W. *Transport Airplane Crashworthiness and Ditching Working Group Recommendation Report* (2018).
27. Riccio, A. *et al.* An Insight on the Crashworthiness Behavior of a Full-Scale Composite Fuselage Section at Different Impact Angles. *Aerospace* **6.** ISSN: 2226-4310. https://www.mdpi.com/2226-4310/6/6/72 (2019).
28. Waimer, M. *Development of a Kinematics Model for the Assessment of Global Crash Scenarios of a Composite Transport Aircraft Fuselage* PhD thesis (Jan. 2013).
29. Williams, M. S. *Vertical drop test of a transport fuselage section located forward of the wing* (Langley Research Center, 1983).
30. Fasanella, E. L. & Alfaro-Bou, E. *Vertical drop test of a transport fuselage section located aft of the wing* tech. rep. (1986).
31. Williams, M. S. *Vertical drop test of a transport fuselage center section including the wheel wells* (Langley Research Center, 1983).

32. Jackson, K. E., Boitnott, R. L., Fasanella, E. L., Jones, L. E. & Lyle, K. H. *A History of Full-Scale Aircraft and Rotorcraft Crash Testing and Simulation at NASA Langley Research Center* in (2004).
33. Malherbe, B., Langrand, B., Charles, J.-L. & Sobry, J.-F. *Improvement of crash models of large aeronautical structures* in (Aug. 2000).
34. Delsart, D., Joly, D. & Mahé, M. *Evaluation of finite element modelling methodologies for the design of crashworthy composite commercial aircraft fuselage* in (2004).
35. Jackson, K. & Fasanella, E. Crash Simulation of Vertical Drop Tests of Two Boeing 737 Fuselage Sections (Jan. 2002).
36. Minegishi, M. *et al.* Vertical Drop Test of a YS-11 Fuselage Section. *Japan Society of Aeronautical Space Sciences* **51,** 354–363 (Jan. 2003).
37. Jackson, K. E., Littell, J. D., Annett, M. S. & Haskin, I. M. *Finite element simulations of two vertical drop tests of F-28 fuselage sections* tech. rep. (2018).
38. Abramowitz, A., of Aviation Research, U. S. F. A. A. O., Development & (U.S.), W. J. H. T. C. *Vertical Drop Test of an ATR 42-300 Airplane* (U.S. Department of Transportation, Federal Aviation Administration, Office of Aviation Research and Development, 2006).
39. Liu, X., Guo, J., Bai, C., Sun, X. & Mou, R. Drop test and crash simulation of a civil airplane fuselage section. *Chinese Journal of Aeronautics* **28,** 447–456. ISSN: 1000-9361. https://www.sciencedirect.com/science/article/pii/S1000936115000230 (2015).
40. Littell, J. D. *A Summary of Results from Two Full-Scale Fokker F28 Fuselage Section Drop Tests* in (2018).
41. Jackson, K. E. & Putnam, J. B. *Simulation of a Full-Scale Crash Test of a Fokker F28 Fellowship Aircraft* in (2020).
42. Gomez, L. *Crashworthiness - Certification by Analysis* in *JAMS 2021 Technical Review* (Wichita State University, 2021).
43. Cronkhite, J. D., Haas, T. J., Berry, V. L. & Winter, R. *Investigation of the Crash-Impact Characteristics of Advanced Airframe Structures.* in (1979).
44. Perfetto, D. *et al.* Drop test simulation and validation of a full composite fuselage section of a regional aircraft. *Procedia Structural Integrity* **12.** AIAS 2018 international conference on stress analysis, 380–391. ISSN: 2452-3216. https://www.sciencedirect.com/science/article/pii/S2452321618301823 (2018).
45. Chetan, Gopalaiah, N. & Girish, K. FATIGUE LIFE ESTIMATION OF REAR FUSELAGE STRUCTURE OF AN AIRCRAFT. *International Journal of Research in Engineering and Technology* **4,** 347–354 (July 2015).
46. Christian, H. *Advanced Lattice Structures for Composite Airframes* https://cordis.europa.eu/docs/results/265881/final1-2014-03-06-alasca-final-report-submitted.pdf.
47. Waimer, M., Feser, T., Schatrow, P. & Schueler, D. Crash concepts for CFRP transport aircraft – comparison of the traditional bend frame concept versus the developments in a tension absorbers concept. *International Journal of Crashworthiness* **23,** 193–218. eprint: https://doi.org/10.1080/13588265.2017.1341279. https://doi.org/10.1080/13588265.2017.1341279 (2018).

48. Guida, M., Marulo, F. & Abrate, S. Advances in crash dynamics for aircraft safety. *Progress in Aerospace Sciences* **98,** 106–123. ISSN: 0376-0421. https://www.sciencedirect.com/science/article/pii/S0376042117302208 (2018).
49. Zhenyu, F. *et al.* The failure mechanism and energy-absorbing characteristics of composite thin-walled C-channels subject to low-speed axial compression. *Journal of Composite Materials* **53,** 2249–2259. eprint: https://doi.org/10.1177/0021998319826337. https://doi.org/10.1177/0021998319826337 (2019).
50. Ren, Y. & Xiang, J. *Influences of Geometrical Factors on the Crashworthiness of Open Shells* in (Apr. 2010). ISBN: 978-1-60086-961-7.
51. Feraboli, P., Wade, B., Deleo, F. & Rassaian, M. Crush energy absorption of composite channel section specimens. *Composites Part A: Applied Science and Manufacturing* **40.** Special Issue: 15th French National Conference on Composites - JNC15, 1248–1256. ISSN: 1359-835X. https://www.sciencedirect.com/science/article/pii/S1359835X09001675 (2009).
52. Bolukbasi, A. & Laananen, D. Energy absorption in composite stiffeners. *Composites* **26,** 291–301. ISSN: 0010-4361. https://www.sciencedirect.com/science/article/pii/0010436195936727 (1995).
53. Mamalis, A. G., Manolakos, D., Demosthenous, G. & Ioannidis, M. *Crashworthiness of composite thin-walled structures* (CRC Press, 2017).
54. Farley, G. L. *Energy-absorption capability of composite tubes and beams* PhD thesis (Virginia Polytechnic Institute and State University, 1989).
55. Hull, D. A unified approach to progressive crushing of fibre-reinforced composite tubes. *Composites Science and Technology* **40,** 377–421. ISSN: 0266-3538. https://www.sciencedirect.com/science/article/pii/026635389190031J (1991).
56. Ostler, D., Blessing, E., Perl, M. & Adams, D. *Crashworthiness - Certification by Analysis* in *JAMS 2019 Technical Review* (The University of Utah, 2019).
57. Bussadori, B., Schuffenhauer, K. & Scattina, A. Modelling of CFRP crushing structures in explicit crash analysis. *Composites Part B: Engineering* **60,** 725–735. ISSN: 1359-8368. https://www.sciencedirect.com/science/article/pii/S1359836814000304 (2014).
58. Deletombe, E., Delsart, D, Fabis, J., Langrand, B. & Ortiz, R. *Recent developments in modelling and experimentation fields with respect to crashworthiness and impact on aerospace structures* in (Aug. 2004).
59. DC, D. O. D. W. *Composite Materials Handbook. Volume 1. Polymer Matrix Composites Guidelines for Characterization of Structural Materials* (2002).
60. DC, D. O. D. W. *Composite Materials Handbook. Volume 3. Polymer Matrix Composites Materials Usage, Design, and Analysis* (2002).
61. Rouse, M., Jegley, D., McGowan, D., Bush, H. & Waters, W. in *46th AIAA/ASME/ASCE/AHS/ASC Structures, Structural Dynamics and Materials Conference* (). eprint: https://arc.aiaa.org/doi/pdf/10.2514/6.2005-1874. https://arc.aiaa.org/doi/abs/10.2514/6.2005-1874.
62. Cumbo, R., Baroni, A., Ricciardi, A. & Corvaglia, S. Design allowables of composite laminates: A review. *Journal of Composite Materials* **56,** 3617–3634. eprint:

https://doi.org/10.1177/00219983221117216. https://doi.org/10.1177/00219983221117216 (2022).

63. Vallmajó, O. *et al.* Virtual calculation of the B-value allowables of notched composite laminates. *Composite Structures* **212,** 11–21. ISSN: 0263-8223. https://www.sciencedirect.com/science/article/pii/S0263822318345318 (2019).
64. Riccio, A., Saputo, S., Sellitto, A. & Di Caprio, F. On the crashworthiness behaviour of a composite fuselage Sub-floor component. *Composite Structures* **234,** 111662. ISSN: 0263-8223. https://www.sciencedirect.com/science/article/pii/S0263822319338358 (2020).
65. Choi, B.-L. & Choi, B.-H. Numerical method for optimizing design variables of carbon-fiber-reinforced epoxy composite coil springs. *Composites Part B: Engineering* **82,** 42–49. ISSN: 1359-8368. https://www.sciencedirect.com/science/article/pii/S1359836815004333 (2015).
66. Egan, B., McCarthy, C., McCarthy, M., Gray, P. & O'Higgins, R. Static and high-rate loading of single and multi-bolt carbon–epoxy aircraft fuselage joints. *Composites Part A: Applied Science and Manufacturing* **53,** 97–108. ISSN: 1359-835X. https://www.sciencedirect.com/science/article/pii/S1359835X13001401 (2013).
67. Borba, N., Körbelin, J., Fiedler, B., dos Santos, J. & Amancio-Filho, S. Low-velocity impact response of friction riveted joints for aircraft application. *Materials Design* **186,** 108369. ISSN: 0264-1275. https://www.sciencedirect.com/science/article/pii/S026412751930807X (2020).
68. Li, W. *et al.* 3D-printed thermoplastic composite fasteners for single lap joint reinforcement. *Composite Structures* **282,** 115085. ISSN: 0263-8223. https://www.sciencedirect.com/science/article/pii/S0263822321015051 (2022).
69. Perez, J., Johnson, E. & Boitnott, R. in *39th AIAA/ASME/ASCE/AHS/ASC Structures, Structural Dynamics, and Materials Conference and Exhibit* (). eprint: https://arc.aiaa.org/doi/pdf/10.2514/6.1998-1703. https://arc.aiaa.org/doi/abs/10.2514/6.1998-1703.
70. Hachenberg, D, Lavinge, V & Mahe, M. *Crashworthiness of fuselage hybrid structure* in *FAA. 8th Triennial International Aircraft Fire and Cabin Safety Research Conference. Washington DC: FAA* (2016), 1–16.
71. Sokolinsky, V. S., Indermuehle, K. C. & Hurtado, J. A. Numerical simulation of the crushing process of a corrugated composite plate. *Composites Part A: Applied Science and Manufacturing* **42,** 1119–1126. ISSN: 1359-835X. https://www.sciencedirect.com/science/article/pii/S1359835X1100131X (2011).
72. Forghani, A., Shahbazi, M., Zobeiry, N., Poursartip, A. & Vaziri, R. in *Numerical Modelling of Failure in Advanced Composite Materials* (eds Camanho, P. P. & Hallett, S. R.) 151–173 (Woodhead Publishing, 2015). ISBN: 978-0-08-100332-9. https://www.sciencedirect.com/science/article/pii/B9780081003329000062.
73. Oterkus, E., Diyaroglu, C., De Meo, D. & Allegri, G. in *Marine Applications of Advanced Fibre-Reinforced Composites* (eds Graham-Jones, J. & Summerscales, J.) 79–102 (Woodhead Publishing, 2016). ISBN: 978-1-78242-250-

1. https://www.sciencedirect.com/science/article/pii/B9781782422501000041.
74. Filippatos, A., Langkamp, A. & Gude, M. Influence of Gradual Damage on the Structural Dynamic Behaviour of Composite Rotors: Simulation Assessment. *Materials* **11.** ISSN: 1996-1944. https://www.mdpi.com/1996-1944/11/12/2453 (2018).
75. Ribeiro, M. L., Tita, V. & Vandepitte, D. A new damage model for composite laminates. *Composite Structures* **94,** 635–642. ISSN: 0263-8223. https://www.sciencedirect.com/science/article/pii/S0263822311003321 (2012).
76. Tsai, S. W. & Wu, E. M. A General Theory of Strength for Anisotropic Materials. *Journal of Composite Materials* **5,** 58–80. eprint: https://doi.org/10.1177/002199837100500106. https://doi.org/10.1177/002199837100500106 (1971).
77. Tsai, S. W. *Strength Characteristics of Composite Materials.* tech. rep. (Philco Corp Newport Beach CA, 1965).
78. Hoffman, O. The Brittle Strength of Orthotropic Materials. *Journal of Composite Materials* **1,** 200–206. eprint: https://doi.org/10.1177/002199836700100210. https://doi.org/10.1177/002199836700100210 (1967).
79. Puck, A. & Schürmann, H. Failure analysis of FRP laminates by means of physically based phenomenological models. *Composites Science and Technology* **62,** 1633–1662. ISSN: 0266-3538. https://www.sciencedirect.com/science/article/pii/S0266353801002081 (2002).
80. Yamada, S. & Sun, C. Analysis of Laminate Strength and Its Distribution. *Journal of Composite Materials* **12,** 275–284. eprint: https://doi.org/10.1177/002199837801200305. https://doi.org/10.1177/002199837801200305 (1978).
81. Pinho, S. T., Dávila, C. G., Camanho, P. P., Iannucci, L. & Robinson, P. Failure Models and Criteria for FRP Under In-Plane or Three-Dimensional Stress States Including Shear Non-Linearity (Mar. 2005).
82. Pinho, S., Darvizeh, R, Robinson, P, Schuecker, C & Camanho, P. Material and structural response of polymer-matrix fibre-reinforced composites. *Journal of Composite Materials* **46,** 2313–2341. eprint: https://doi.org/10.1177/0021998312454478. https://doi.org/10.1177/0021998312454478 (2012).
83. Camanho, P., Arteiro, A., Melro, A., Catalanotti, G. & Vogler, M. Three-dimensional invariant-based failure criteria for fibre-reinforced composites. *International Journal of Solids and Structures* **55.** Special Issue Computational and Experimental Mechanics of Advanced Materials A workshop held at King Abdullah University of Science and Technology Jeddah, Kingdom of Saudi Arabia July 1-3, 2013, 92–107. ISSN: 0020-7683. https://www.sciencedirect.com/science/article/pii/S0020768314001449 (2015).
84. Yan, L., Wang, X., Wu, H. & Liu, P. Damage and failure mechanisms of biaxial weft-knitted reinforced composites via meso-scale finite element modeling. *Journal of Industrial Textiles* **51,** 1592S–1611S. eprint: https://doi.

org/10.1177/15280837211044167. https://doi.org/10.1177/15280837211044167 (2022).

85. Hashin, Z. Failure Criteria for Unidirectional Fiber Composites. *Journal of Applied Mechanics* **47,** 329–334. ISSN: 0021-8936. eprint: https://asmedigitalcollection.asme.org/appliedmechanics/article-pdf/47/2/329/5878334/329_1.pdf. https://doi.org/10.1115/1.3153664 (June 1980).
86. Zhou, J., Wen, P. & Wang, S. Finite element analysis of a modified progressive damage model for composite laminates under low-velocity impact. *Composite Structures* **225,** 111113. ISSN: 0263-8223. https://www.sciencedirect.com/science/article/pii/S0263822319303976 (2019).
87. Gong, Y. *et al.* A Reliable Fracture Angle Determination Algorithm for Extended Puck's 3D Inter-Fiber Failure Criterion for Unidirectional Composites. *Materials* **14.** ISSN: 1996-1944. https://www.mdpi.com/1996-1944/14/21/6325 (2021).
88. Schirmaier, F., Weiland, J., Kärger, L. & Henning, F. A new efficient and reliable algorithm to determine the fracture angle for Puck's 3D matrix failure criterion for UD composites. *Composites Science and Technology* **100,** 19–25. ISSN: 0266-3538. https://www.sciencedirect.com/science/article/pii/S0266353814001882 (2014).
89. Rezasefat, M., Badel Torres, D., Gonzalez-Jimenez, A., Giglio, M. & Manes, A. A fast fracture plane orientation search algorithm for Puck's 3D IFF criterion for UD composites. *Materials Today Communications* **28,** 102700. ISSN: 2352-4928. https://www.sciencedirect.com/science/article/pii/S2352492821006929 (2021).
90. Koerber, H. *et al.* Experimental characterization and constitutive modeling of the non-linear stress–strain behavior of unidirectional carbon–epoxy under high strain rate loading. *Advanced modeling and simulation in engineering sciences* **5.** http://hdl.handle.net/2117/367696 (2018).
91. Kwon, Y. & Panick, C. Strain rate dependent failure criteria for fibrous composites using multiscale approach. *Multiscale and Multidisciplinary Modeling, Experiments and Design* **3** (Mar. 2020).
92. Raimondo, L., Iannucci, L., Robinson, P. & Curtis, P. Modelling of strain rate effects on matrix dominated elastic and failure properties of unidirectional fibre-reinforced polymer–matrix composites. *Composites Science and Technology* **72,** 819–827. ISSN: 0266-3538. https://www.sciencedirect.com/science/article/pii/S026635381200070X (2012).
93. Daniel, I., Werner, B. & Fenner, J. Strain-rate-dependent failure criteria for composites. *Composites Science and Technology* **71,** 357–364. ISSN: 0266-3538. https://www.sciencedirect.com/science/article/pii/S0266353810004677 (2011).
94. Millen, S., Murphy, A., Catalanotti, G. & Abdelal, G. Coupled Thermal-Mechanical Progressive Damage Model with Strain and Heating Rate Effects for Lightning Strike Damage Assessment. *Applied Composite Materials* **26** (Dec. 2019).
95. Support, A. *Composites Pin Board - Composite Coordinate Systems* https://www.autodesk.com/support/technical/article/caas/tsarticles/ts/2jDyibvNmozlbtCYAu9r1N.html (2023).

96. Koerber, H. & Camanho, P. High strain rate characterisation of unidirectional carbon–epoxy IM7-8552 in longitudinal compression. *Composites Part A: Applied Science and Manufacturing* **42,** 462–470. ISSN: 1359-835X. https://www.sciencedirect.com/science/article/pii/S1359835X11000054 (2011).
97. Singh, H., Namala, K. K. & Mahajan, P. A damage evolution study of E-glass/epoxy composite under low velocity impact. *Composites Part B: Engineering* **76,** 235–248. ISSN: 1359-8368. https://www.sciencedirect.com/science/article/pii/S135983681500102X (2015).
98. Riccio, A., Di Costanzo, C., Di Gennaro, P., Sellitto, A. & Raimondo, A. Intra-laminar progressive failure analysis of composite laminates with a large notch damage. *Engineering Failure Analysis* **73,** 97–112. ISSN: 1350-6307. https://www.sciencedirect.com/science/article/pii/S1350630716302898 (2017).
99. Riccio, A., Saputo, S., Raimondo, A. & Sellitto, A. in *Dynamic Response and Failure of Composite Materials and Structures* (eds Lopresto, V., Langella, A. & Abrate, S.) 129–158 (Woodhead Publishing, 2017). ISBN: 978-0-08-100887-4. https://www.sciencedirect.com/science/article/pii/B9780081008874000044.
100. Iannucci, L. & Willows, M. An energy based damage mechanics approach to modelling impact onto woven composite materials—Part I: Numerical models. *Composites Part A: Applied Science and Manufacturing* **37,** 2041–2056. ISSN: 1359-835X. https://www.sciencedirect.com/science/article/pii/S1359835X05004318 (2006).
101. Matzenmiller, A., Lubliner, J. & Taylor, R. A constitutive model for anisotropic damage in fiber-composites. *Mechanics of Materials* **20,** 125–152. ISSN: 0167-6636. https://www.sciencedirect.com/science/article/pii/0167663694000530 (1995).
102. Camanho, P. & Dávila, C. Mixed-Mode Decohesion Finite Elements for the Simulation of Delamination in Composite Materials (July 2002).
103. Wu, E. M. & Reuter, R. C. *Crack Extension in Fiberglass Reinforced Plastics* in (1965).
104. Benzeggagh, M. & Kenane, M. Measurement of mixed-mode delamination fracture toughness of unidirectional glass/epoxy composites with mixed-mode bending apparatus. *Composites Science and Technology* **56,** 439–449. ISSN: 0266-3538. https://www.sciencedirect.com/science/article/pii/026635389600005X (1996).
105. Zhang, T., Yan, Y., Li, J. & Luo, H. Low-velocity impact of honeycomb sandwich composite plates. *Journal of Reinforced Plastics and Composites* **35** (Oct. 2015).
106. *Abaqus/CAE User's Guide* (Dassault Systemes Simulia, Inc., 2022).
107. Guo, C. & Lu, Z. A 3D FEM Mesoscale Numerical Analysis of Concrete Tensile Strength Behaviour. *Advances in Materials Science and Engineering* **2021,** 1–14 (July 2021).
108. H.N.R., W. *VUMAT_Lecture _1/HashinVumat.for* https://github.com/hnrwagner/VUMAT_Lecture_1/blob/main/HashinVumat.for (2023).

109. Wan, L. *et al.* Computational micromechanics-based prediction of the failure of unidirectional composite lamina subjected to transverse and in-plane shear stress states. *Journal of Composite Materials* **54** (Apr. 2020).
110. O'Higgins, R., Padhi, G., McCarthy, M. & Mccarthy, C. Experimental and Numerical Study of the Open-Hole Tensile Strength of Carbon/Epoxy Composites. *Mechanics of Composite Materials* **40,** 269–278 (July 2004).
111. Chen, J.-F., Morozov, E. V. & Shankar, K. Simulating progressive failure of composite laminates including in-ply and delamination damage effects. *Composites Part A: Applied Science and Manufacturing* **61,** 185–200. ISSN: 1359-835X. https://www.sciencedirect.com/science/article/pii/S1359835X14000530 (2014).
112. Wronkowicz-Katunin, A., Katunin, A. & Dragan, K. Reconstruction of Barely Visible Impact Damage in Composite Structures Based on Non-Destructive Evaluation Results. *Sensors* **19.** ISSN: 1424-8220. https://www.mdpi.com/1424-8220/19/21/4629 (2019).
113. Vallons, K. *The Behaviour of Carbon Fibre - Epoxy NCF Composites under Various Mechanical Loading Conditions* PhD thesis (Jan. 2009).
114. Shi, Y., Swait, T. & Soutis, C. Modelling damage evolution in composite laminates subjected to low velocity impact. *Composite Structures* **94,** 2902–2913. ISSN: 0263-8223. https://www.sciencedirect.com/science/article/pii/S0263822312001547 (2012).
115. Shao, J. R., Liu, N. & Zheng, Z. J. A modified progressive damage model for simulating low-velocity impact of composite laminates. *Advances in Mechanical Engineering* **14,** 16878132221095948. eprint: https://doi.org/10.1177/16878132221095948. https://doi.org/10.1177/16878132221095948 (2022).
116. *Lecture 2: Elements* (ABAQUS, Inc., 2005).
117. Jacquotte, O.-P. & Oden, J. Analysis of hourglass instabilities and control in underintegrated finite element methods. *Computer Methods in Applied Mechanics and Engineering* **44,** 339–363. ISSN: 0045-7825. https://www.sciencedirect.com/science/article/pii/004578258490135X (1984).
118. *Element Selection Criteria* https://mashayekhi.iut.ac.ir/sites/mashayekhi.iut.ac.ir/files/u32/presentation10.pdf.
119. Corporation, L. S. T. *Hourglass (HG) Modes* 2012. https://ftp.lstc.com/anonymous/outgoing/jday/hourglass.pdf.
120. Ferreira, G. F. O., Ribeiro, M. L., Mendes Ferreira, A. J. & Tita, V. Computational analyses of composite plates under low-velocity impact loading. *Materials Today: Proceedings* **8.** 4th Brazilian Conference on Composite Materials (BCCM 4), July 22-25th 2018, 778–788. ISSN: 2214-7853. https://www.sciencedirect.com/science/article/pii/S2214785319300550 (2019).
121. Tita, V., de Carvalho, J. & Vandepitte, D. Failure analysis of low velocity impact on thin composite laminates: Experimental and numerical approaches. *Composite Structures* **83,** 413–428. ISSN: 0263-8223. https://www.sciencedirect.com/science/article/pii/S0263822307001717 (2008).
122. *MATLAB version: 9.13.0 (R2022b)* Natick, Massachusetts, United States, 2022. https://www.mathworks.com.

123. Riccio, A., Raimondo, A., Di Caprio, F., Fusco, M. & Sanità, P. Experimental and numerical investigation on the crashworthiness of a composite fuselage sub-floor support system. *Composites Part B: Engineering* **150,** 93–103. ISSN: 1359-8368. https://www.sciencedirect.com/science/article/pii/S1359836818306668 (2018).
124. Di Caprio, F. *et al.* Design of Composite Stanchions for the Cargo Subfloor Structure of a Civil Aircraft. *Procedia Engineering* **167.** International Symposium on Dynamic Response and Failure of Composite materials, Draf2016, 88–96. ISSN: 1877-7058. https://www.sciencedirect.com/science/article/pii/S1877705816340310 (2016).
125. Mirbagheri, Y., Nahvi, H., Parvizian, J. & Düster, A. Reducing spurious oscillations in discontinuous wave propagation simulation using high-order finite elements. *Computers Mathematics with Applications* **70.** High-Order Finite Element and Isogeometric Methods, 1640–1658. ISSN: 0898-1221. https://www.sciencedirect.com/science/article/pii/S0898122115003089 (2015).
126. Calladine, C. Understanding imperfection-sensitivity in the buckling of thin-walled shells. *Thin-Walled Structures* **23.** Buckling Strength of Imperfection-sensitive Shells, 215–235. ISSN: 0263-8231. https://www.sciencedirect.com/science/article/pii/0263823195000134 (1995).
127. Li, S. & Sitnikova, E. A critical review on the rationality of popular failure criteria for composites. *Composites Communications* **8,** 7–13. ISSN: 2452-2139. https://www.sciencedirect.com/science/article/pii/S2452213917301146 (2018).